UNIVERSITY OF BRISTOL

Measurement of the charged particle multiplicities at a centre of mass energy of 7 TeV at LHCb

by

David Voong

A thesis submitted in partial fulfillment for the degree of Doctor of Philosophy

in the
Faculty of Science
Department of Physics

November 2014

Declaration of Authorship

I, David Voong, declare that this thesis titled, 'Measurement of the charged particle multiplicities at a centre of mass energy of 7 TeV at LHCb' and the work presented in it are my own. I confirm that:

- This work was done wholly or mainly while in candidature for a research degree at this University.
- Where any part of this thesis has previously been submitted for a degree or any other qualification at this University or any other institution, this has been clearly stated.
- Where I have consulted the published work of others, this is always clearly attributed.
- Where I have quoted from the work of others, the source is always given. With the exception of such quotations, this thesis is entirely my own work.
- I have acknowledged all main sources of help.
- Where the thesis is based on work done by myself jointly with others, I have made clear exactly what was done by others and what I have contributed myself.

Signed: ____

Date: ____

UNIVERSITY OF BRISTOL

Abstract

Faculty of Science
Department of Physics

Doctor of Philosophy

by David Voong

This thesis presents a method for unfolding the observed charged particle distributions produced from proton-proton collisions at a centre of mass energy of $\sqrt{s} = 7$ TeV at the LHCb detector. These results will help to constrain the parameters phenomenological particle production models and Monte Carlo event generators, and help to provide insight on the mechanisms behind particle production, especially in the soft QCD regime.

Acknowledgements

Contents

Chapter 1

Introduction

The LHCb collaboration is formed of more than six hundred scientists from over fifty different institutions across the globe, it is truly a testament to human innovation and cooperation. The experiment aims to address some of today's unanswered questions about our Universe, such as the observed matter-antimatter asymmetry (a term which a hundred years ago was a term known only to a few select specialists but today is familiar amongst the general public).

At the heart of the collaboration is the LHCb detector, a finely tuned machine which took over a decade to design and construct. The LHCb detector sets itself apart from the more common hermetic detectors found in operation around the LHC by its unique geometry. This is specialised to detect particles at an angle close to that of beam pipe known as the forward region - a region in which hermetic detectors tend to be insensitive. In addition to this, the production mechanism of exotic mesons such as B and D mesons are favoured in the forward region, making LHCb the current world's best environment in which to the study the decay of such mesons.

The decay processes of these rare particles are thought to hold the key to understanding the mechanisms behind the matter-antimatter asymmetry observed as well as acting as a probe for new physics via loop processes or the famous penguin processes. The unique geometry of the LHCb detector together with its outstanding primary vertex reconstruction and particle identification makes it the ideal machine for scientists at

LHCb to provide many of the world's best measurements, test the standard model and models beyond the standard model more strictly than ever before and to lead searches into new physics beyond our current understanding.

One of the key tools available to particle physicists are those of Monte Carlo simulation. This tool enables scientists to simulate physical processes and gauge how these will manifest themselves in a real life experimental situation. It is a prominent example of the process of bridging between theoretical predictions and their real world observations, a branch of Physics called Phenomenology.

The use of Monte Carlo simulations is prolific in a variety of physics analyses, typically it is used in estimating the background contributions, detector and trigger efficiencies, signal shape and sensitive studies. Such a large span of uses stresses the importance of having a reliable Monte Carlo simulation and much effort has been put into developing models that are in good agreement with measured data. Much of the challenge in this is finely tuning the ample number of parameters used in these simulators through constraints set by measured data.

Chapter 2

Background theory

2.1 The Standard Model

The Standard Model describes fundamental particles and their interactions mediated via force carrying particles. It describes electromagnetism, the weak force and the strong force.

The Standard Model is built upon the principles of Quantum Field Theory and renormalizable gauge theories developed in the twentieth century [1]. It is most commonly represented in the form of the Lagrangian formalism and is divided into the following sectors. The Electroweak sector - describing both electromagnetic forces and weak interactions, Quantum Chromodynamics (QCD) sector - describing the strong interaction and the Higg's sector - describing interactions with the Higg's field.

The Standard Model has proven to be an extremely successful theory having exceptional predictive powers - the theoretical prediction of the electron anomalous magnetic moment being in agreement with experimental data to 10 significant figures [2].

2.1.1 Fundamental Particles

The fundamental particles are categorised by several intrinsic properties which can be seen in table 2.1. By their intrinsic spin they are classified as particles with half-integer spin (fermions) and integer spin (bosons), these are outlined in the following sections.

Fermions

Fermions are further sub-divided into two groups - quarks and leptons - depending on the types of interactions they experience. Quarks have the property of colour which makes them sensitive to the strong interaction whilst leptons do not.

Both quarks and leptons are further sub-divided into three generations; the higher generations correspond to particles with higher mass states, these particles rapidly decay to the lower stable generations by the weak force.

Each fermion generation consists of a particle doublet, for example the first generation of quarks is composed of up and down type quarks. Particles in fermions doublets couple strongly to one another such that interactions between the two particle types are relatively strong in comparison to coupling between particles in different generations. This can be seen in the CKM matrix (a matrix which describing coupling between different quark types measured through experiment) where the coupling between the up and down quarks is approximately four times greater than between up and strange type quarks.

The lepton generations are made up of a charged lepton and neutrino doublet. There is no coupling between lepton generations (in contrast to quarks) in the standard model; higher generation lepton states such as the tau lepton may decay via tree processes such as a decay to its corresponding neutrino along with a $W^{\pm}$ boson (see subsection below).

The three generations together with the corresponding doublets gives a total of 6 quark flavours and 6 lepton flavours.

Bosons

The Standard Model describes two types of bosons, gauge bosons and the Higg's boson.

A gauge boson is a force carrying particle - also referred to as a force mediator - associated to a particular type of interaction e.g. gluons are associated with the strong interaction and photons are associated to the electromagnetic interaction. The term “gauge” comes from the property of the equations of motion related to a given interaction; these are invariant under “gauge” transformations which are discussed in section 2.1.3.

The Higgs boson plays a unique role in the Standard Model. Its existence supports the validity of the Higgs mechanism; a mechanism which explains why some particles are massive while others are not, in addition to why interaction strengths vary for different interaction types. On the 4th July 2012 the discovery of particle with a mass between 125 and 127 GeV was announced; on the 14th March 2013 the properties of the newly discovered particle were found to be consistent with the Higgs Boson predicted by the standard model.

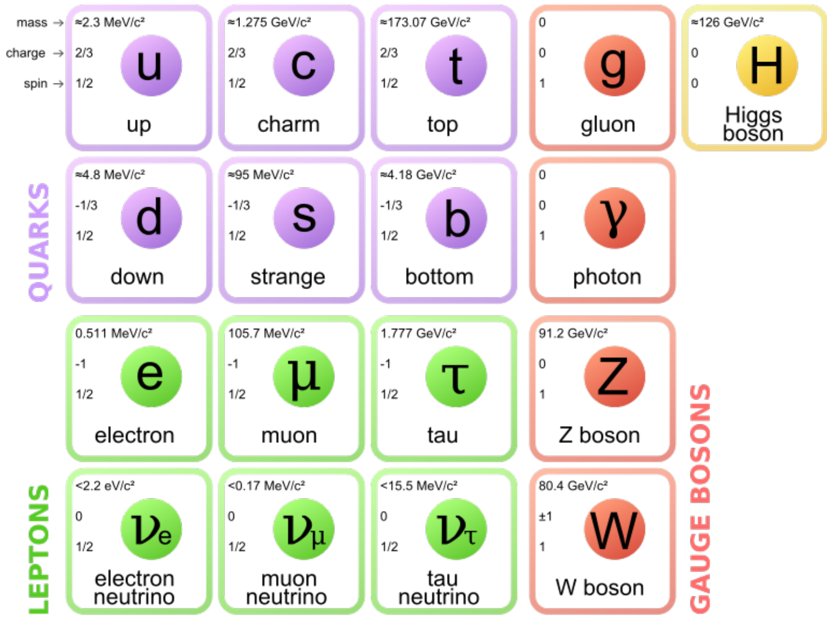

FIGURE 2.1: Table of particles in the Standard Model [3]

2.1.2 Quantum Field Theory (QFT)

Quantum field theory is built on concepts from Quantum Mechanics, Special Relativity and Classical Field Theory. Fundamental particles are described as excitations or quanta of the fields. For example, electrons are quanta of the electron field and similarly photons are quanta of the electromagnetic field i.e. interactions between electrons can be described as being a result of the interaction between the electron field and electromagnetic field. Mathematically these interactions can be described using the Lagrangian Formalism.

2.1.2.1 Lagrangian Formalism

With Lagrangian mechanics the equations of motion for a given field is derived by minimising the action $\mathcal{S}$ given by,

$$\mathcal{S} = \int \mathcal{L}(\phi, \partial_\mu \phi) \mathrm{d}^4 x \tag{2.1}$$

where $\mathcal{L}$ is the Lagrangian density, ϕ is the field and ∂_μ is the differential operator acting on the space and time coordinates of the field as seen in special relativity. By applying the condition of the Principle of Least Action, the equations of motion are given by the Euler-Lagrange equation,

$$\partial_\mu \left(\frac{\partial \mathcal{L}}{\partial(\partial_\mu \phi_i)} \right) = \frac{\partial \mathcal{L}}{\partial \phi_i} \tag{2.2}$$

2.1.3 Gauge Theories

A gauge theory is defined by a Lagrangian which is invariant under continuous local transformations of the fields or coordinates.

$$\delta \mathcal{L} = 0 \tag{2.3}$$

Each possible gauge transformations can be represented by a matrix; together these matrices form a group under matrix multiplication - the symmetry group of the gauge theory.

For each generator of the group there is an associated gauge field, for example, in QED there is one generator to the U(1) group which is associated to the electromagnetic four-vector potential field. Similarly, in QCD there are 8 generators associated to the SU(3) group corresponding to 8 gluon fields. The quanta of the gauge fields are called gauge bosons, for the previous examples these are the photon and gluons respectively.

The symmetry group for the Standard Model is U1 x SU(2) x SU(3), it is a non-Abelian group with 12 gauge fields; the corresponding gauge bosons are the photon, W+, W-, Z0 and eight types of gluon.

2.1.4 Coupling Constants

The coupling constants of a theory are dimensionless values that describe the strength of an interaction. For example the fine structure constant of QED (α) describes the strength of the electromagnetic interaction, defined as,

$$\alpha = \frac{e^2}{4\pi} \tag{2.4}$$

where e is the charge of the positron[1] and α has the value 1/137. Theories with coupling constants that have a value much less than one are said to be weakly coupled. The evolution of systems described by these theories are compatible with perturbative calculations in which the expansion is based on powers of the coupling constant. Conversely theories with coupling constants that have a value of the order of one or greater are said to be strongly coupled and are not compatible with the perturbation method.

The Standard model consists of theories with running coupling constants, which vary depending on the energy scale of a process. The behaviour of these are described by the β functions,

$$\beta(g) = \frac{\partial g}{\partial log(\mu)} \tag{2.5}$$

[1] Expressed in Heaviside-Lorentz and natural units. Unless explicitly stated otherwise all following equations will be expressed in this way

where g is the coupling constant of the theory ($g = e$ for QED) and μ is the interaction energy scale. A β function with positive values describes a coupling that increases with the energy of the process and vice-versa.

2.1.5 Quantum Electrodynamics (QED)

QED is an example of a Quantum Field Theory, it describes the electromagnetic interactions between charged fermions via the exchange of photons - gauge bosons of the theory. It is both a Quantum Field Theory as well as a Gauge Theory with a symmetry group of U(1) - an Abelian group of composed of 1 x 1 unitary matrices. The Electroweak theory of the standard model is a unification of QED and Quantum Flavour Dynamics - a gauge theory which describes the weak interaction. The Lagrangian for the QED is given by,

$$\mathcal{L} = \bar{\psi}(i\gamma^\mu D_\mu - m)\psi - \frac{1}{4}F_{\mu\nu}F^{\mu\nu} \tag{2.6}$$

where ψ is a bispinor field of spin 1/2 corresponding to the electron field; γ^μ are the Dirac Matrices; $\bar{\psi}$ is the Dirac adjoint spinor $\psi^\dagger\gamma^0$; D_μ is the gauge covariant derivative given by,

$$D_\mu = \partial_\mu + ieA_\mu + ieB_\mu \tag{2.7}$$

e is the coupling constant between the electron and electromagnetic fields - charge of an electron; A_μ is the covariant four-potential of the electromagnetic field generated by the electron; B_μ is the external field due to an external source and $F_{\mu\nu}$ is the electromagnetic field tensor given by,

$$F_{\mu\nu} = \partial_\mu A_\nu - \partial_\nu A_\mu \tag{2.8}$$

2.1.6 Quantum Chromodynamics (QCD)

QCD is a physical theory that describes the interactions between particles with the property of colour via strong interactions. It is a gauge theory with a symmetry group of SU(3) (the group of unitary matrices with a determinant of one) and describes the interactions between quark and gluon fields.

The strong force is responsible for the binding force which holds nucleons together to form the nucleus of an atom. This is due to the deeper fundamental interaction between the components of nucleons - quarks and gluons - collectively called partons. The gluons are the gauge bosons of the theory i.e. mediators of the strong force. It is a short range force having a significant effect only on scale of ~ 1 fm (about the size of the charge radius of a proton) due to the nature of its coupling. The Lagrangian of QCD is,

$$\mathcal{L} = \bar{\psi}_i i((\gamma^\mu D_\mu)_{ij} - m\delta_{ij})\psi_j - \frac{1}{4}G^a_{\mu\nu}G^{\mu\nu}_a \tag{2.9}$$

where $\bar{\psi}_i$ is the quark field and $G^a_{\mu\nu}$ is the gluon field strength tensor given by,

$$G^a_{\mu\nu} = \partial_\mu A^a_\nu - \partial_\nu A^a_\mu + g f^{abc} A^b_\mu A^c_\nu \tag{2.10}$$

where A^a_ν are the gluon fields and f^{abc} are the fine structure constants of the SU(3) group.

Quarks have been observed in two-quark bound states (mesons) and three-quark bound states (baryons); the six flavours of quarks give rise to many possible quark combinations, these combinations are commonly grouped into octets by the eightfold way, figure 2.2.

The property of colour in QCD is analogous in many ways to the role of electric charge in QED. However instead of there being one type of charge in QCD there are three types, labelled red, green, blue and their corresponding anti-colours anti-red, anti-green and anti-blue. The names of the charge types are motivated by the behaviour of coloured light such that a bound state of a red, blue and green quarks gives a net colour charge of white or colourless; a combination of colour and anti-colour is also colourless.

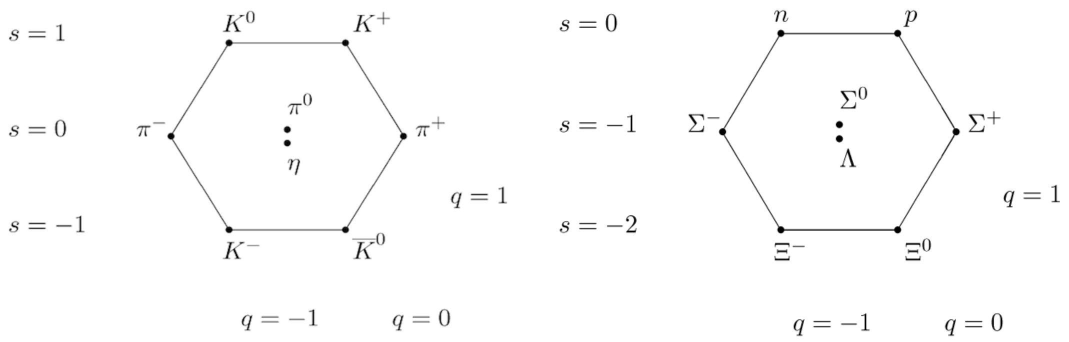

(A) The meson octet (two quark bound states) (B) Baryon octet (three quark bound states)

FIGURE 2.2: Eightfold method of organising quark bound states. Bound states on the same horizontal share the same strangeness and those on the same diagonals running top left to bottom right share the same charge

Each quark possesses one of the three types of colour charge; it can be either red, green or blue (similarly so for anti-quarks and the anti-colour charges). Gluons on the other hand possess a combination of colour and anti-colour charge (though these charges are not necessarily of the same colour). Since gluons are charged, QCD features some additional richness not seen in its QED counterpart. Gluons can couple with one other unlike photons which cannot, see figure 2.3.

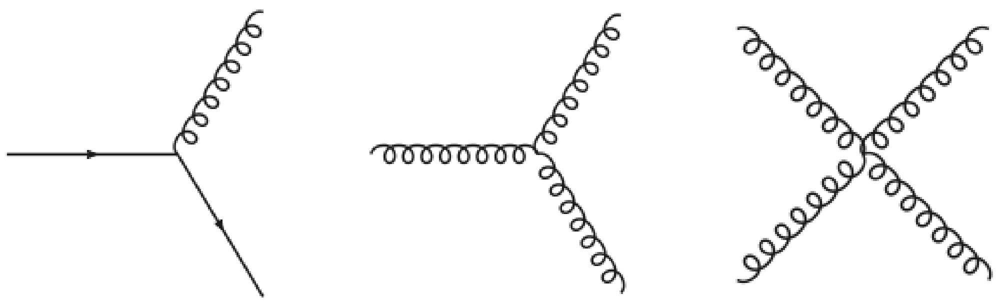

(A) Quark-gluon vertex (B) Three-gluon vertex (C) Four-gluon vertex

FIGURE 2.3: QCD field couplings

Asymptotic freedom

The coupling constant α_s of QCD describes the strength of the strong interaction. The β function for the strong coupling constant is given by,

$$\beta(\alpha_s) = -\left(11 - \frac{2n_f}{3}\right)\frac{\alpha_s^2}{2\pi} \tag{2.11}$$

where,

$$\alpha_s = \frac{g^2}{4\pi} \tag{2.12}$$

and n_f is the number of quark flavours in the theory. Since there are six quark flavours in the standard model the values of the β function are negative i.e. the coupling constant of the strong force decreases with an increase in the energy transfer (or equivalently a decrease in the distance) of the process. The running coupling constant as a function of the energy transfer is given by,

$$\alpha_s(|q^2|) = \frac{4\pi}{(11 - \frac{2n_f}{3})\ln(|q^2|/\Lambda^2)} \quad (|q^2| >> \Lambda^2) \tag{2.13}$$

where $|q^2|$ is the energy transfer of the process and Λ is the QCD scale defined as the energy transfer at which the strong coupling constant $\alpha_s \sim 1$ and perturbative calculations with expansions of the coupling constant diverge.

This behaviour of the strong force coupling constant to become weaker at short range interactions is known as asymptotic freedom. Quarks and gluons which interact over short distances - such as at high energy collider experiments - interact very weakly and act as quasi-free particles. Since the coupling constant is small in this regime perturbative methods can also be used calculate properties of the theory.

Colour Confinement

Colour confinement is an observed phenomenon in which partons are only observed in bound colour singlets states, i.e. no individual free quarks or gluons have been observed. As quarks are separated the coupling constant increases such that the energy needed to separate them increases indefinitely. At some energy threshold the system of separating quarks will have enough enough energy to spontaneously form quark anti-quark pairs - forming a bound state with the initial quarks. This process - called hadronisation - may occur multiple times resulting in a shower of particles called a jet. Since the strong coupling constant is inherently large in these processes perturbative methods are incompatible with describing this behaviour, instead our best understanding is achieved by phenomenological models (see section 2.3.3).

2.2 QCD in Proton Collider Experiments

The complexity of QCD shown in colour confinement and the running of the strong coupling constant present additional challenges in experimental physics. In order to describe the behaviour of QCD phenomena with perturbative methods the strong coupling constant must be small such that a perturbative expansion in powers of the coupling constant converge. This is true in the case short range interactions where asymptotic freedom is present though this is not the case for long range interactions at the scale of Λ_{QCD}.

Colour confinement tells us that coloured particles can only be observed in colour singlet states called hadrons. The size of hadrons ($\sim$ 1 fm) corresponds to a energy scale of approximately 200 MeV ($\approx \Lambda_{QCD}$), hence, the observable particles associated to QCD are coupled to long range physics - i.e. incompatible with a purely perturbative description. To describe such states a combination of perturbative and non-perturbative approaches must be used.

2.2.1 Factorisation

Factorisation is the process of decoupling the hard and soft scale physics in QCD phenomena into products of hard and soft scale terms. By factorising the problem, the well understood perturbative methods can be used to calculate terms involving hard scale interactions - where $\alpha_s << 1$ - and non-perturbative methods are used to calculate the remaining contributions from soft scale physics.

The hard process is described by a matrix element calculated using the perturbative Feynman approach from the QCD Lagrangian. The soft physics is characterised by a parton distribution function which describes the density and momentum of quarks within the proton. Cross sections are then calculated by convoluting the parton level cross section with the parton distribution function.

For the process, $ij \to k$ in a proton-proton interaction, the cross-section $\sigma_{ij\to k}$ is described by,

$$\sigma_{ij\to k} = \int \mathrm{d}x_1 \int \mathrm{d}x_2 f_i^1(x_1) f_j^2(x_2) \hat{\sigma}_{ij\to k} \tag{2.14}$$

where $\hat{\sigma}$ is the cross-section for hard partonic cross-sections and f_i^1 is the parton distribution function describing the probability of finding a parton of type i in the beam proton 1 with momentum fraction x_1; similarly f_i^2 describes the distribution of partons for beam proton 2.

Due to the non-perturbative nature of parton distributions, their determination is through fits to experimental data such as from deep inelastic scattering experiments. The parton distribution functions are universal in that the parton distribution function calculated from one experiment may be used as input for another. For experiments involving different energies the behaviour of the parton distribution functions at different energy scales is described by the DGLAP evolution equations [4].

Protons accelerated to high energies are highly boosted in the laboratory rest frame, the proton is Lorentz contracted in the direction of the beamline and time dilated so that its constituent partons appear frozen, each carrying a longitudinal momentum fraction x of the total proton longitudinal momentum. The boost also ensures partons are well modelled as being collinear to its parent proton, i.e. $0 < x < 1$. The beam crossing time is short enough such that an interactions between partons in opposing beams can be modelled as a one-to-one interaction; i.e. interactions in the final state do not interfere with the initial parton-parton interaction. In this environment the proton-proton beams are well modelled as sources of quasi-free quarks and the interactions in the system are well described by a factorisation scheme.

2.3 Monte Carlo Generators

Monte Carlo (MC) generators are computational software used to simulate high energy processes. They use the principles of random sampling to emulate quantum mechanical phenomena together with the Standard Model and phenomenological models to describe particle interactions.

MC generators are important for many aspects of high energy physics. They enable physicists to develop an understanding of how physics models translate to real world experiments bridging between the theoretical and experimental aspects of high energy physics. MC generators provide physicists insight into the frequency of specific types of events as well as the angular distribution of the resultant particles. This enables physicists to estimate the signal to background ratios of specific processes and provide insight into which regions of phase space provide the greatest level of sensitivity for a given process. Understanding the distribution of the resultant particles from a given type of interaction enables highly specialist detector design optimised for sensitivity to a given process.

MC generators are extremely sophisticated programs due to the complexity of high energy process. This process is simplified by factorising the process into several steps. First a hard process is simulated with associated initial state radiation followed by the hadronisation process and final state radiation as well as beam remnants. These components are discussed in the following sections and are visualised in figure 2.4.

2.3.1 The Hard Process

The hard process is described by the parton interaction with the highest momentum transfer, it characterises the properties of the event such as the distribution of particles in the system and their energies. In general, experimentalists are interested in events involving a particular hard process, such as the production of exotic flavoured states, e.g.

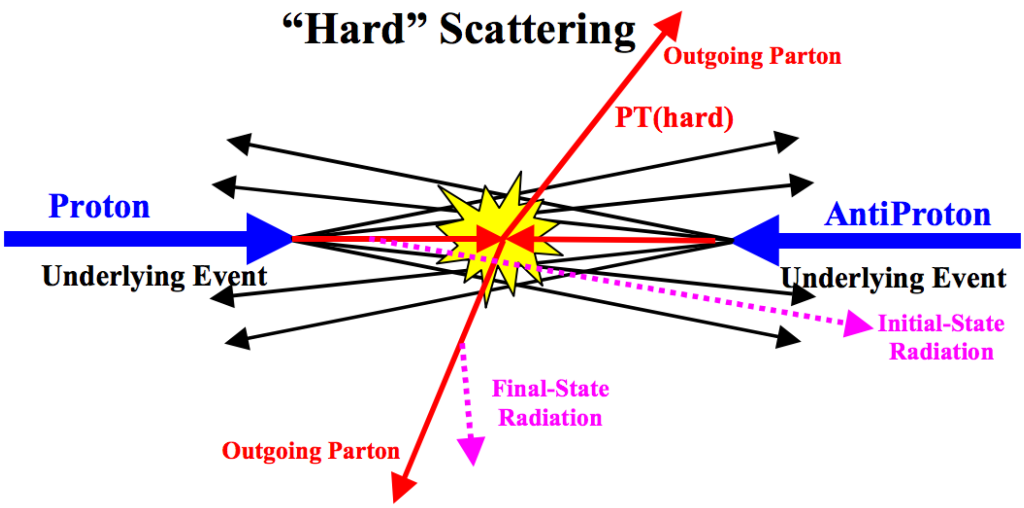

FIGURE 2.4: An event schematic demonstrating the aspects of the interaction [5]

$$gg \rightarrow c\bar{c} \tag{2.15}$$

describing the process of gluon fusion forming a charm quark-antiquark pair.

The hard process is the first stage of a MC event simulation, next a backwards time evolution is performed on the initiator partons to describe the system before the interaction. In the proton-proton event case this corresponds to the state of the incoming proton pairs. Similarly a forward time evolution is applied to the outgoing partons of the interaction to describe the final state of the system.

The forward evolution is divided into two phases, the first stage describes the radiation of quarks and gluons from the outgoing partons as a series of parton branchings evolving the system from a state with a low number of high momentum partons to a state with a high number of low momentum partons (parton shower 2.3.2). This process describes the branchings using perturbative calculations down to a momentum threshold where perturbative methods are no longer applicable. Similarly an upper momentum threshold exists; partons with a momentum greater than this threshold are assigned to the hard process of the event.

The second phase takes the output of the parton shower and evolves it into a system of colourless hadrons using non-perturbative phenomenological models via the process of hadronisation (section 2.3.3).

2.3.2 Initial and Final State Radiation

Initial state radiation is composed of partons that are emitted from the beam particles. In the case of proton beams this is modelled as virtual particles being exchanged between the quark constituents; these virtual particles primarily consist of gluons which may further radiate pairs of gluons creating a complicated state of the proton. Similarly final state radiation consists of a myriad of partons but in this case the partons originate from the out-going partons of the hard scatter and initial state radiation.

The probability for branching to occur is generally calculated in one of two ways, either with a matrix element calculated from Feynman diagrams or with the parton shower model. The parton shower model is a simplified version of the matrix element approach with approximations including a simplification of kinematics, interference and helicity structure. Though the matrix element calculations are truer to the theory of QCD, in practice the matrix elements are more difficult to calculate - especially at higher orders. The two approaches are complementary to one another and which approach is used is based on the particular situation. In general the parton shower is chosen as the first place to start due to its flexibility and simplicity whilst for precision measurements the matrix element approach is favoured.

Parton Showers

The parton shower is made up of branchings of the form $a \to bc$, e.g for quark-gluon radiation this is,

$$q \to qg$$

Each of the partons in a shower are characterised by its virtuality scale Q^2 which gives an approximate sense of its time ordering in the shower, classically it is defined as the invariant mass of the parton; under this definition a system with a low number of high mass partons evolving into a high number of low mass partons will decrease in the virtuality scale as more and more branchings occur. The Q^2 variable may also be described by other variables such as its transverse momentum which similarly decreases with the number of branchings. A maximum virtuality scale Q_{max} distinguishes partons that are involved in the hard process from those in the parton shower, also a minimum virtuality scale Q_0 sets the scale at which non-perturbative effects become significant.

Partons with $m^2 < 0$ and $m^2 \geq 0$ are described as space- and time-like respectively.

Initial State Radiation (ISR)

For initial state radiation the virtuality scale is typically associated to the mass of the parton given by the equation,

$$Q^2 = -m^2 = -(E^2 - p^2) \tag{2.16}$$

The branching evolution of initial state radiation is described by increasing values of the virtuality scale Q^2, this corresponds to a high energy parton from a beam particle emitting partons with increasing virtuality and momentum i.e. the branching partons become more space-like. The branching continues until there are enough partons with $Q^2 \geq Q^2_{\text{max}}$ to initiate the hard process; thus limiting the virtuality of the system, for example, the virtuality of the partons in the process $q\bar{q} \rightarrow Z^0$ have a virtuality cut off of the order of the $2m_{Z^0}$.

In order to generate an event with a particular hard process the shower algorithm first sets the longitudinal momentums x_1 and x_2 of the incoming partons to that required by the hard process using the parton distribution function. A backward time evolution is then applied to the partons, gaining energy with each emission and decreasing in virtuality until it is compatible with a shower initiating parton in the proton.

Final State Radiation (FSR)

For final state radiation the initiating shower parton originates from the outgoing partons of the hard interaction via time-like partons. The virtuality scale for partons is typically defined by either its invariant mass or transverse momentum.

$$Q^2 = m^2 \tag{2.17}$$

or

$$Q^2 = p_\perp^2 \tag{2.18}$$

note the change in sign in the mass ordering relative to the ISR. The final state evolves with a decreasing virtuality scale - becoming more time-like. Starting from an outgoing parton from the hard process the branching results in partons with lower mass or transverse momentum depending on the choice of ordering parameter. The minimum virtuality of a parton is set by Q_0, partons which cannot branch further due to this cutoff are then used as input for the hadronisation process.

2.3.3 Hadronisation

Hadronisation is the process of evolving a system of coloured partons into colourless hadrons, photons and leptons. Hadronisation occurs in the long distance regime where perturbation theory breaks down. Instead MC generators use phenomenological models to describe the process. The two leading class of models are the string model and the cluster model, described further in the following sections.

The hadronization model used varies in importance for different observable parameters i.e. some variables are more sensitive to it than others. It has a significant effect on the particle multiplicity of an event but less so for the energy flow which is instead more sensitive to the hard process of the event. Therefore in order to constrain hadronisation models with real data, observables such as the particle multiplicity are of great importance.

The String Model

The Pythia generator uses the a string model to model the hadronization process, in this model quark bound systems are described as being connected by a string with potential,

$$V(r) = \kappa r$$

where r is the distance between the quarks and κ is the tension of the string ($\sim$ 1 GeV/fm). In this model, a system with a separating quark-antiquark has a colour flux tube joining the pair. The diameter of the tube has dimension of the typical hadronic size ($\sim$ 1fm) and is assumed to be cylindrically symmetric along its length. A massless relativistic string with no transverse degrees of freedom is used to model the axis of symmetry and the tension in the string (κ) gives the energy density of the colour flux tube.

As the distance between quarks increases the flux tube grows longer but with fixed diameter giving rise to the linear potential. This implies a distance independent force of attraction above some distance scale, it is thought that this is due to gluon self interactions originating from the three gluon vertex processes though it is not well understood.

The Cluster Model

The cluster model is based on the concept of colour pre-confinement, a property of QCD that states for partons at virtuality scales (Q) much lower than the hard process (Q_{H}),

$$Q << Q_{\mathrm{H}}$$

form colour-singlets pairs called clusters. The invariant mass distribution of the clusters falls rapidly at high masses and is asymptotically independent of the scale of the hard process (Q_{H}), depending only on Q and the QCD scale Λ_{QCD}.

To form clusters from the parton shower, the cluster model first performs gluon splitting that evolve gluons into a quark-antiquark pairs that then form the singlet cluster states with neighbouring quarks. These then undergo isotropic quasi-two-body decays into the observed hadrons.

2.3.4 The Underlying Event

The underlying event is any other activity in an event that accompanies a hard process, it contains contributions from the beam remnants - the left over proton fragments after the hard scatter - multiple parton interactions and initial and final state radiation. The hard scatter consists of the two outgoing jets, the initial state radiation leading to the hard process and the particles originating from the hard final state radiation.

The beam remnants are particles that evolves from the remainder constituents of the beam particle that do not take part in the hard process. These may be colour connected to the hard process due to colour confinement e.g. for a proton-proton interaction, a proton that initiates a hard process via a quark initiator will have remaining constituents that form a colour triplet. The colour connections are later resolved during the hadronisation process which ensures the final state of the interaction is composed of colour singlet hadrons.

2.3.5 Multiple Parton Interactions (MPI)

Multiple Parton Interactions (MPI) describe processes that involve two or more distinct hard parton interactions for a single hadron-hadron interaction. Since partons appear localised and static in the the lab frame in the case of hadrons colliding at relativistic energies, these multiple interactions can be modelled as independent interactions and hence by a Poisson distribution. In addition to this, the number of MPI is also dependent on the amount of overlap (which is related to the impact parameter) between the interacting hadrons with a higher average number of interactions occurring with a larger overlap. This has the overall effect of widening the Poisson distribution with the degree of this effect depending on the distribution of partons within the hadron.

The initial inclusion of MPI models originated due to the regularisation of a divergence in the parton-parton scattering cross-section in the low p_{T} region [13]. In this picture the ratio of partonic cross-section to the total cross-section can be interpreted as the average number of parton interactions per hadron-hadron interaction.

Their inclusion has been shown to more accurately describe observed data in high p_{T} events made at the Intersecting Storage Rings (ISR) at CERN [6] and the CDF and D0 experiments at Fermilab, Chicago [7] [8] [9]. And for low p_{T} underlying event observables in $p\bar{p}$ events at the CDF detector [10] [11] and pp events observed at the CMS detector [12]. The use of MPI models in MC generators (e.g. Pythia [13] [14] [15] and others [16] [17]) have also been shown to have led to successful descriptions of observed soft hadronic events.[13]

2.3.6 PYTHIA

PYTHIA is a multi-purpose event generator commonly used in the field of high energy physics with a focus on simulating collisions between elementary particles e.g. e+e- pp interactions and multi-hadronic final states. It contains theory and models for a number of physics aspects, including hard and soft interactions, parton distributions, initial- and final-state parton showers, multiple interactions, fragmentation and decay. And it uses the Lund string model for the hadronisation of partons; a feature which can be traced back to PYTHIAs connection to the JETSET event generator developed by the Lund group at Lund University, Sweden with which it merged in 1996.

Since the merger there have been many other additional developments on the PYTHIA programs. An interleaved evolution was introduced in PYTHIA 6.3 with p_{T} ordered parton showers and more sophisticated minimum bias and models of the underlying event. And also the addition of supersymmetric models with R-parity violation, Technicolor models, Z0/W0 models, models with extra dimensions, etc.

In 2004 the PYTHIA developers decided that for future versions of the software the programming language in which PYTHIA was written would be changed from Fortran

77 to C++. This prompted a process of migrating the structure and logic from one language to another and was completed in 2007 with the release of PYTHIA 8.1 [18].

PYTHIA LHCb

The LHCb experiment uses its software package Gauss [19] as its primary Monte Carlo event generation tool. It encompasses both event generation and detector simulation aspects and is specialised for LHCb physics. It uses PYTHIA 6.4 as well as other optional Monte Carlo event generators components together with EvtGen [20] - which manages the decay and evolution of particles produced by the Monte Carlo event generator - and Geant [21] for its detector simulation.

Additional tools are also present that focus on aspects such as on the collision properties: pile up - the presence of multiple proton-proton interactions in a single beam crossing, beam luminosity and crossing dynamics, and the smearing of the interaction point about the nominal interaction position.

The values of the parameters used in PYTHIA (or tune) for the LHCb event generation is determined from data collected such as from charged particle density measurements at the UA5 and CDF experiments. The non default parameter values and the versions of PYTHIA used in the LHCb event generation are shown in section A.1.

EPOS

EPOS is an MC generator using an approach of Energy conserving quantum mechanical scattering based on Parton ladders, Off-shell remnants and the Splitting of parton ladders [22]. Originally designed for the purpose of modelling minimum bias hadronic events with high parton densities such as from proton-nucleus, nucleus-nucleus, heavy ion and cosmic ray air shower interactions. It was later adapted to model minimum bias proton-proton hadronic events at the LHC [23] called EPOS LHC.

In the EPOS generator an interaction between particles is modelled using a parton ladder which describes the evolution of the parton interactions originating from the beam particles occurring in parallel. The parton ladder can be considered as a quasi-longitudinal colour field or flux tube and can be treated as a relativistic string which decays via the production of quark-antiquark pairs [24].

The density of these relativistic strings determines how the hadronisation is handled; regions of high string fragment density are classified as the core region, lower density regions are assigned to the corona region. In the corona region the hadronisation process is similar to the hadronisation in the PYTHIA generator, however the hadronisation procedure in the core region is carried out using the EPOS collective hadronisation procedure [22].

2.4 Minimum bias data

To minimise the bias of data from inelastic collisions collected from collider experiments, experimentalists use a trigger with a minimal set of criteria - generally called the minimum bias trigger. This trigger will typical involve requirements such as a minimum number of hits in an event or an event with at least one reconstructed track. Biases are still present due to collisions that are not detectable such as collisions that result in particles with trajectories collinear to the initial trajectory of the beam particles; these particles continue along the beam pipe leaving no sign in the sensitive components of the detector.

Collisions at the LHC can be classified into elastic (in which no additional particles are produced and inelastic) and inelastic collisions,

$$\sigma_{tot} = \sigma_{elastic} + \sigma_{inelastic} \tag{2.19}$$

which can be further classified into diffractive and non-diffractive collisions,

$$\sigma_{inelastic} = \sigma_{non-diffractive} + \sigma_{single-diffraction} + \sigma_{double-diffraction} \tag{2.20}$$

Diffractive collisions involve collisions that do not transfer colour between the beam particles and are characterised by events with large rapidity gaps with no hadronic activity. They can involve the break up of one of the incoming protons (single diffraction) or both (double diffraction, see figure 2.5). The events typically selected by a minimum bias trigger are made up of non-diffractive inelastic events with a small contributions from diffractive collisions. From the analysis of MC data generated by the LHCb group, the requirement that the reconstruction of at least one track in the nominal acceptance of the detector increases the percentage of non-diffractive inelastic collisions occurring in the detector increases from 53.4% to 81.5% with the other collisions consisting of a 25% contribution from diffractive collisions in the former and 18.5% in the latter, more detail on this can be found in section 5.

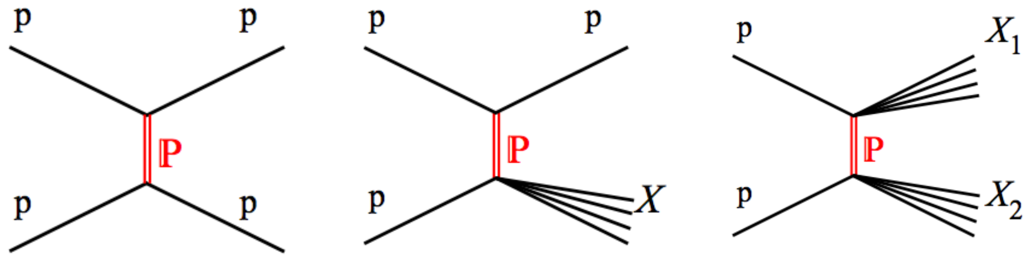

(A) Elastic scattering, $p+p \rightarrow p+p$

(B) Single diffractive scattering, $p+p \rightarrow p+X$

(C) Double diffractive scattering, $p+p \rightarrow X+X'$

FIGURE 2.5: Examples of elastic and inelastic proton-proton interactions via the exchange of a pomeron [25].

Minimum bias data is dominated by soft QCD physics characterised by low p_T particles and long interaction distances. This property of minimum bias data makes it the ideal region in which to validate, tune and develop phenomenological models e.g. particle production and the structure of the proton. Furthermore minimum bias data is a good approximation of the underlying event (see section 2.3.4) which accompanies a hard scale scatter; a good understanding of this translates to a good understanding of the associated hard energy scale physics such as the rare B decays integral to understanding matter and anti-matter physics.

Chapter 3

The LHCb detector

3.1 The Large Hadron Collider (LHC)

The Large Hadron Collider (LHC) is located at the European Organisation for Nuclear Research (CERN) near Geneva in Switzerland. On the 23rd November 2009 the collider began producing collisions at a centre of mass energy of 900 GeV. Over the course of its operation the energy of the collisions has increased, for proton-proton collisions the centre of mass energy was increased first to 7 TeV (28 February 2010) and then 8 TeV (5 April 2012) with a peak luminosity of the order $10^{34}\,\mathrm{cm}^{-2}\,\mathrm{s}^{-1}$, making the LHC world's highest energy and luminosity particle accelerator.

In the future the LHC intends to continue to push the energy and luminosity boundaries to reach unprecedented levels of high energy interactions and data collection. The goal being to produce collisions with a centre of mass energy of 14 TeV or greater. In addition to this, the sub-detector components will be upgraded to improve in areas such as detector readout rate and the resolution of kinematic quantities. Together with the increase in beam energy and luminosity this will give scientists at the LHC the ability to challenge the Standard Model at a level of greater detail than ever seen before.

Stationed at locations around the LHC are several detectors. The two counter-directional beams of proton bunches are focused at these positions such that a large number of collisions occur at the position of the detectors. The six main detectors, ALICE[26], ATLAS[27], CMS[28], LHCb[29], TOTEM[30] and LHCf[31] function as complementary experiments. A full discussion with regards to each detector at the LHC is beyond the scope of this thesis, therefore this thesis focuses on the most significant detector related to the research discussed, the LHCb detector.

3.2 LHCb Overview

The main aim of the LHCb experiment is to study CP violation processes and other rare phenomena particularly those involving the decay of B and D mesons. Designed to build upon the research carried out by the B factories Belle and BarBar, LHCb aims to produce significant improvements on the available statistics of B^+, B^0 and B_s decays. This enables LHCb to further constrain and confirm results from the B factories as well as investigate the possibilities of new physics.

The requirements for the detector include high precision vertex resolution is required to identify secondary vertices and tag B events; accurate particle identification is required to detect and classify rare processes; and a fast and efficient trigger with the ability to filter the copious events produced from the LHC's high luminosity.

The LHCb detector is a single arm spectrometer with a forward angular coverage from approximately 10 mrad to 300 [250] mrad in the bending [non-bending] plane. It comprises of a vertex detection system, a tracking system, Ring Imaging Cherenkov Detectors (RICH), a calorimeter system, muon detector, trigger system and computing farm. Each have been specifically designed to achieve the criteria stated previously and individually discussed in the following sections.

3.3 Vertex Locator (VELO)

The detection of rare B and D meson decays is a key requirement to meet the physics goals of the LHCb experiment. In the LHCb detector these processes are characterised by the presence of production and decay vertices. To maximise the sensitivity of detecting and correctly identifying these events via the presence of displaced vertices a dedicated

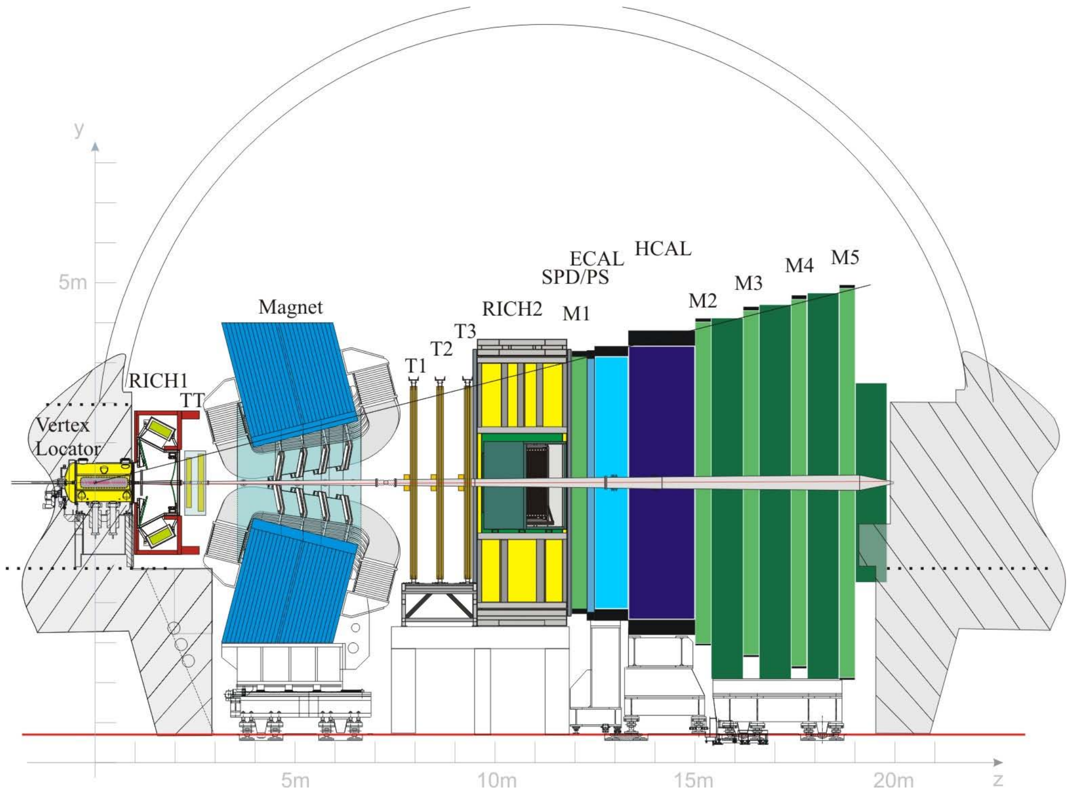

FIGURE 3.1: LHCb schematic

sub-detector system called the VELO (Vertex locator) is employed around the nominal interaction region. The detection of vertices is achieved indirectly via the detection of their decay products through track reconstruction, the paths of which are extrapolated towards a common point of intersection to give the vertex. The reconstruction of VELO tracks is also important for use in the LHCb trigger system, discussed in section 3.9.

The VELO is a silicon micro strip vertex detector, it is made up of two halves (left and right) each containing twenty one track station modules (figure 3.2) positioned at different points along the beam axis. The angular coverage of the VELO detector is shown in figure 3.3.

Modules are approximately semi-circular in shape, 300 μm thick, with an outer diameter of 84 mm and an inner diameter of 8mm in order to accommodate the beam pipe. Each module is composed of a pair of sensors which measure the radial distance and azimuthal angle of particles traversing the detector. The silicon strips of the radial sensor are orientated radially about the module and in concentric semi-circles for the azimuthal sensor, see figure 3.4. The modules are also contained within a secondary vacuum to

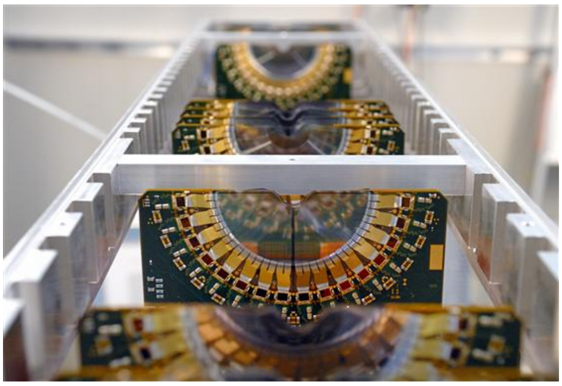

FIGURE 3.2: VELO silicon stations during partial construction of the VELO sub-detector

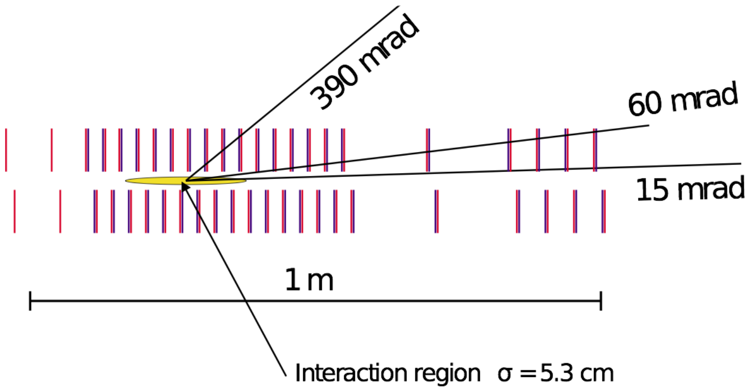

FIGURE 3.3: The layout of the VELO R (red) and ϕ (blue) sensors shown in the (x,z) plane. A $\pm 2\sigma$ area around the nominal interaction point is shown in yellow. Lines drawn at 390 mrad and 15 mrad represent the maximum and minimum angular coverage, while the line at 60 mrad shows the average track angle in minimum bias events. The left-most two pairs of R sensors are the pileup veto stations.

reduce background contributions from interactions with gas particles in the beam pipe, this is enclosed by a 300μm thick aluminium foil which also protects from radio frequency pickup from the beam.

The two halves of the detector open and close about the interaction region depending on the status of the LHC beam (see fig 3.5). During the beam fill or dumping the VELO is put into its open configuration in order to minimise radiation damage to its components. When the beam is stable the VELO is configured into its closed configuration (In this configuration the minimal distance between the silicon trackers and the beamline is 8mm) to maximise its tracking resolution.

Figure 3.6 shows the resolution of the primary vertex position as a function of track multiplicity and figure 3.7 shows the resolution of the impact parameter as a function

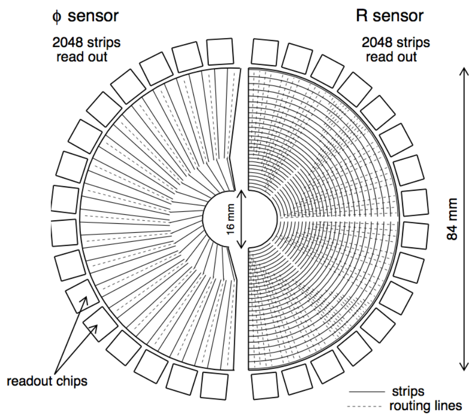

FIGURE 3.4: Schematic diagram of a VELO station from the perspective of along the beam line. Each half consists of both R and ϕ sensors though in this figure only the ϕ sensors are shown in the left half and only the R sensors are shown in the right half.

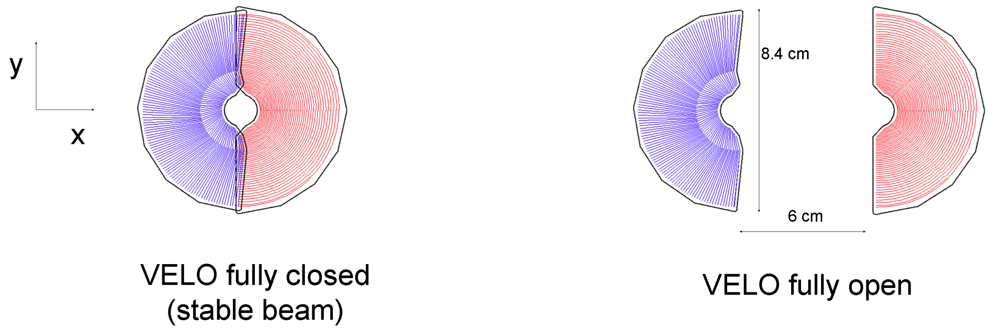

FIGURE 3.5: The front face of the first modules illustrated in two configurations. Closed (left): Once the beam position is stable the halves close so that the position between the VELO and the interaction region is minimised. Open: The two halves are separated in order to protect the modules from the unstable beam.

of p_{T}^{-1}. Both of these measurements approach the expected design parameters [32].

3.4 Ring Imaging Cherenkov Detectors (RICH)

Cherenkov Radiation

Charged particles traversing through a medium at a speed greater than the speed of light in the same medium emit electromagnetic radiation known as Cherenkov radiation. The angle at which the radiation is emitted relative to the direction of the particle (Cherenkov angle, θ_C) is constant given the speed of the particle and the refractive index of the medium are also constant. The relationship between the speed of the

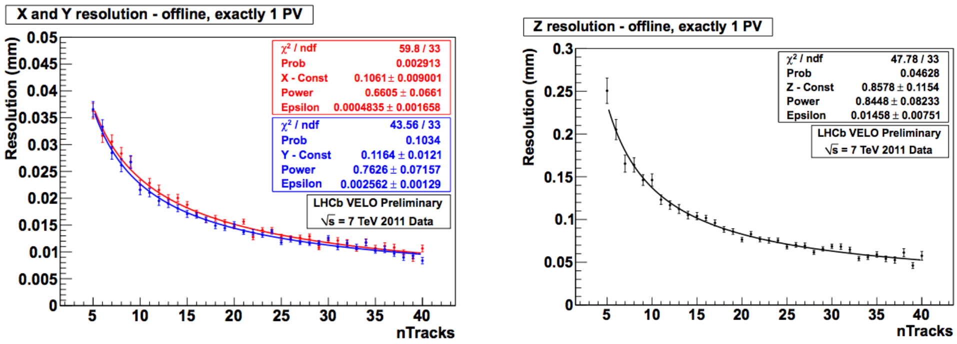

(A) x in red, y in blue

(B) z

FIGURE 3.6: Resolution of primary vertex position [32]

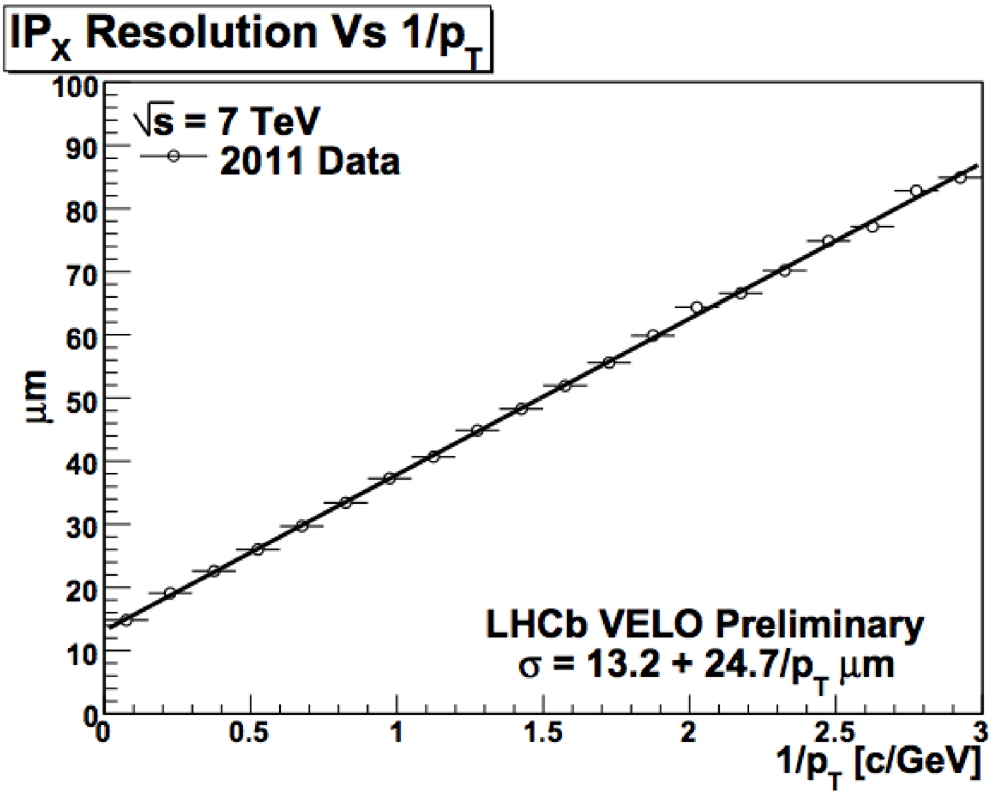

FIGURE 3.7: Impact parameter resolution as a function of p_T^{-1}

particle ($\beta = |\vec{v}|/c$), refractive index of the medium (n) and the Cherenkov angle (θ_C) is described by the equation,

$$\cos\theta_C = \frac{1}{n\beta} \tag{3.1}$$

The speed of the particle, β can be expressed in terms of its mass m and momentum $\vec{p}$, the equation for the Cherenkov angle in these terms is then,

$$\cos\theta_C = \frac{1}{n}\sqrt{1+\frac{m^2}{p^2}} \tag{3.2}$$

where $\beta = \frac{|\vec{p}|}{E} = \frac{|\vec{p}|}{\sqrt{p^2+m^2}} = \frac{1}{\sqrt{1+m^2/p^2}}$. For a charged particle emitting Cherenkov radiation, measurements of the Cherenkov angle of its emitted photons together with its momentum information (e.g. using information from tracking systems) and the above relationship allows the calculation of its mass and hence particle type (particle and anti-particles can be distinguished by their charge, e.g from the direction of bend when passing through a magnetic field). Measurements of the Cherenkov angle in the LHCb detector are achieved through its RICH system.

Requirements of the RICH detector

The RICH is designed to provide excellent discrimination between charged hadrons, in particular, pions, kaons, and protons (though identification of charged leptons is also possible). This allows the discrimination between different hadronic decays, in particular, processes with similar topologies but different final states e.g. $B^0 \to h^+h^-$ [33] (figure 3.8), $B_c^+ \to J/\psi\pi^+\pi^-\pi^+$ [34], $B^+ \to DK^+$ [35], $B^0 \to K^{*0}\gamma$ [36] and $B_s^0 \to K^\pm\pi^\mp$ [37].

In addition to the discrimination between exclusive decay processes, information from the RICH detector is also used to make more general decisions on whether an event is of interest e.g. identification of events with at least one ϕ particle (which are present in many decay modes of interest). These decisions require significantly less CPU processing than exclusive event selection such that they are well suited to the strict time constraints of the trigger system, see section 3.9.

In a addition to direct processes (where the charged hadron identified is part of the processes being investigated) the particle identification also provides a method of flavour tagging in measurements of CP asymmetries or particle anti-particle oscillations. Such

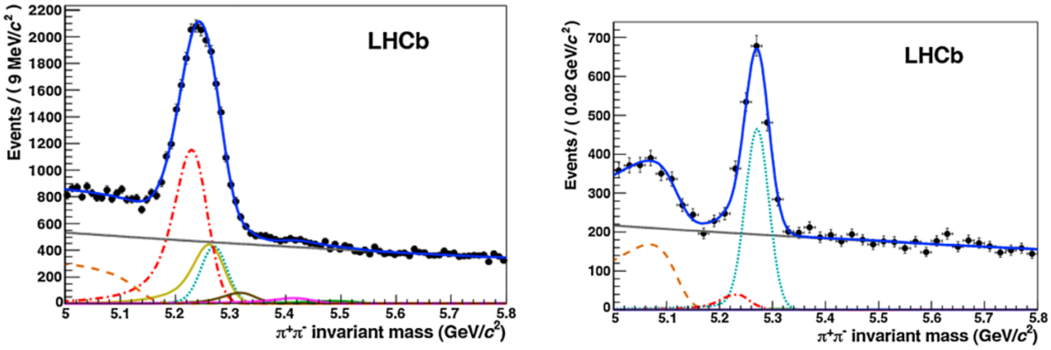

(A) Without RICH information (B) With RICH information

FIGURE 3.8: Invariant mass distribution of $B \to h^+h^-$ decays before (A) and after (B) inclusion of RICH information to isolate the signal decay, $B^0 \to \pi^+\pi-$ (teal dashed). The background processes are $B^0 \to K\pi$ (red dashed-dotted), $B^0 \to$ 3-body (orange dashed), $B_s \to KK$ (yellow), $B_s \to K\pi$ (brown) $\Lambda_b \to pK$ (purple) and $\Lambda_b \to p\pi$ (green). There is also a contribution from combinatorial background (grey).

particles which are used to tag events typically have lower transverse momenta than particles from the decay of heavy B mesons. In order to satisfy the requirements stated previously the RICH must maintain good performance over a large range of momenta (2-100 GeV/c [33]).

Detector Description

The RICH system consists of two RICH detectors, RICH1 and RICH2 [38]. RICH1 is positioned directly downstream of the Vertex Locator (VELO) and upstream of the magnet; it is attached directly to the VELO exit window. RICH2 is positioned downstream of the magnet and Tracking stations (T1, T2 and T3). They are approximately 1 m and 10 m downstream of the nominal interaction interaction point respectively (see figure 3.1), cover an angular acceptance of $\pm(25-300)$ $[\pm(15-120)]$ mrad and momentum range of $2-40$ $[15-100]$ GeV/c see figure 3.10.

In order for Cherenkov radiation to occur a medium with a refractive index $n > 1$ is required. The RICH system employs three different mediums (in the context of RICH detectors these are more commonly referred to as radiators) in order to cover the desired momentum range, see figure 3.9. RICH1 contains both an aerogel and C_4F_{10} gas whilst

RICH2 contains only CF_4 gas. The refractive indices of these are 1.03, 1.0014 and 1.0005 (at 0°, 101 kPa and for photons with a wavelength of 400 nm) respectively.

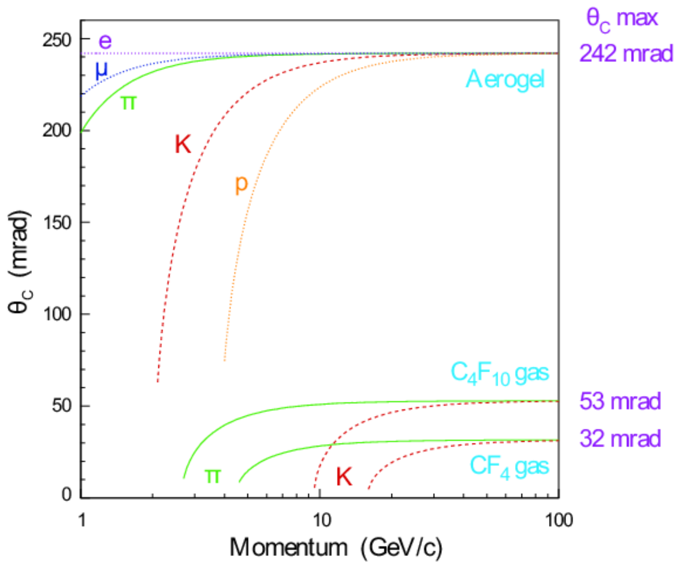

FIGURE 3.9: Cherenkov angle θ_C as a function of particle momentum, particle type and radiator type.

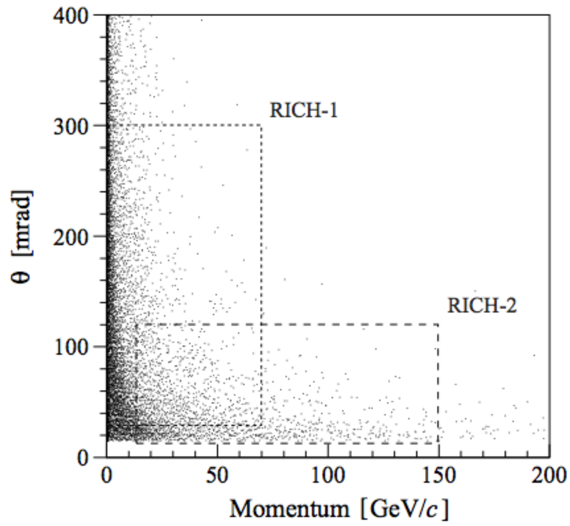

FIGURE 3.10: Polar angle θ and momentum p distribution of the tracks in simulated $B^0 \to \pi^+\pi^-$ decays. The angular coverage and momentum range or the RICH detectors are shown by the regions contained in the dotted lines.

Cherenkov photons emitted by charged particles passing through the radiators in the RICH detectors are emitted at a constant angle relative to the direction of the charged particle, this is referred to as the Cherenkov angle, θ_C. Focusing these photons onto a plane with a parabolic mirror results in rings of photons in which the Cherenkov angle can be calculated from the radius. Both RICH detectors employ similar mirror systems; using a spherical mirror to focus the rings and a plane mirror to reflect the rings onto a plane of photon detectors, see figure 3.11. The purpose of the plane mirrors is to direct photons away from the detector where space limitations, radiation and strong magnetic fields create an undesirable environment for the operation of photon detectors. Each of the mirrors are composed of segments, see table 3.1 and figure 3.12

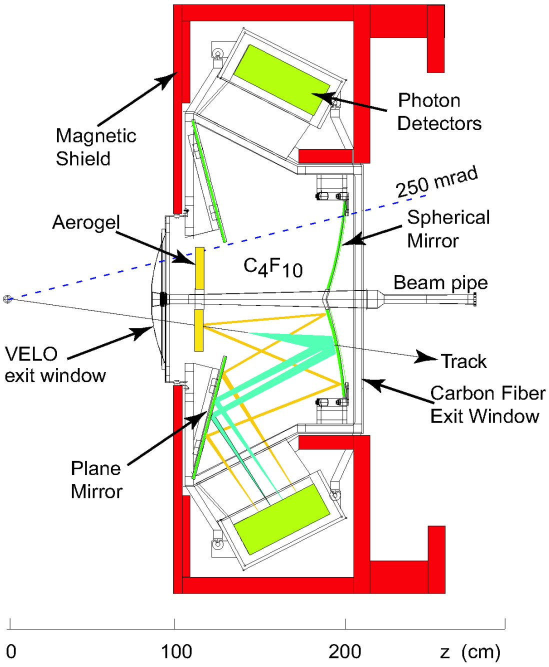

(A) RICH1, side view

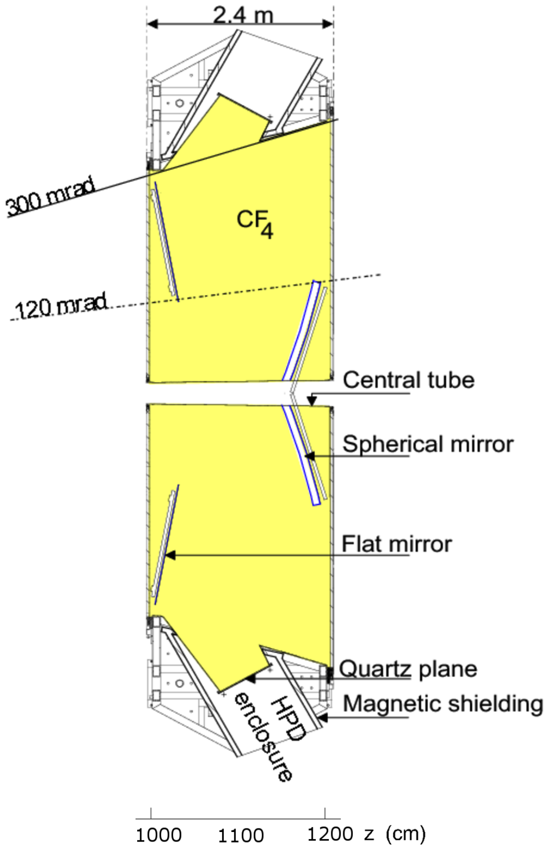

(B) RICH2, top view

FIGURE 3.11: Schematic of the RICH detectors, RICH1 (A) and RICH2 (B). The beam pipe runs left to right in both images.

TABLE 3.1: Spherical and plane mirror segmentation scheme in the RICH detectors.

	Spherical Mirror Segments	Plane Mirror Segments
RICH1	4	16
RICH2	56	40

The photon detector planes are arrays containing Hybrid Photon detectors (HPDs). There are two planes per RICH detector; Up and Down boxes in RICH1 (containing

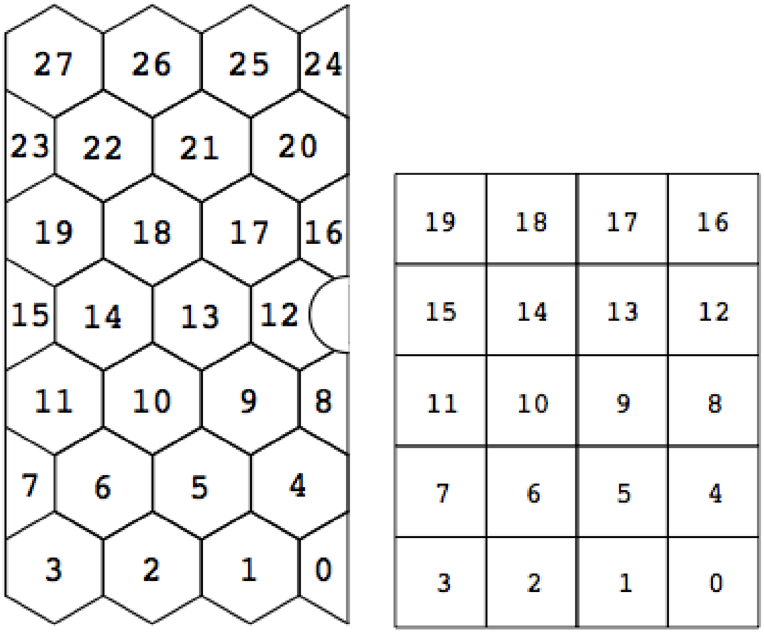

(A) (B)

FIGURE 3.12: Schematic of the spherical (A) and plane (B) mirror segments for the left half of the RICH2 detector. Also shown is the numbering scheme used

additional magnetic shields due to their proximity to the magnet) and the Left and Right boxes in RICH2, see figure 3.11. There are a total of 484 HPDs in the RICH system with 196 of them in the RICH1 detector and 288 in the RICH2 detector.

The entrance to the HPDs consists of a quartz entrance window with a photocathode layer painted on the inner side of the window (see figure 3.13). Photons incident on an HPD stimulate the emission of electrons into a vacuumed cavity inside the HPD via the photocathode layer. These electrons are then accelerated by an electric field across a potential difference of 16 kV onto a 32 x 32 silicon chip array with a pixel size of 2.5 mm x 2.5 mm. The chip records the position of the electron which is used to reconstruct the track of the photon from its emission point in the radiator to photocathode layer on the HPD entrance window. The Cherenkov angle can then be calculated by coupling the photon to its corresponding charged particle and calculating the relative angle between the two.

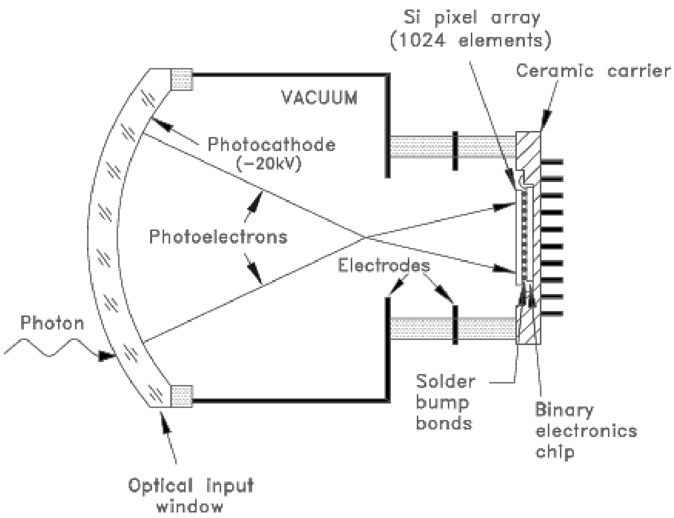

FIGURE 3.13: Schematic diagram of a Hybrid Photon Detector (HPD)

Performance - Cherenkov Angle Resolution

For a medium with refractive index n and where $|\vec{p}| >> m$ the Cherenkov angle becomes *saturated* such that for all particle types the Cherenkov equation (equation 3.2) can be expressed as,

$$\cos\theta_C^{max} = \frac{1}{n} \tag{3.3}$$

such that the Cherenkov angle for all particle types converge,

$$\theta_C^{max}(\pi) = \theta_C^{max}(K) = \theta_C^{max}(p) \tag{3.4}$$

Saturation of the Cherenkov angle in the LHCb RICH detector can be seen in the high momentum regions of figure 3.9. The saturation Cherenkov angles are 242 mrad, 53 mrad and 32 mrad for the Aerogel C_4F_{10} and CF_4 radiators respectively. The alignment of the RICH detector can then be tested by plotting the distribution of the difference between the measured Cherenkov angle and the saturated Cherenkov angle, $\Delta\theta_C = \theta_C$ - θ_C^{max} for photons emitted from saturated tracks.

3.5 Magnet

A dipole magnet is present for momentum determination of charged particles. The magnet provides an integrated downstream field of 3.6 Tm which results in a momentum resolution better than $\delta p/p \approx 0.5\%$ for tracks with momentum less than 200 GeV [39]. The magnet is positioned after the VELO and RICH 1 sub detectors so that the magnetic field does not effect the vertex reconstruction and particle identification of low momentum particles. The structure of the magnet is designed such that the magnetic field does not disrupt the components of other sub-detectors such as the Photon detectors in the RICH systems which use large electric fields. The field lines of the dipole magnet result in a predominantly horizontal Lorentz force on the charged particles in the LHCb detector, consequently tracks are predominantly bent in this plane.

3.6 Tracking

The LHCb tracking system consists of the VELO; the Tracker Turicensis (TT) and the T1, T2 and T3 detectors (collectively called the T-stations), see figure 3.1.

3.6.1 Tracker Turicensis (TT)

The Tracker Turicensis is located before the magnet and after the VELO detector. In addition to charged particles produced in the VELO detector the location of the TT allows it to provide tracking information for charged particles produced from the decay of long lived neutral particles such as the K^0_S which may not decay in the VELO detector. It also provides tracking information for charged particles with low momentum which may not reach the T-stations downstream of the magnet due to the bending of then magnet.

The TT is a silicon micro strip detector with height of 1.5 m and width of 1.3 m, covering the full angular acceptance of the LHCb detector. It consists of 4 layers, the first and last are made up of vertical strips, the second and third inner layers have strips which

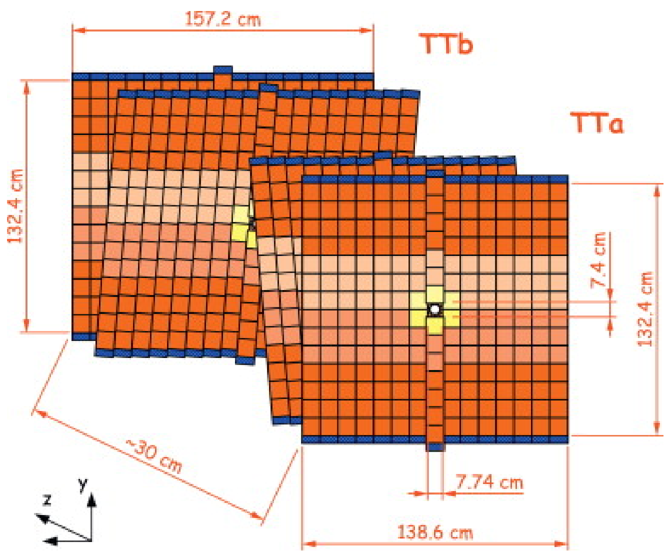

FIGURE 3.14: Layout of the 4 stations which constitutes the Tracker Turicensis

have been rotated by 5 ° and -5 ° stereo angle to provide the transverse position of particles.

3.6.2 T-Stations T1, T2 and T3

The T-stations are positioned after the magnet (see figure 3.1). Together with the tracking detectors upstream of the magnet the trajectory of charged particles through the magnetic field can be measured. The Lorentz force causes the trajectory of charged particles to bend as it traverses the magnetic field; from this the momentum of the track can be measured.

3.6.3 Track Reconstruction

Track reconstruction at the LHCb detector is carried out via several different tracking strategies; generally these involve reconstructing tracks at the sub-detector level called track segments. For example tracks may be reconstructed purely from hits in the VELO sub-detector, these are known as VELO tracks. Similarly tracks may be reconstructed only from hits in the T-stations positioned downstream of the LHCb magnet. These segments may then be combined with hits in other trackers or other track segments to give a more detailed description of the corresponding particle. For example a VELO track segment may be combined with hits from the TT tracker to give an Upstream track, similarly a T-station track segment may also be combined with hits in the TT tracker to give a Downstream track. The possible track types are outline in figure 3.15 and a more detailed description of each of the strategies can be found at [40].

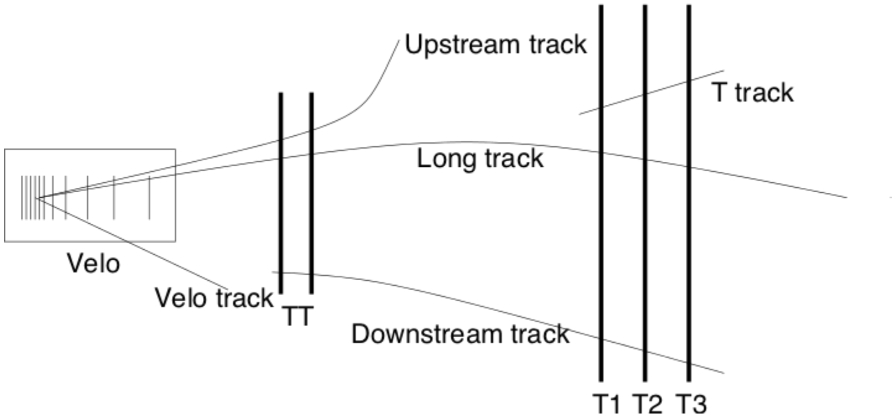

FIGURE 3.15: LHCb Track Types

3.7 Calorimeter

The calorimeter system fulfils several primary roles in the LHCb detector. It provides very fast measurements which are used by the trigger to make quick judgements on an event (a decision is made 4 microseconds after the interaction); examples of such measurements are,

- E_T of electrons, photons and neutral pions
- E_T and $\Sigma(E_T)$ of Hadrons

As well as providing fast information it also provides information on the particle type, discriminating between electrons, photons and hadrons. It is especially useful at identifying neutral particles such as photons and neutral mesons, e.g. pions. This enables the LHCb detector to make physics measurements for many decays, see table 3.2,

The calorimeter system is positioned approximately thirteen metres downstream of the nominal interaction point with a solid angle coverage of 300 mrad in x and 250 mrad

Particle Type	Example Process
Electron	$B \to K * e^{+}e^{-}$
Photons	$B_d \to K * \gamma$ $B_s \to \phi\gamma$
Neutral Mesons	$B_d \to \pi^{+}\pi^{-}\pi^{0}$ $B_d \to J/\psi\eta$

TABLE 3.2: Calorimeter particle identification

in y [41]. It extends for 2.7 metres (See figure 3.1) and is composed of several sub-components. In order of distance from the nominal interaction point these are the Scintillating Pad Detector (SPD), a 2.5 radiation length ($2.5\,X_0$ = 12 mm) lead wall, the Pre Shower (PS), an electromagnetic calorimeter (ECAL) with dimensions of 4 m x 3.5 m and a hadronic calorimeter (HCAL). Each component is designed to maximise the signal of certain particle types and minimise the signal for others. The nominal signal deposition regions for various particle types are shown in figure 3.16

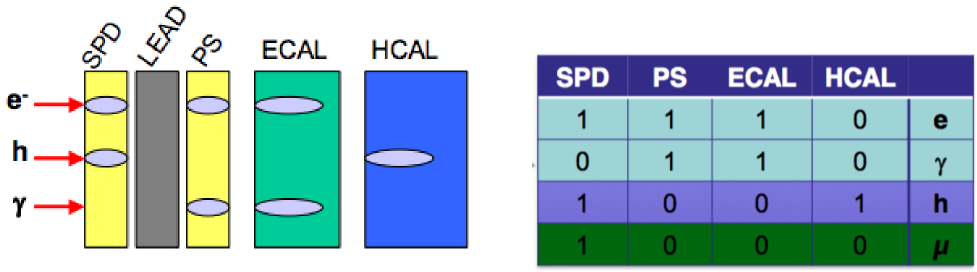

SPD	PS	ECAL	HCAL	
1	1	1	0	e
0	1	1	0	γ
1	0	0	1	h
1	0	0	0	μ

(A) (B)

FIGURE 3.16: (A): Nominal regions of energy deposition in the LHCb calorimeter system for various particle types (B): Nominal particle signal detection in the LHCb calorimeter system for various particle types

TABLE 3.3: Cell granularity structure of the SPD/PS and ECAL components of the LHCb calorimeter system

	Inner region	Middle region	Outer region
Cell size (mm)	40.4	60.6	121.2
Number of channels	1472	1792	2688

The SPD and PS are made from scintillator pads and contain a groove which holds a helicoidal optical fibre that collects scintillating light. The ECAL is a Shashlik electromagnetic calorimeter, it is made of interleaved tiles of 2mm think lead absorbers and 4mm thick scintillator material orientated to face the direction of the beam pipe; there

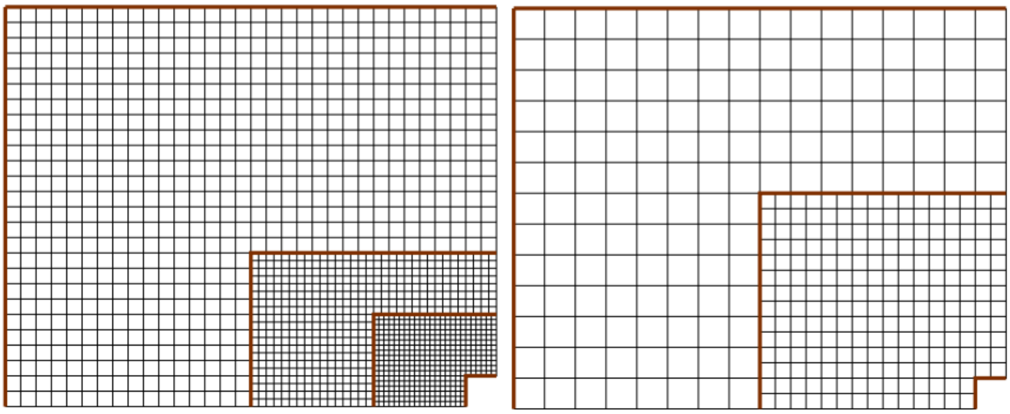

(A) ECAL (B) HCAL

FIGURE 3.17: Schematic of the cell granularity of the LHCb calorimeters for one of its quadrants. See tables 3.3 and 3.4 for further details.

TABLE 3.4: Cell granularity structure of the HCAL component of the LHCb calorimeter system

	Inner region	Outer region
Cell size (mm)	131.3	262.6
Number of channels	860	680

are 66 of these interleaved pairs of lead and scintillator tiles giving a longitudinal size of 25 radiation lengths (X_0). The HCAL is made of interleaved plates of Scandium and Iron and is orientated in the horizontal plane. It has a longitudinal size of 5.6 hadron interaction lengths (λ_I) and is made up of 26 layers of Scandium and Iron plate pairs.

From beam tests [42] the ECAL has been shown to have an energy resolution of,

$$\frac{\sigma_E}{E} = \frac{(8-10)\%}{\sqrt{E}} \oplus 0.9\%$$

and the HCAL has been shown to have a resolution of

$$\frac{\sigma_E}{E} = \frac{69 \pm 5\%}{\sqrt{E}} \oplus 9 \pm 2\%$$

Figure 3.18 shows the invariant masses of particles reconstructed using hits in the calorimeter system.

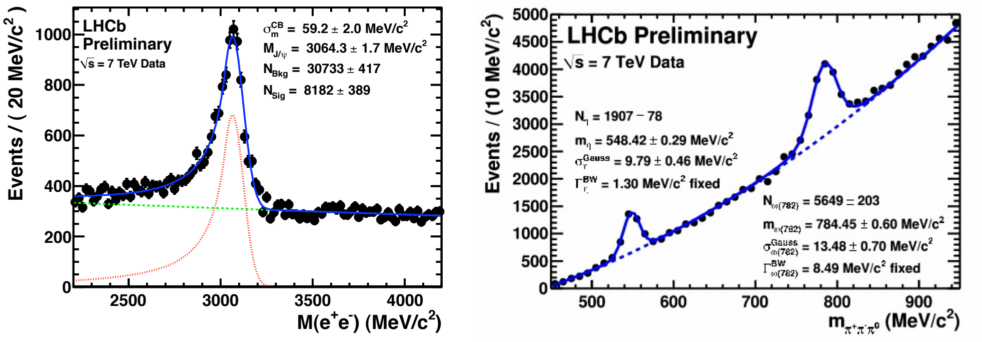

(A) (B)

FIGURE 3.18: Reconstruction of (A) $J/\psi \to e^+e^-$
and (B) $\eta/\omega \to \pi^+\pi^-\pi^0$ using information from the calorimeter system.

3.8 Muon System

Muon detection is an important requirement for the LHCb detector. Muons are present in the final state of many of the key decays that are sensitive to new physics and the rare decays shown in table 3.5, They are also used to determine the flavour of neutral B mesons in electroweak and strong processes.

TABLE 3.5

Process
$B_s^0 \to \mu^+\mu^-$
$B \to J/\psi(\mu^+\mu^-)K_s$
$B_s^0 \to J/\psi(\mu^+\mu^-)\Phi$

To reconstruct these types of events at the LHCb bunch crossing rate (which peaks at 40MHz corresponding to a bunch crossing every 25 ns) the muon system employs a fast stand alone muon reconstruction and passes the information to the hardware trigger (see section 3.9) of the LHCb which applies a minimum p_T requirement (1.5 GeV/c for events with a single muon or a geometrical mean of 1.3 GeV/c for the two muons with the highest p_T in the event). Events triggered on this muon requirement make up $\sim$ 40% of the hardware level trigger output; together with data from the calorimeter system this makes up the bulk.

For the LHCb detector to be competitive in the physics analysis of decays such as shown in table 3.5 a trigger efficiency of $\sim$ 95%, muon identification of $\sim$ 90%, muon misidentification of $\sim 1.5\%$ and muon p_T resolution of $\sim 20\%$ is required together with a timing resolution of ~ 25 ns to match the nominal bunch crossing rate. In addition to this the hardware must be capable of handling the high rates of particles passing through the detector as well as the associated radiation damage.

The Muon System is made up of five stations orientated perpendicularly to the beam axis; these are named M1 through to M5, each consisting of two mechanically independent halves called the A and C side. M1 is positioned before the Pre Shower of the calorimeter system 12.1 m from the nominal interaction point and stations M2-M5 are positioned downstream of the calorimeter system 15.2 m, 16.4 m, 17.6 m and 18.8 m from the interaction point (figure 3.19). Stations M2-M5 are interleaved with 80 cm thick iron absorbers designed to remove hadronic backgrounds giving a longitudinal size of 20 hadron interaction lengths for stations M2-M5 [43]. The geometry of the muon stations is projective to the nominal interaction point; the transverse dimensions scale with distance from the nominal interaction point such that the angular acceptance is the same for all muon stations; $\pm$306mrad in the horizontal plane and $\pm$258mrad in the vertical plane.

Each of the muon stations is divided into four rectangular regions, labeled R1-R4 in order of radial distance from the beam axis (Since the geometry of the muon stations is projective to the nominal interaction point the relative sizes of the regions between each station are the same). These are further subdivided into 276 rectangular chambers of varying size depending on in which region the chamber is located (figure 3.20). The chambers are made up of Multi-Wire Proportional Chambers (MWPC) with the exception of R1 in station M1 which uses triple-GEM detectors(Gas Electron Multiplier) due to higher expected particle rates in this region and the higher levels of radiation tolerance for triple-GEM detectors [44]. This gives a total of 1380 chambers providing a detection area of 435 m^2.

The chambers are further subdivided into logical pads; the dimensions of which vary between muon stations. Stations M1-M3 are used in the muon trigger to calculate the p_t of muon candidates (since muons are more attenuated at the further downstream

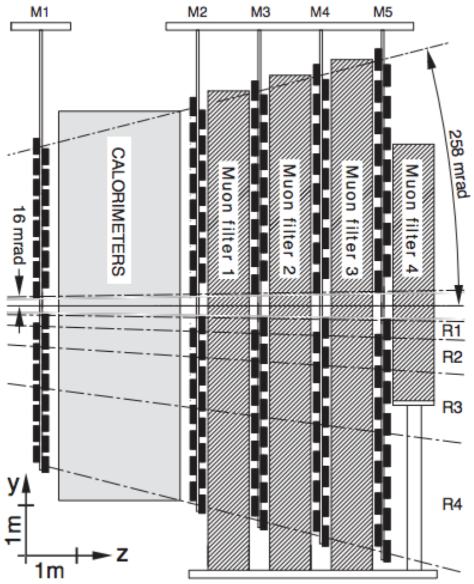

(A) Side view of the muon system

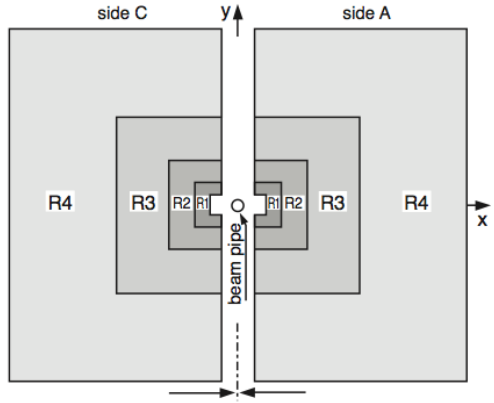

(B) Front view of the muon station regions

FIGURE 3.19: Muon system layout

muon stations) and so the granularity in the bending plane (horizontal) is finer than that of stations M4 and M5 (which are used to identify penetrating muons).

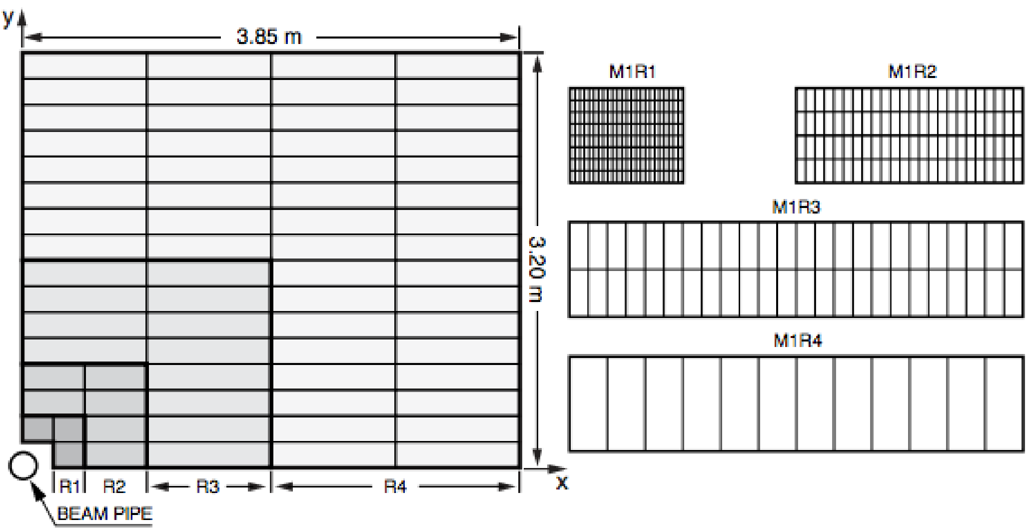

FIGURE 3.20: On the left is a quadrant of the M1 station with the regions R1-R4 shown. Each rectangle represents a chamber. On the right are the chambers for regions, R1-R4 with the logical pad sub-structure shown

Overall the muon system has performed very well during the operation of LHCb achieving if not exceeding the requirements set by the Technical Design Report [45]. In particular efficiencies are well above the design requirements previously described [46], see figure; efficiencies and mis Id rates together with the PID information from the RICH detector can be seen in figure [47]. The momentum resolution achieved from the stand alone muon system reconstruction is 25% and 0.4% with the offline reconstruction using the tracking information [46].

3.9 Trigger

Requirements

The Large Hadron Collider was designed with a nominal bunch crossing rate of 40 MHz corresponding to a bunch crossing rate with at least one visible inelastic proton-proton interaction of $\sim$ 11 MHz [48]. The trigger system is required to select from these events rare interactions such as those involving the production of $b\bar{b}$ pairs, these events are typically characterised by the presence of particles with high transverse energy and momentum corresponding to daughter particles from the decay of the b quarks. To achieve this the trigger translates the raw detector hit information into physical processes and then decides on whether the event is to be kept. The time in which the trigger can achieve this is strictly constrained by the interaction rate in the LHCb detector. This rate is constantly being driven to higher values to get the most out of the detectors and maximise the data taking rate of experiments at the LHC. Such a dynamically changing environment requires an equally robust trigger.

Layout

The trigger system is divided into two levels, the level 0 trigger (L0) and the High Level Trigger (HLT) [49]. The high level trigger is further subdivided into two subsections, HLT1 and HLT2. For an event to pass the trigger it must pass each of the subdivisions in sequence (L0, HLT1, HLT2). Events selected by the trigger are then written to permanent data storage for further processing and analysis.

Level 0 Trigger (L0)

The L0 trigger uses information from the muon and calorimeter systems. It identifies high transverse energy photons, hadrons and electrons from hits in the calorimeter system and high transverse energy muons from hits in the muon system. As the first level in the trigger system the L0 trigger makes more decisions that the following levels, to do this the trigger must be very fast. For this reason the decision algorithm is implemented in hardware with the electronics located inside the experiment and connected by optical fibres. The L0 trigger reduces the event rate from 40 MHz to 1.1 MHz with a maximum latency of $4\,\mu s$

High Level Trigger

The high level trigger is a software implemented trigger system, it runs on the Event Filter Farm (EFF), a network of computers dedicated to making fast decisions about events [50]. The presence of a software based trigger in addition to the hardware based trigger increases the flexibility of the trigger system; providing a simple interface to apply modification of parameters, implementation and computing resources without direct access to the physical components.

The HLT has access to all the raw data from the LHCb detector, this event information is stored in raw banks e.g. energy clusters in the calorimeter system, hits in the tracking system. The HLT system uses a set of algorithms to decode the raw banks into event objects such as vertices, tracks and particles; this is known as the *reconstruction* process. The event objects are passed as arguments to a decision algorithm which determines whether the event is kept depending on the properties of the event objects, e.g. a minimum transverse momentum requirement of particles produced in the event or a minimum impact parameter requirement between a particle and interaction vertex. For events which pass the event selection many of the event objects are stored to file in order to reduced the CPU processing requirements of its later analysis.

High Level Trigger 1 (HLT1)

The HLT1 performs the initial reconstruction defining the vertices and tracks in the event. Its role in the trigger system has varied through the evolution of the experiment, displaying the versatility of the software trigger component of the trigger system. In the 2010 data taking period the role of the trigger was to confirm the decision of the L0 trigger matching the tracks made from the calorimeter and muon system to the VELO and TStation trackers together with other additional checks such as confirming the charge of particles detected at the L0 stage in order to minimise the misidentification of neutral particles. For the 2011 data taking period the HLT1 used a one track approach, basing the decision on the presence of at least one track passing a set of requirements such as, its impact parameter, transverse momentum, track fitting quality etc. For more information see. [49]

High Level Trigger 2 (HLT2)

The HLT2 performs a higher level of reconstruction, matching track segments from each of the sub detector components to form a combined track with improved position and momentum resolution. Basic particle identification is applied these tracks to produce particle objects; this together with reconstruction of secondary vertices enable the reconstruction of both inclusive and exclusive decay channels e.g. $B \to hhhh$ or $B \to DX$.

Offline Processing and Reprocessing

Events which pass the trigger system are written to a permanent file storage system together with the full detector information. Before these data are made available for physics analysis there is an additional offline processing stage. In the offline environment the time requirements for processing each event are lessened allowing for more sophisticated algorithms to be run such as algorithms which decode particle identification information from the RICH system as well as advanced clone killing algorithms.

Having the raw event information stored allows for reprocessing of the event information, this is useful since the reconstruction algorithms are constantly improving as well as the understanding of the detector and its alignment methods. Older data can then be reprocessed, giving event objects with greater resolution on their measurements i.e. are better representations of the corresponding physical particles.

Performance

The trigger system has shown to be flexible and robust during the operation of the LHCb detector adapting to the larger pile-up conditions imposed by the machine delivering 1296 instead of the planned 2622 colliding bunches. The trigger rates of the LHCb detector in 2011 are outlined in table 3.6 [48].

Table 3.6: Trigger output rates during the 2011 data taking period

Trigger	Output Rate (kHz)
L0	870
HLT1	43
HLT2	3

3.10 Computing

The LHCb experiment provides an extremely challenging software environment. Requirements for such a software project include management of both large amounts of data as well as high rates of data; managing software written by a large number of collaborating scientists; managing frequent improvements and changes in algorithms; the ability to provide a common interface between generated data and measured data such that meaningful comparisons can be made; a constantly changing detector environment and the encapsulation of data relevant to a wide range of users.

The LHCb software is based on the Gaudi software architecture and framework [19]. This framework is specifically design for use in the field of high energy physics and based on the concept of object orientated programming. Well defined interfaces are defined between components of the framework so that each component can be modified in a self contained manner without affecting other components. A schematic view of the Gaudi architecture is shown in figure 3.21, describing a typical state of the software model.

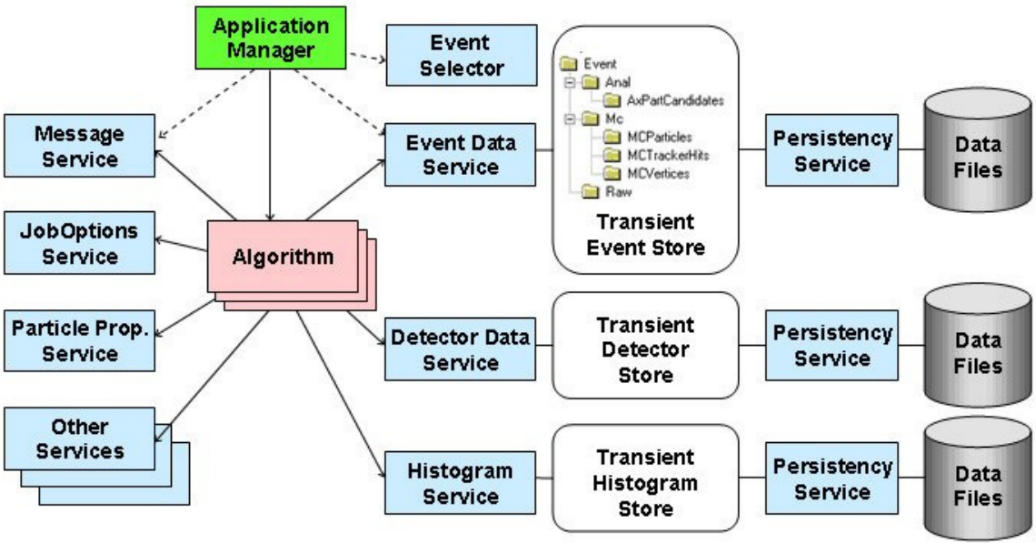

FIGURE 3.21: A state diagram of a typical application build on the Gaudi framework

Unique to Gaudi architecture in comparison to other object orientated frameworks is the distinction between data and algorithms. In the Gaudi architecture algorithms themselves are objects and act on data objects (e.g. A track fitting algorithm acts on detector hit objects to form a track rather than the hits themselves forming a track). The motivation of this approach is shown in the persistency of algorithms and data objects. Algorithms are methods typically used to create objects such as tracks from detector hits; these methods are constantly being improved over the lifetime of the experiment. In contrast to this the models describing data are more stable (e.g. the concept of a track is not expected to change). Making a distinction between the algorithm and data decouples the two enabling the ability to modify the algorithms without affecting the data.

Each phase of the data processing is encapsulated into an application built on the Gaudi framework. Monte Carlo event generation and detector response to the generated particles is handled by the Gauss application, the output of this phase is in the form of detector hits and is used as input for the Boole application. The Boole application applies a detector response to the hits generated by the Gauss application digitising the hits into a format which mimics measured data. Additional hits are added from from Spillover events and LHC background and the digitisation step of the readout electronics, as well as of the L0 trigger hardware are simulated. The next phase of data processing is to reconstruct objects from the digitised hits, this is achieved through the Brunel application. Since the output from Boole is designed such that it models the detector output the algorithms used by Brunel are exactly the same for both generated data and data produced from measured collisions, decoupling the reconstruction phase completely from the generation phase. The output from the reconstruction phase is then proceeded by an analysis phase, the application for this phase is the DaVinci application. This phase is focused on the application of more sophisticated algorithms acting on high level objects such as particles and secondary vertices. This includes the reconstruction of exclusive decay channels and high level background correction. The overall application and data flow is outlined in figure 3.22.

Information about the state of the LHCb detector at a given time is accessed via the Conditions Database service. This information includes such things as the temperature and pressure in certain detector elements as well as the alignment parameters used to describe the detector. The values stored in the database are dependent on several variables such as the time, version and data source of the data; each combination of variables is identified by a unique tag. Similarly information about the structure and materials of the detector elements are accessed via the Detector Descriptions Database and accessed via the Detector Description Service.

To make use of the grid computing service the LHCb software uses the Distributed Infrastructure with Remote Agent's Control project (DIRAC). This together with the job submission application named Ganga, enables users to perform large scale physics

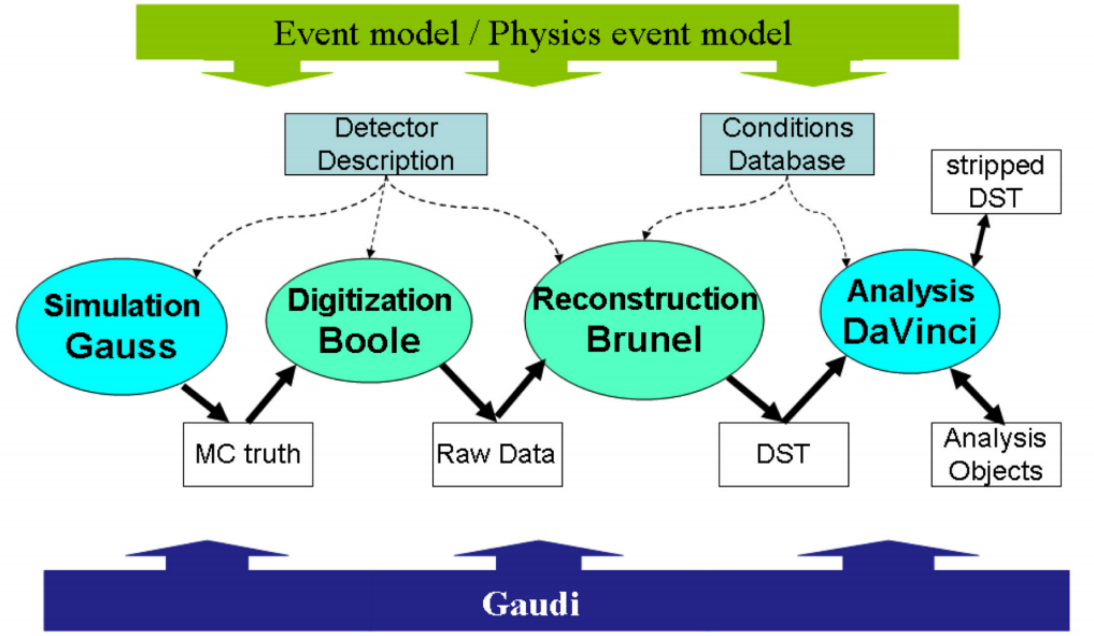

FIGURE 3.22: A schematic of application processes and data flow. Underlying all the applications is the Gaudi framework. The arrows represent the transfer of input and output data.

analysis without having to the need for a complete understanding of the computing challenges behind their physics analyses.

Chapter 4

HPD image centre alignment

4.1 Overview

The Hybrid photon detectors (HPD) are used to detect Cherenkov photons emitted by particles traversing the RICH system. The hit positions of the emitted photons form a ring on the HPD plane, the radius of which is related to the Cherenkov angle associated to the particle. The Cherenkov angle of a particle acts as a signature of its particle type. This enables discrimination between electrons, pions, kaons and protons which is needed to identify the decay processes of particles produced in the LHCb detector.

The HPDs are arrange in two grids, for RICH 1 [RICH 2] the grids are positioned above [left] and below [right] the beamline and are are arranged into rows of 14 [16] by 7 [9] columns (Fig 4.1). The HPDs are approximately cylindrical in shape, with a length of 160 mm and radius of 43.7 mm [1] (See Fig 4.2 and Fig 4.3). A spherically-shaped cap quartz window is attached to one end of the HPD, on its inner surface is a deposition of an S20 (multi alkali) photo-cathode which emits photo-electrons when stimulated by photons. The emitted photo-electrons traverse the vacuum chamber of the HPD where they are accelerated by an electric potential difference of 20 kV onto a square silicon chip array of 32 $\times$ 32 pixels [2] with a length and width of 16 mm.

[1] There are small differences in the dimensions of the HPDs in RICH1 and RICH2. The values given here are for the HPDs in RICH 1, details for the HPDs in RICH 2 can be found in the RICH Technical design report.

[2] When the HPD is run is its ALICE configuration the pixel dimensions are 32 $\times$ 256 pixels

FIGURE 4.1: Upper HPD grid in RICH 1

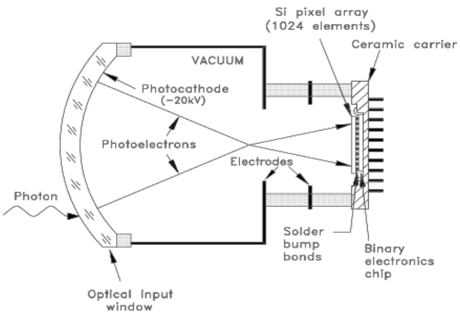

FIGURE 4.2: HPD schematic

FIGURE 4.3: photo of a HPD

The total accumulation of pixel signals over the course of a run can be visualised on a two dimensional plot called a hit map (or image summary fig 4.4). Due to the circular shape of the quartz window the hit map is circular in shape. An image centre is determined by fitting a circle to the boundary of the hit map and taking the central position. The accuracy in the position of the image centre is an important property of the HPD since any translation of the image centre affects the accuracy in the position of the photon, Cherenkov angle and particle identification.

Observations of the image centre show that its position does not necessarily line up with the centre of the silicon chip, this effect is accounted for by an alignment process which reflects the displacement of the image centre from the silicon chip centre in the detector description of the LHCb detector. In addition, during the course of operation, shifts in the position of the image centre for individual HPDs have been consistently observed. These shifts can be as much as 2 mm (Fig 4.5c) between consecutive runs. This phenomenon was further confirmed during and investigation carried out in laboratory

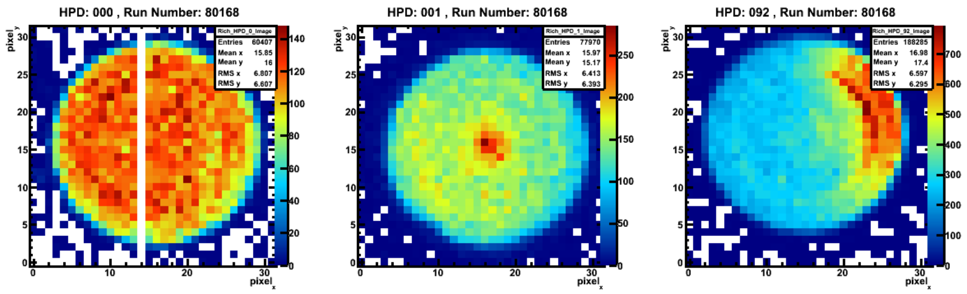

FIGURE 4.4: Example HPD hit maps for HPDs 001, 002 and 092 for run 80168. The z-axis corresponds to the number of hits registered by a pixel, the x and y axes correspond to the pixel position on the silicon chip

tests performed at the end of 2009 using HPDs removed from the LHCb detector for which shifts has been most noticeably observed. The low levels of mechanical stress, scale of the shifts (Fig 4.5) and rigidity of the HPD fixings suggest the image shifts are not due to physical movement of the HPD components, but are instead the result of disturbances to the electric fields due to build up of charge on HPD components over the duration of operation. Additionally shifts were shown to be present across both magnetic field configurations and when the magnet was off suggesting this effect was not an artefact of the magnet.

In addition to the alignment of the HPD image centres the performance of the RICH detector is also dependent on the alignment of its other components. In particular the alignment of the mirrors which reflect the Cherenkov radiation onto the HPD plane and the Magnetic distortion monitoring system (MDCS) which corrects distortion effects to the HPDs due to the magnetic field from the LHCb magnet. These alignment procedures are intimately entangled such that changes in any of the alignment procedures will affect the other. Since improvements in the individual alignment systems are constantly ongoing in parallel it can be difficult to disentangle how the effect of changes in the individual alignment systems affects the RICH system as a whole.

The work presented here builds on alignment techniques performed previously for the data collected in 2010. The main changes were to carry out the alignment on a run by run basis. For the data taking period of 2010 the HPD image centres were calculated by averaging over the whole year. Improvements were also made to the general stability and accuracy of the fit. At the time of writing the current alignment software produces improvements $\sim 7\%$ in RICH1 and RICH2 (section 4.4) compared to the 2010 alignment techniques.

The shifting of images was first noticed in the middle of 2009 [51] most noticeably in a HPD located around the outer corner (HPD: A7 13) of the the A-side HPD plane. The RICH2 HPD intervention in October 2009 was used as an opportunity to extract the HPD to investigate image shifts in a laboratory environment.

The set up for the laboratory tests were chosen so that the conditions were as similar as possible to the conditions in the LHCb detector. Tests were performed over time periods varying from 48 to 450 hours using an LED light source. Figure 4.6 shows the results from a 48 hour period test, Figure 4.6a [4.6b] shows the variation in the row [column] position of the image centre and figure 4.6c shows the variation in the radius of the circle used to fit the HPD hit map. In January 2010 the tests were repeated over a 450 hour period to investigate whether the shifts exhibited oscillatory behaviour, results are shown in figure 4.7, no significant repeating behaviour was observed.

4.2 Image fitting technique

Image fitting is applied to the accumulated hit maps in order to find the centre of the image. A boundary finding procedure is first employed to find the edges of the images, once the boundary is determined a χ^2 minimisation is performed to fit a circle to the boundary. Various boundary finding methods were investigated, two of these are outline below, 1. Threshold boundary fitting and 2. Sobel boundary fitting.

4.2.1 Boundary selection procedure

The boundary selection method uses an iterative algorithm to scan over the hit map scanning from the pixels in the outer region towards the centre. A test is applied to each pixel with a set of criteria to meet, the outermost pixels which pass the test are then marked as part of the boundary of the image. The Sobel boundary fitting method incorporates an additional process applied to the hit map prior to the boundary selection,

FIGURE 4.5: Image centre x,y displacement and shifts for 2010 tagged consecutive runs ranging from 68179 - 80168

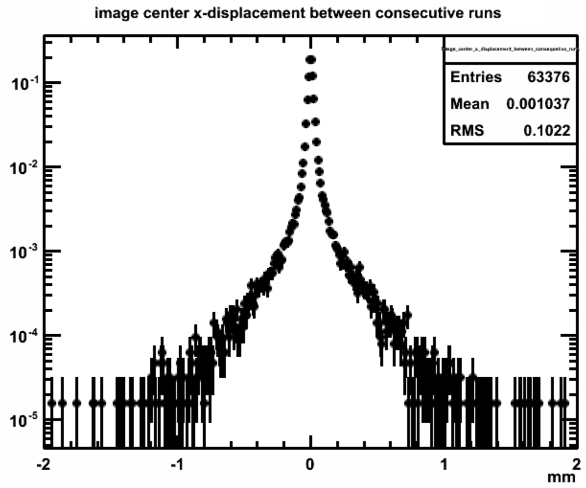

(A) Displacement in x

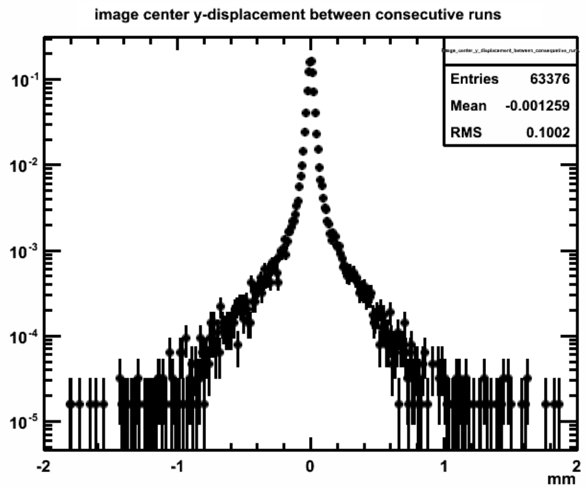

(B) Displacement in y

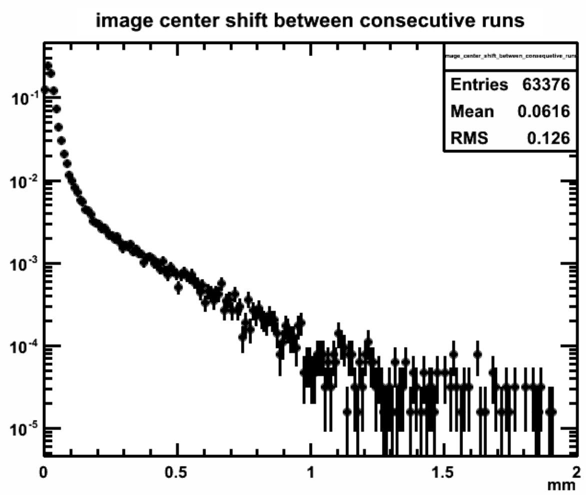

(C) Distance

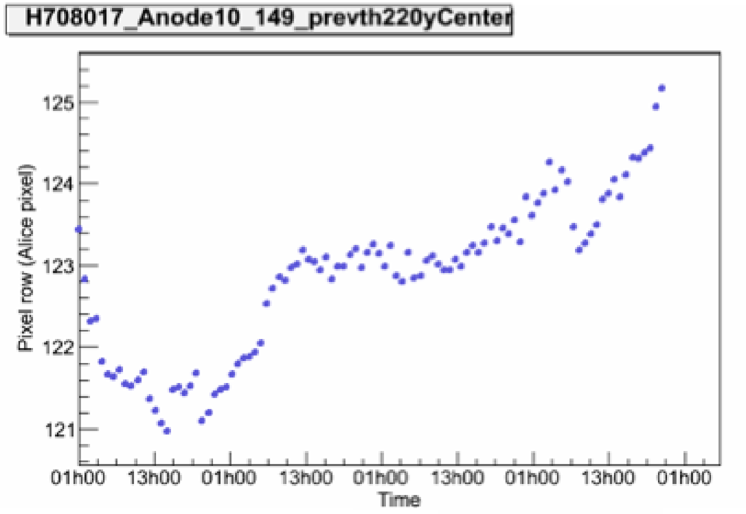

(A) image centre row position, note: lab test were performed with HPD in Alice mode meaning a greater number of effective pixels on the chip (8 Alice pixels to 1 LHCb pixel (0.5mm))

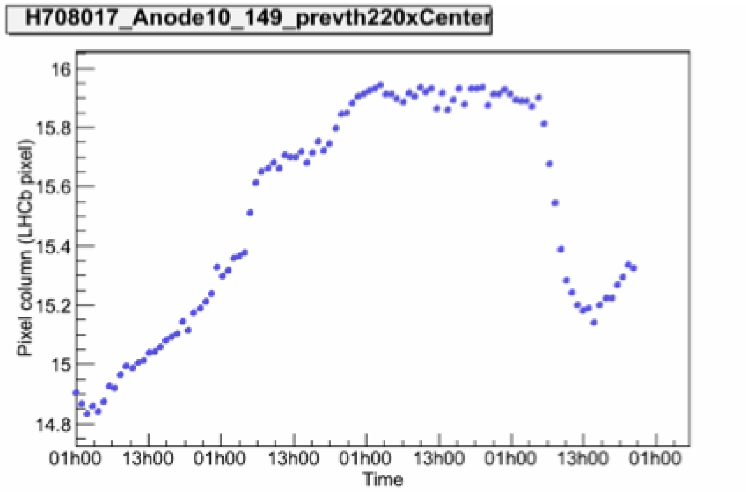

(B) image centre column position

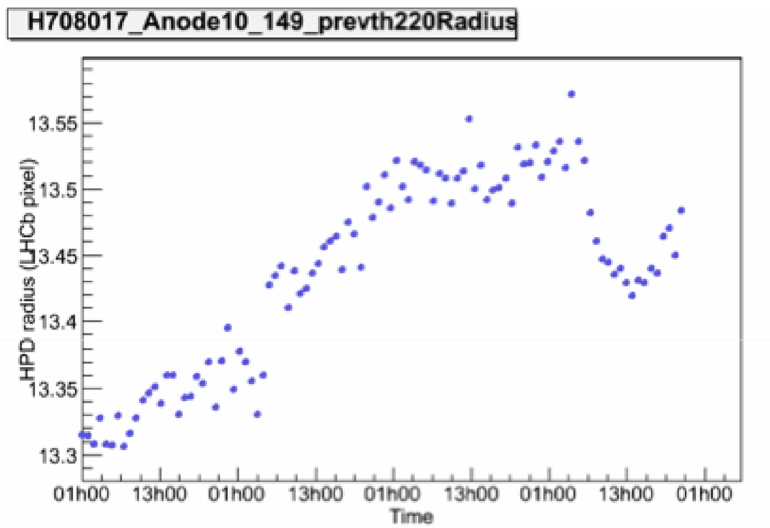

(C) image radius

FIGURE 4.6: HPD A7 13 image shift lab test results over a period of four days

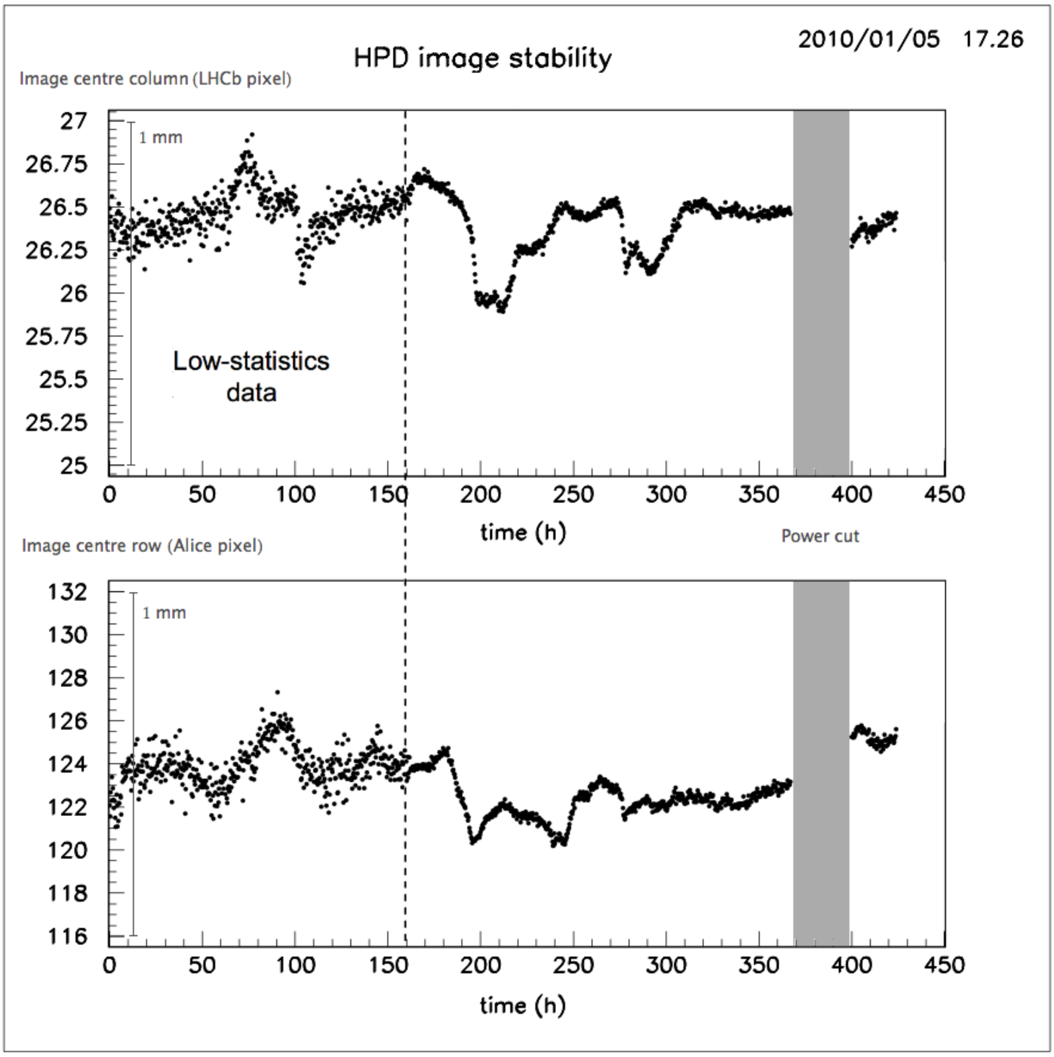

FIGURE 4.7: HPD image centre shift laboratory tests in January 2010. HPDs image shifts were monitored over a 450 hour period

this process emphasises regions in the image with large changes to the image intensity hence emphasising the image boundaries.

4.2.1.1 Threshold boundary fitting

The threshold boundary method uses two criteria to determine the boundary pixels.

Criteria 1

The number of hits for a pixel must pass a user defined threshold parameter. The parameter is defined such that a value of 1 corresponds to the average number of hits per pixel for the HPD image. The optimal threshold value is calculated by comparing the Cherenkov angle resolution as a function of the threshold value.

Criteria 2

At least one of its adjacent pixels must also pass requirement 1, this requirement reduces the contribution of pixels with unexpectedly high population (noisy pixels). This can occur when there is a fault with an individual pixel.

4.2.1.2 Sobel boundary fitting

Similarly to the threshold boundary method the Sobel method also uses a set of criteria to select a boundary, however, before this process a filter is applied to the HPD hit image which maps the intensity (I) of a pixel to its intensity gradient in relation to its adjacent pixels. An example of the Sobel filter being used in the field of image processing can be seen in figure 4.8 and an example of the application of the Sobel filter to a HPD image is shown in figure 4.9. The intensity gradient is calculated by calculating the horizontal and vertical intensity gradients for a pixel and combining them using Pythagoras theorem,

$$\frac{\partial I}{\partial \vec{r}} \approx \sqrt{\left(\frac{\partial I}{\partial x}\right)^2 + \left(\frac{\partial I}{\partial y}\right)^2} \tag{4.1}$$

For a pixel located on row i and column j the horizontal intensity gradient is given by,

$$\left(\frac{\partial I}{\partial x}\right)_{(i,j)} = (I_{(i+1,j-1)} - I_{(i+1,j+1)}) + 2(I_{(i,j-1)} - I_{(i,j+1)}) + (I_{(i-1,j-1)} - I_{(i-1,j+1)}) \tag{4.2}$$

where the first term is equal to the difference between the lower diagonal left and lower diagonal right pixels; the second term is the difference between the left and right pixels weighted by a factor of two; the third term is the difference between the upper diagonal left and upper diagonal right pixels. Similarly for the the vertical intensity gradient,

$$\left(\frac{\partial I}{\partial y}\right)_{(i,j)} = (I_{(i-1,j+1)} - I_{(i+1,j+1)}) + 2(I_{(i-1,j)} - I_{(i+1,j)}) + (I_{(i-1,j-1)} - I_{(i+1,j-1)}) \quad (4.3)$$

where the first term is difference between the lower diagonal left and upper diagonal left pixels; the second term is difference between the lower and upper pixels weighted by a factor of two; the third term is difference between the lower diagonal right and upper diagonal right pixels.

A boundary finding algorithm is then applied to the filtered hit map, the boundary pixels are required to match the following criteria,

Criteria 1

The intensity gradient of a pixel must pass a user defined threshold parameter. The optimal threshold value is calculated by comparing the Cherenkov angle resolution as a function of the threshold value.

Criteria 2

The pixel must be either a peak pixel (adjacent pixels on the same column or row must have a lower intensity gradient) or be adjacent to a peak pixel and have an intensity gradient greater than a user defined threshold value that is related to the intensity gradient of its corresponding peak pixel.

An example of the boundary finding algorithm can be seen in figure 4.10.

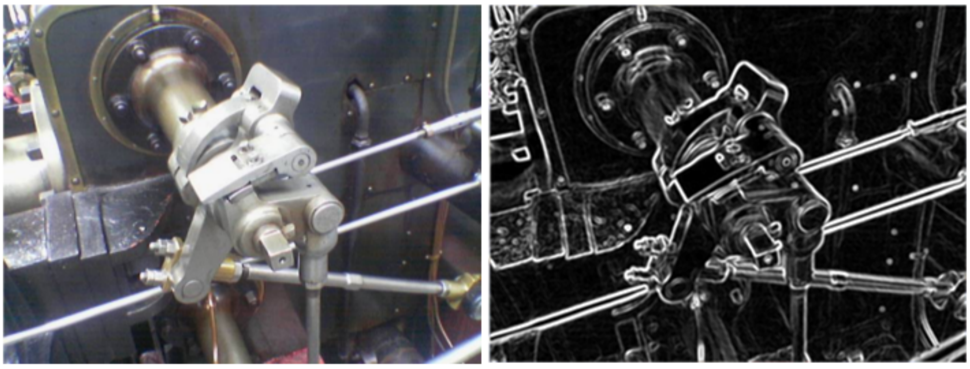

FIGURE 4.8: An example of the Sobel filter in action

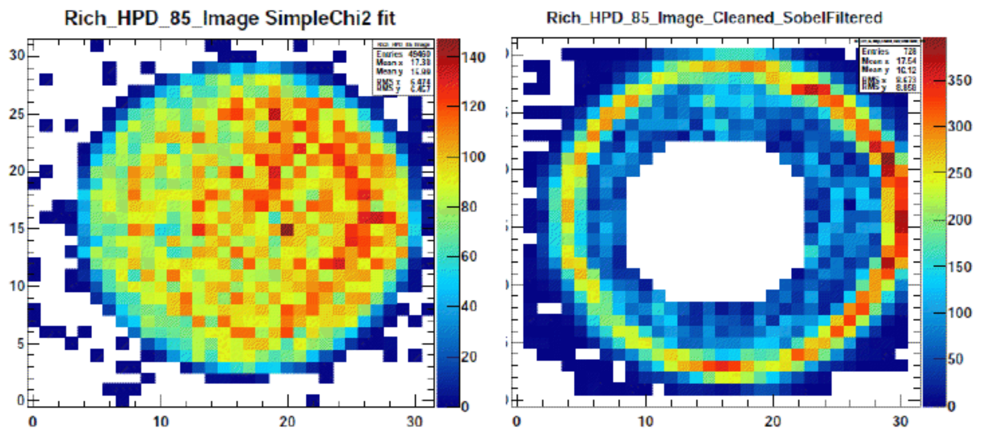

FIGURE 4.9: HPD image summary with Sobel filter applied

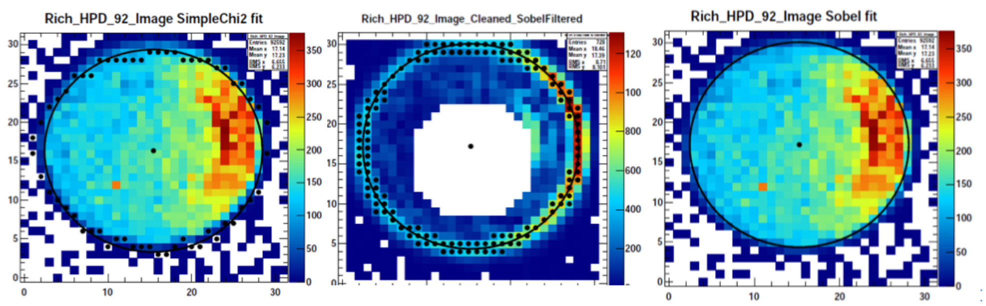

FIGURE 4.10: Boundary fitting comparison: left) 2010, centre) HPD image summary with image cleaning and Sobel filter applied, right) HPD image summary with fitted circle of centre image overlaid

4.2.2 Circle fitting

The circle fitting procedure is carried out by minimising the chi squared function,

$$\chi^2(x_0, y_0, r) = \sum_{n=0}^{N} \left(\sqrt{(x_n - x_0)^2 + (y_n - y_0)^2} - r \right)^2 \cdot I_n \tag{4.4}$$

where x_0 and y_0 correspond to the x and y coordinates of the centre of the circle, r the radius and (x_n, y_n, I_n) are the x, y coordinates and intensity for the boundary pixel n (weighting each pixel by its intensity minimises the contribution from pixels with low photon population). Results for the image centre fitting using both the threshold and Sobel boundary finding techniques are shown in figure 4.10.

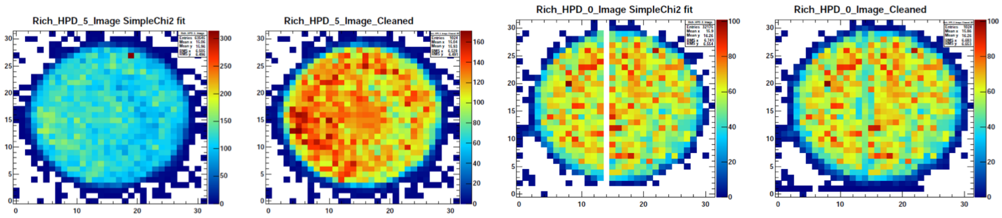

(A) Image cleaning: hot pixel example (B) image cleaning: dead column example

FIGURE 4.11: Other changes to the 2010 fitting code

4.2.3 Additional Image Stabilisation

Defects in individual HPDs can result in undesirable effects in the detection of particles from proton-proton interactions in the LHCb detector. For example, a defective pixel may exhibit a high population of hits which do not correspond to any physics event. These are referred to as hot pixels. Similarly a defective pixels might not detect any signal at all, these are known as dead pixels. To minimise the the effect of these hot/dead pixels on the HPD image centre calculations smoothing is applied to suspected defective pixels (see figures 4.11a and 4.11b).

Hot pixels are determined by comparing the population of a pixel to the average population for a pixel calculated as the sum of pixel hits divided by the total number of pixels. A conservative threshold value is chosen and the central region is not scanned to ensure only defective pixels are selected. Dead pixels are selected from pixels that have no hits but have neighbouring pixels with a population greater than a user defined threshold value. Again a conservative threshold is chosen to ensure only defective pixels are selected.

4.3 RICH resolution

To check the resolution of the RICH detector, the saturation properties of the Cherenkov angle are exploited. Saturated particles are selected with a momentum requirement on the associated track. The RICH resolution is determined from the variable $\Delta\theta$, defined as the difference between the measured Cherenkov angle θ_C and the expected Cherenkov angle θ_C^{exp} for an individual track,

$$\Delta\theta_C = \theta_C - \theta_C^{exp} \tag{4.5}$$

where the measured Cherenkov angle is the direct Cherenkov angle measurement from the RICH detector and the expected Cherenkov angle is calculated from equation 3.3.

This distribution of $\Delta\theta$ is fitted with the sum of a gaussian and second order polynomial, see figure 4.12. The overall RICH resolution is then defined as the width of the gaussian component of the distribution fit.

4.4 Alignment Procedure

The shifts in the HPD image centre are tracked and corrected for in the LHCb conditions database. The database contains information on the environment in the LHCb detector such as the position of detector components. In the database a central axis for each HPD is defined which runs through the centre of its base and centre of its quartz window. To correct for the image shift, the position of the silicon chip array in the plane perpendicular to the central axis is modified such that it is displaced by the displacement vector of the image centre shift.

4.4.1 Run dependent corrections

For data collected in 2010 a global correction to the HPD image centre was applied for all runs. The global correction factor was calculated from the averaged HPD image centre for each run. For the reprocessing of this data in 2011 and the data collected in 2011 a correction per run strategy was implemented. For every run a corresponding database slice is produced containing information on the position correction of the silicon chip array for that run. The idea of a correction per run technique was also investigated during data taking in 2010, however instabilities in the HPD image centre fit resulted in the global averaged correction yielding better performance. These issues were addressed in the software used in 2011. The later version employed a more sophisticated fit method in addition to additional modifications (see section 4.2) as well as general bug fixes.

Figures 4.12 and 4.13 show the distribution of $\Delta\theta$ for tracks produced during run 80168 in 2010 for RICH 1 and RICH2 respectively. The left side of the plots show the distribution of $\Delta\theta$ where the global HPD image shift correction has been applied and the right side of the plots show the distribution where the correction per run method as well as the more recent image fitting methods are used. For RICH 1 the resolution is improved by 7.6% from 1.88 mrad to 1.747 mrad and 4.6% from 0.78 mrad to 0.75 mrad for RICH 2. The order of the improvements in the resolution were found to consistently improve the resolutions with improvements of similar magnitudes for several runs.

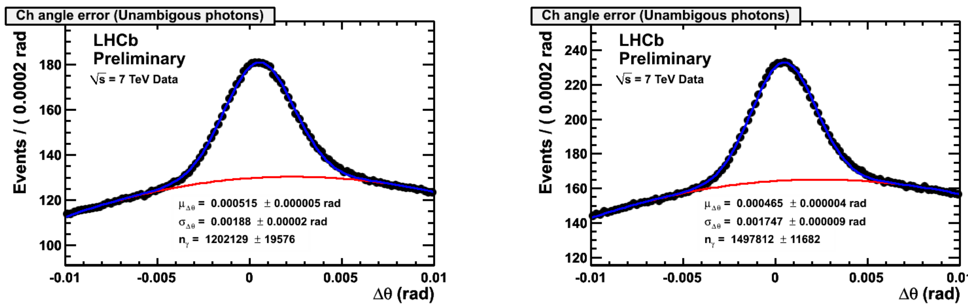

FIGURE 4.12: CK angle reconstructed - CK angle expected for photons from saturated tracks in RICH1 for run 80168. Left) Using 2010 default database values. Right) Using new alignment procedures and run by run corrections

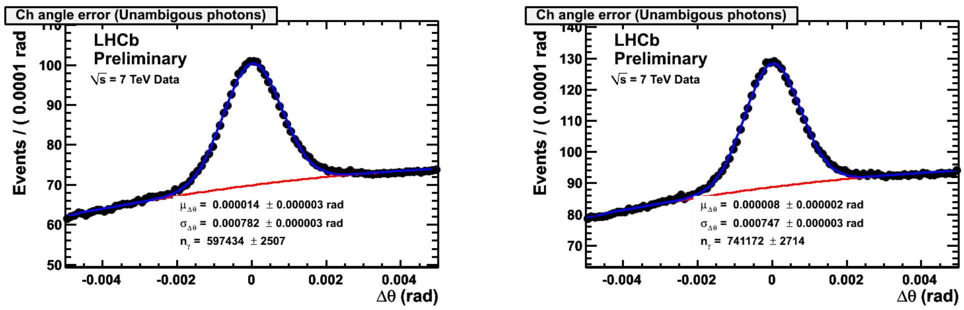

FIGURE 4.13: As with figure 4.12 but for RICH2

4.4.2 Full reconstruction

The full reconstruction of events in the RICH system incorporates the most recent alignment in other parts of the system e.g. the mirror alignment and magnetic distortion calibration. These components are interrelated with the HPD image centre alignment such that improvements in the alignment method of one will propagate to another. The overall improvement in the resolution of the RICH detector can be seen in figures 4.14 and 4.15 for RICH1 and RICH2 respectively. These plots show the distribution of the resolution parameter σ (the width parameter of the Gaussian component of the fit to $\Delta\theta$) for all runs.

Further improvement in the Cherenkov angle resolution is seen in in the case of the full reconstruction with an improvement of 8% in resolution, from 1.75 mrads to 1.62 mrads in RICH1 and 7.4% improvement in resolution from 0.73 mrads to 0.68 mrads in RICH2.

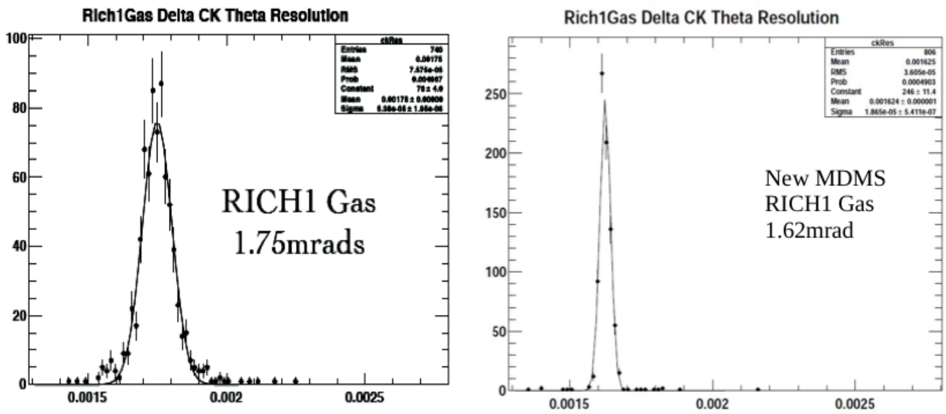

FIGURE 4.14: CK angle resolution for 2010 runs in RICH1. Left) 2010 alignment Right) 2011 alignment

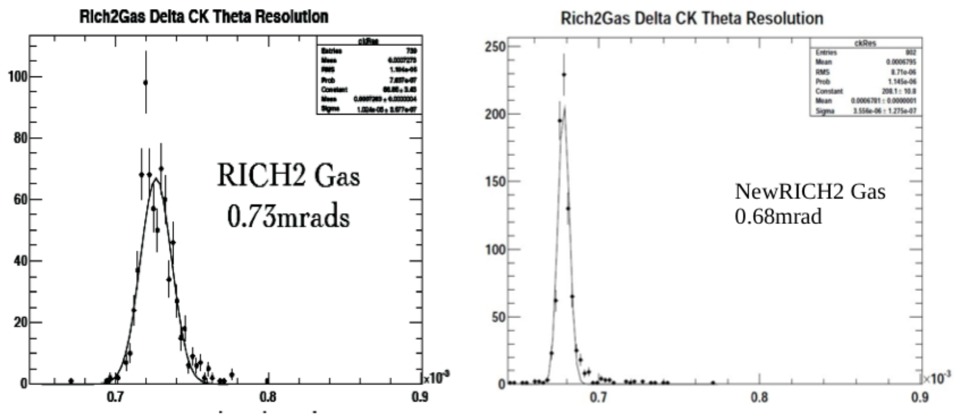

FIGURE 4.15: CK angle resolution for 2010 runs in RICH2. Left) 2010 alignment Right) 2011 alignment

4.4.3 Data from 2011

Table 4.1 shows the result of the 2011 alignment software on the 2011 data taken up to May 2011. The alignment procedure appears to be stable under the change in conditions of the detector.

TABLE 4.1: Mean Cherenkov angle resolution for 2011 data (up to May 2011) using the 2011 alignment software, in mrad

RICH	$<\mu>$ (from MC)	μ
1	1.55	1.63
2	0.68	0.69

4.5 Conclusion

The 2011 alignment software shows significant improvements over the software used in the 2010 alignment. The general fitting stability, accuracy and run dependence monitoring are amongst the key improvements. Over runs from 2010 the improvement in Cherenkov angle resolution is $\sim 8\%$ in RICH1 and $\sim 7\%$ in RICH2 and has brought the average Cherenkov angle resolution much close to the expected Monte Carlo average (see table 4.2).

The improvement in the resolution of the Cherenkov angle correlates to an improvement in the particle identification ability of the RICH system (since the error in the Cherenkov angle is related to the error in the mass of the particle, equation 3.2). This enables the LHCb detector to better identify processes from the decay products of particles produced from the proton-proton interactions, an ability that is especially important for the study of rare decays.

TABLE 4.2: Mean Cherenkov angle resolution for 2010 data, in mrad

RICH	$<\mu>$ (from MC)	μ (2010 software)	μ (2011 software)
1	1.55	1.75	1.62
2	0.68	0.73	0.68

Chapter 5

Multiplicity Distributions of Charged Particles

5.1 Introduction

The LHCb detector provides a unique environment in which to study particle multiplicities providing an opportunity to investigate properties of particle production at a unique energy regime and kinematic range with a high level of precision due to the excellent tracking of the detector. The analysis of the production of charged particles is studied as a function of pseudorapidity and transverse momentum. In addition to this the inclusive particle multiplicity is studied for the whole pseudorapidity and momentum range.

In this chapter the data selection used is discussed followed by the correction procedures used to remove background contributions. The procedures used to correct detector efficiency effects (unfolding) are then considered followed by an overview of the systematic uncertainties associated to each of the correction procedures. The results are then presented together with comparisons to Monte Carlo event generator predictions.

There have been several multiplicity measurements from proton-proton collisions occurring at the LHC, including measurements from the ATLAS [52], CMS [53] and ALICE [54] detectors. The mean charged particle multiplicity measured in these experiments have been shown to be consistently higher than predicted by current MC generators such as PYTHIA. This analysis on data from the LHCb detector is aimed at complementing these results especially by providing insight into regions uniquely accessible to the LHCb detector, in particular, the high pseudorapidity region.

5.2 Prompt Particles

Prompt particles are defined as stable particles produced from the initial proton-proton interaction or from the decay of short lived states that are produced in the initial proton-proton interaction. The set of stable charged particles is composed of electrons, muons, charged pions, kaons and protons. A proper lifetime cut of 0.01 nanoseconds is imposed on a decay process such that only stable particles from processes with a combined lifetime less than the cut are considered. Under this definition charged particles from the decay of K_s and Λ mesons which have mean lifetimes of 0.08954 ± 0.00004 ns and 0.2632 ± 0.002 ns respectively, are not classified as prompt particles.

The η and p_{T} distributions of prompt particles over the full kinematic range (i.e. excluding any detector acceptance cuts) calculated from MC data is shown in figure 5.1.

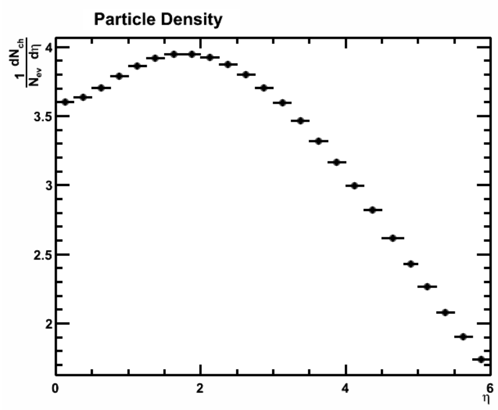

(A) η

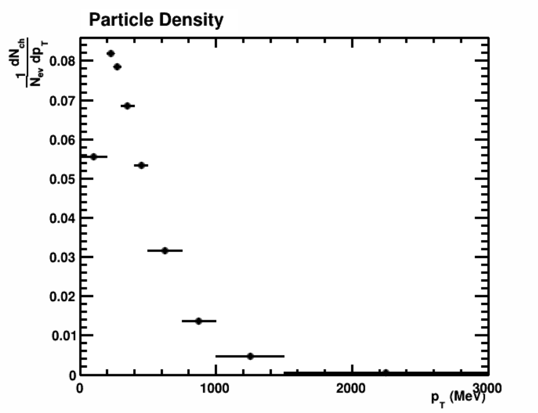

(B) p_{T}

FIGURE 5.1: Probability density distributions of prompt particles as a function of the kinematic variables η and p_{T}. The distributions are calculated from data generated using PYTHIA v6.4 with the LHCb parameter set and without any detector acceptance selection criteria on the particle selection.

5.3 Data and Trigger

The data used for this analysis was recorded in May 2010 at a centre of mass energy of 7 TeV. The average number of proton-proton collisions per bunch crossing during this period of data taking was estimated as less then 0.1. As a result the dataset is dominated by events involving a single proton-proton interaction; with only a small contribution of events with multiple proton-proton interactions. The data is separated into two subsets: events recorded with the LHCb magnet field down or up. The dataset consists of 5.8 million and 12.2 million events respectively for down and up magnet configurations. The Monte Carlo simulated data are also divided into magnet up and magnet down configurations, both consisting of 35 million events. The simulated events are constrained to events with only one proton-proton interaction in order to emulate the data.

The track selection consists of long tracks (see section 3.6.3) together with several kinematic requirements that select tracks from regions where the detector efficiency is high and background contributions are small. A momentum requirement of $p \geq 2$ GeV and $p_T \geq 0.2$ GeV removes low momentum tracks; pseudorapidity requirement of $2.0 \leq \eta < 4.8$ selects tracks corresponding to particles that have transversed a greater number of tracking stations due to the geometry and positioning of the tracking stations, and a requirement on the proximity of the track to the mean interaction region (described in the section 5.4). These selections require that the minimum distance between the track and mean interaction region (Distance Of Closest Approach, DOCA) is 2 mm and that the the track is within 3 standard deviations of the mean z position of the mean interaction region (figure 5.2). This requirement ensures that particles that are produced far away from the interaction region (i.e. unlikely to be prompt particles) do not pass the selection. The track selections are shown in figure 5.2

Due to the low luminosity during this data taking ($\sim 1 \times 10^{30}/\text{cm}^2/\text{s}$) period the L0 trigger 3.9 accepted all events meaning only the HLT was used to select events. The trigger requirements for the data are minimal, requiring at least one selected track is reconstructed in events where the beams are registered as crossing.

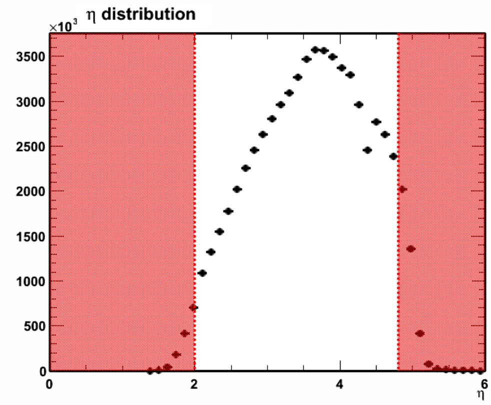

(A) η. The shaded regions correspond to the acceptance boundaries of the LHCb detector, in these regions there is a significant loss in the particle reconstruction efficiency which is coupled with an increase in background contributions.

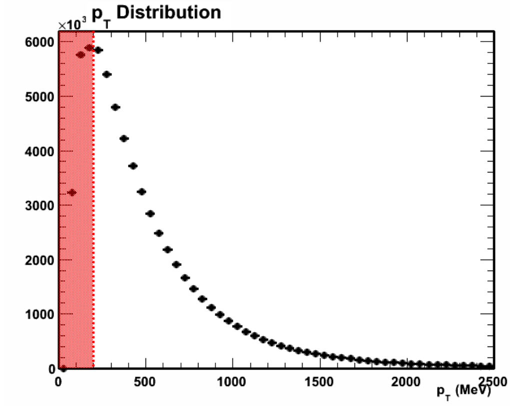

(B) p_T. The shaded region corresponds to tracks with low momenta that do not traverse the full detector due to bending from the LHCb magnet.

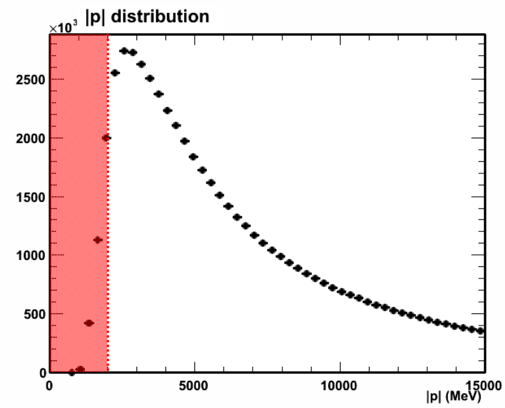

(C) $|p|$. The shaded region corresponds to tracks with low momenta that do not traverse the full detector due to bending from the LHCb magnet.

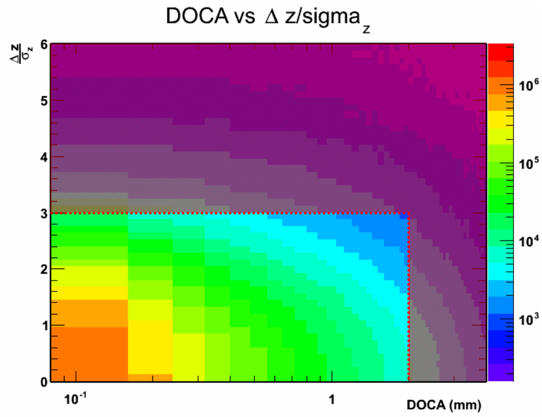

(D) Interaction region. The shaded region corresponds to particles which originate from outside the nominal interaction region, such as from the decay products of long lived particles.

FIGURE 5.2: Track selection criteria. The excluded regions are shown in the shaded red areas and correspond to regions with large background contributions or low tracking efficiency.

5.4 Interaction Region

The mean interaction region is described by two quantities, the beam line and the luminous region. The beamline is a vector quantity defined as being the axis along which the average proton-proton interactions occurs. This is calculated by plotting the x and y distribution of the primary vertex position as a function of z and fitting them with a first order polynomial, see figures 5.3a and 5.3b. From these fits an equation of the beam line can be determined, the minimum distance between the track and the beam line gives the distance of closest approach (DOCA) between the track and beam line.

The luminous region describes the range of z values in which the proton-proton interactions occur. This is calculated by plotting the z distribution of the primary vertices and fitting this distributions with a Gaussian giving its mean position and corresponding standard deviation from it, see figure 5.3c.

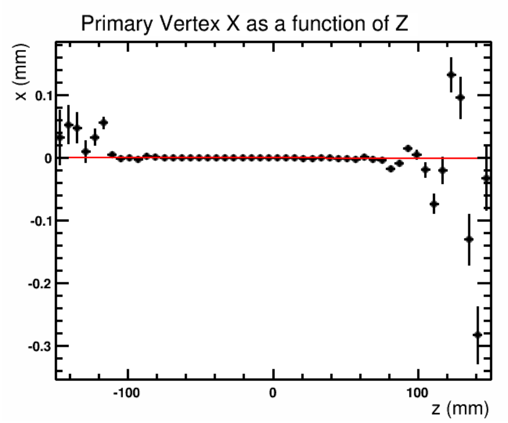

(A) $\langle PV_x \rangle$ as a function of PV_z. This distribution demonstrates how the position of the primary vertex in the x direction varies with where along the beam axis the interaction occurs - it has been fitted with a first order polynomial.

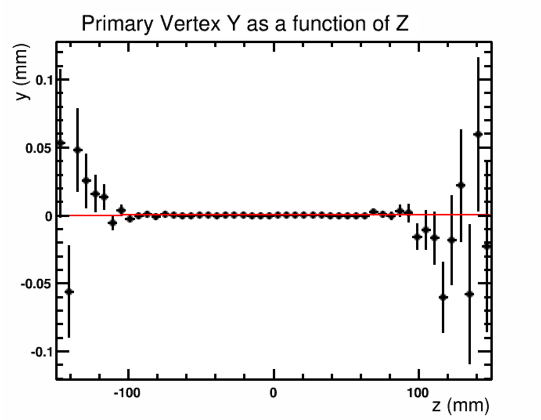

(B) $\langle PV_y \rangle$ as a function of PV_z. This distribution demonstrates how the position of the primary vertex in the y direction varies with where along the beam axis the interaction occurs - it has been fitted with a first order polynomial.

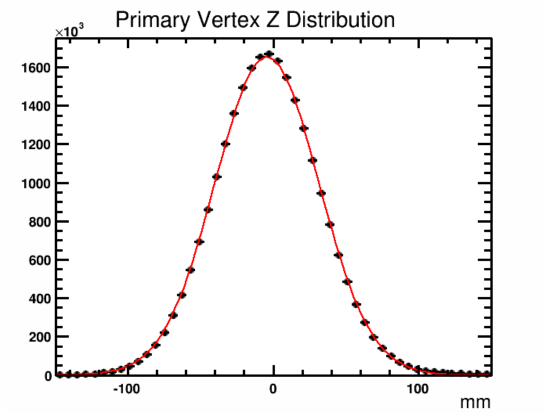

(C) PV_z. This distribution demonstrates the variation in the position of the primary vertex in z - it has been fitted with a Gaussian function.

FIGURE 5.3: PV distributions of MC data in the magnet down configuration

5.5 Charged Particle Density

The charged particle density is investigated as a function of pseudorapidity and transverse momentum. The uncorrected distributions are shown in figure 5.4a and 5.4b for pseudorapidity and transverse momentum respectively. Comparisons between measured data and MC data are shown in figure 5.5.

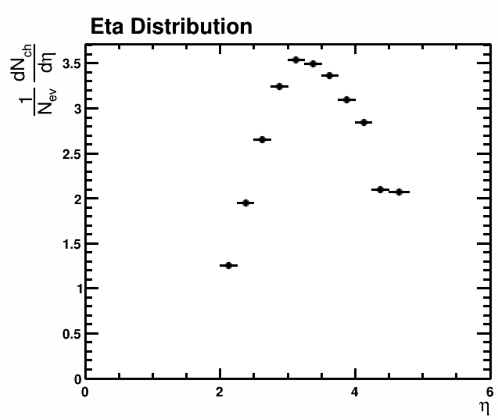

(A) η

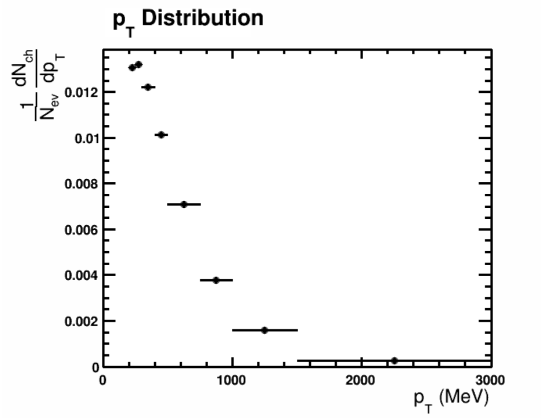

(B) p_T (MeV)

FIGURE 5.4: Uncorrected reconstructed track η and p_T of magnet down data for tracks with $2.0 < \eta < 4.8$ & $p_{\mathrm{T}} >= 200$ MeV & $|p| >= 2000$ MeV & $\mathrm{DOCA}_{\mathrm{beamline}} < 2$ mm & $\Delta z/\sigma_z < 3$ where $\mathrm{DOCA}_{\mathrm{beamline}}$ is the minimum distance between the track and the beamline, Δz is the distance in z between the nominal interaction region and the track's closest position to the beamline and σ_z corresponds to the width of the nominal interaction region.

The true distributions are obscured by detector effects such as detection inefficiencies or the reconstruction of fake tracks. In order to make a measurement of the true distribution several correction procedures are applied. Firstly a background correction is applied to remove the contributions from tracks that are not associated to any true particle but are instead due to mis-reconstruction effects, secondly an efficiency correction is applied which corrects for prompt particles that are not reconstructed i.e. not observed by the detector. This may be due to charged particles being bent outside of the detector by the magnetic field therefore not leaving any trace in the sub-detectors downstream of the magnet, particles that do not induce enough of a response from the detector to be reconstructed or particles that traverse non-sensitive components of the detector. Lastly a pile-up correction is made in order to remove the contribution from events where there are multiple proton-proton interactions i.e. giving a measurement of the charged particle density for single proton-proton interaction events only.

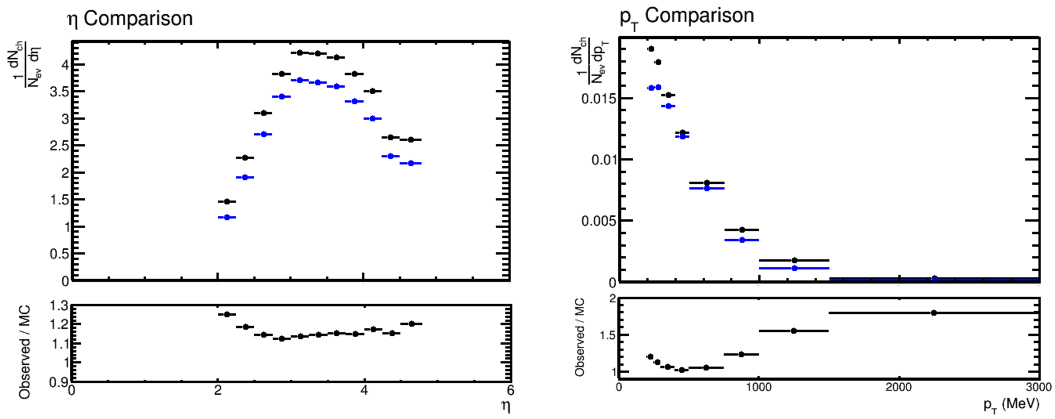

(A) η (B) p_T (MeV)

FIGURE 5.5: Comparison between measured data and MC generated data of the uncorrected reconstructed track η and p_T of magnet down data for tracks with $2.0 < \eta < 4.8$ & $p_T >= 200$ MeV & $|p| >= 2000$ MeV & $\text{DOCA}_{\text{beamline}} < 2$ mm & $\Delta z/\sigma_z < 3$ where $\text{DOCA}_{\text{beamline}}$ is the minimum distance between the track and the beamline, Δz is the distance in z between the nominal interaction region and the track's closest position to the beamline and σ_z corresponds to the width of the nominal interaction region. MC data is shown in blue.

5.5.1 Background Corrected Distributions

The main sources of the background contributions are shown in table 5.1.

TABLE 5.1: Background track classifications

Ghost track	Tracks which are either a) not associated to any corresponding true particle either from the initial proton-proton interaction or from their interactions with detector material and magnetic fields b) has only a small fraction of hits associated from a true particle.
Material track	Tracks which are a result of the interaction between particles from the initial proton-proton reaction and detector material. In MC simulated data material tracks are determined by tracks which are associated to particles that are not involved in the generator level event description
Secondary track	Tracks associated to true particles which do not meet the prompt particle requirement
Clone track	Tracks associated to true prompt particles and share the same association with other tracks in the event

To correct for background contributions the mean purity, p is calculated as a function of η, p_{T}, n_{VELO}, n_{t} , where n_{VELO} is the number of VELO tracks (Tracks that are reconstructed from only hits in the VELO sub-detector, see section 3.3) reconstructed

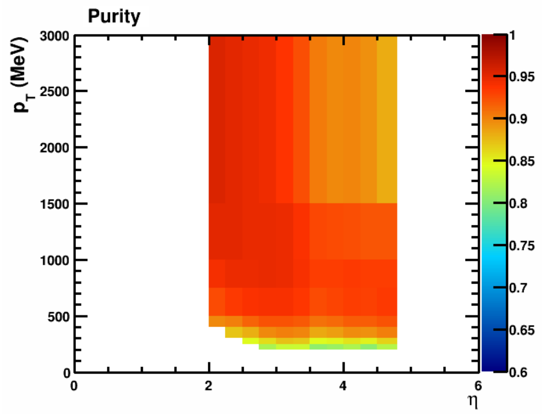

(A) Signal - a prompt particle reconstructed in any η/p_{T} bin in the event

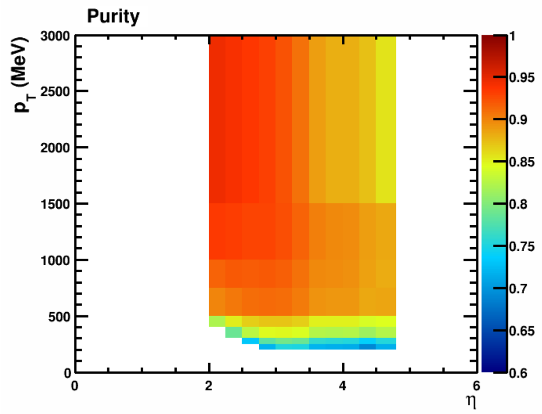

(B) Signal - a prompt particle reconstructed in the same bin as its associated track

FIGURE 5.6: Signal weights as a function of η and p_T for particles with $2.0 < \eta < 4.8$ & $p_{\mathrm{T}} >= 200$ MeV & $|p| >= 2000$ MeV calculated from MC generated data.

in the event and n_{t} is the number of hits in the T-stations (section 3.6) for the event. The purity is calculated from MC data using truth information to determine signal tracks. The purity is given by,

$$p(\eta, p_{\mathrm{T}}, n_{\mathrm{VELO}}, n_{\mathrm{t}}) = \frac{n_{\mathrm{mat}}(\eta, p_{\mathrm{T}}, n_{\mathrm{VELO}}, n_{\mathrm{t}})}{n_{\mathrm{reco}}(\eta, p_T, n_{\mathrm{VELO}}, n_{\mathrm{t}})} \tag{5.1}$$

where n_{mat} is the number of tracks matched to a prompt particle in the same η, p_T and n_{velo} bin. The background corrected η and p_T distributions are calculated by weighting each track by the purity corresponding to the η and p_T bin it is in as well as the n_{velo} and n_{t} bin for the event. Figure 5.6 shows the purity as a function of pseudorapidity and transverse momentum as well as the binning scheme which was chosen to minimise migration effects - particles which are reconstructed as tracks in a different $\eta - p_{\mathrm{T}}$ bin to the $\eta - p_{\mathrm{T}}$ bin of the particle.

Similarly the background rates can be calculated for each of the sources of background in order to gauge the main sources of background, see figure 5.7. The largest source of background is from ghost tracks with a background rate of the order of 10% whilst the contributions from secondary and material tracks are of the order of 4% , finally the contributions from clones are the smallest and are of the order of 0.1%. The clone tracks are predominantly localised in the region $3.5 \leq \eta \leq 4.0$; analysis of MC data

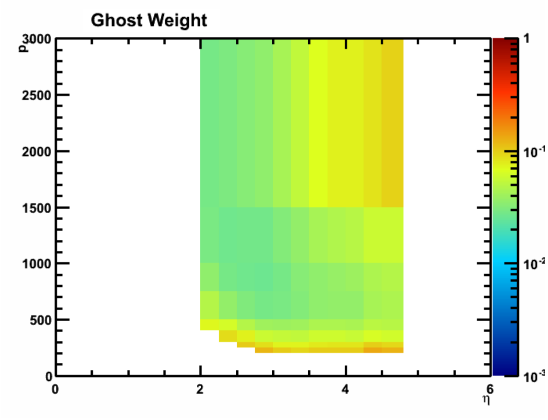

(A) Ghost Rate

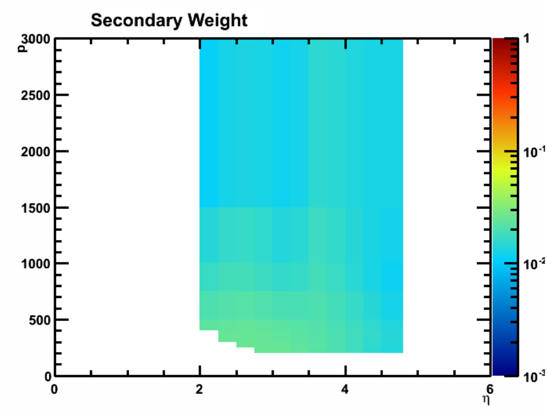

(B) Secondary Rate

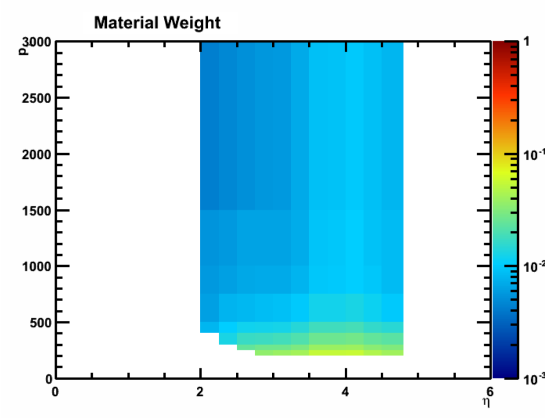

(C) Material Rate

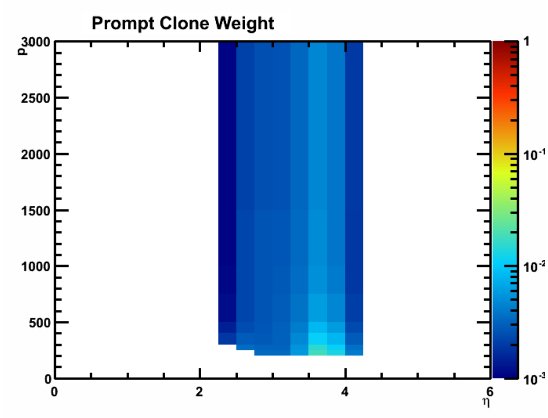

(D) Clone Rate

FIGURE 5.7: Background Rates for tracks with $2.0 < \eta < 4.8$ & $p_{\mathrm{T}} >= 200$ MeV & $|p| >= 2000$ MeV & $\mathrm{DOCA}_{\mathrm{beamline}} < 2$ mm & $\Delta z/\sigma_z < 3$ where $\mathrm{DOCA}_{\mathrm{beamline}}$ is the minimum distance between the track and the beamline, Δz is the distance in z between the nominal interaction region and the track's closest position to the beamline and σ_z corresponds to the width of the nominal interaction region. This is calculated from MC generated data.

suggests this is due to the geometry of the VELO detector. In this pseudorapidity range it is highly probably that a particle will pass through two separated sets of modules (see figure 3.3). Two tracks may be reconstructed, one from the hits in the first stations and one from the hits in the second station - producing two clone tracks. Outside of this range the probability of clone tracks being reconstructed rapidly drops as shown in figure 5.7d.

The background corrected distributions are shown in figure 5.8. A comparison between the background corrected distributions in measured data and MC data is shown in figure 5.9. The dip shown in the pseudorapidity range $4.0 \leq \eta \leq 4.3$ is due to the flange [29] in the LHCb detector, this presents additional non-sensitive detector material, decreasing the reconstruction efficiency in this region.

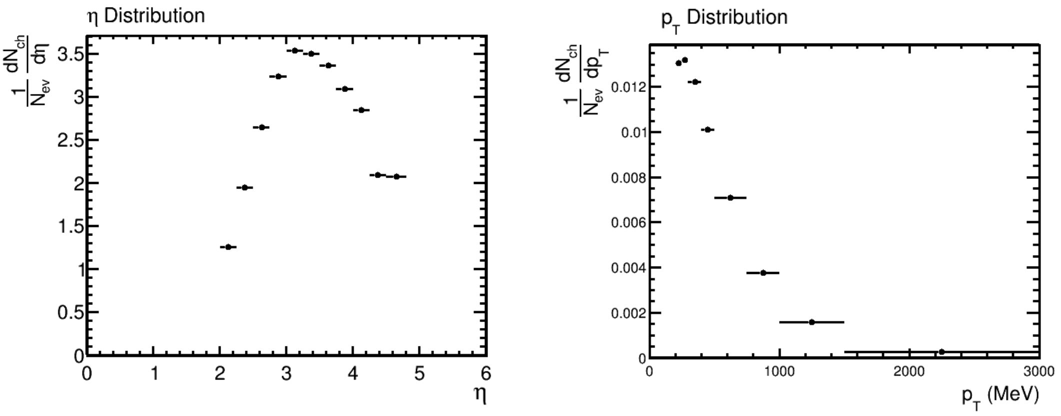

(A) η (B) p_T

FIGURE 5.8: Background corrected track distributions for tracks with $2.0 < \eta < 4.8$ & $p_{\mathrm{T}} >= 200$ MeV & $|p| >= 2000$ MeV & $\mathrm{DOCA_{beamline}} < 2$ mm & $\Delta z/\sigma_z < 3$ where $\mathrm{DOCA_{beamline}}$ is the minimum distance between the track and the beamline, Δz is the distance in z between the nominal interaction region and the track's closest position to the beamline and σ_z corresponds to the width of the nominal interaction region.

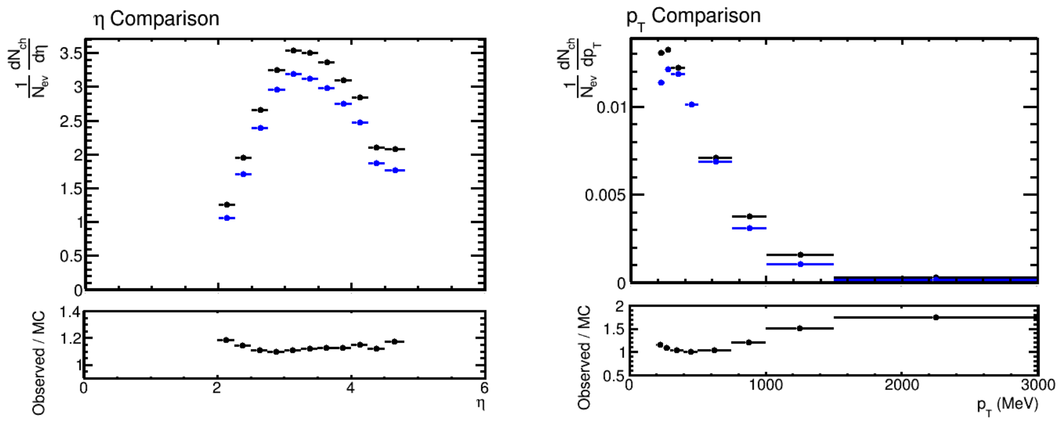

(A) η (B) p_T

FIGURE 5.9: Comparison of background corrected track distributions, MC (blue) and measured data (black) for tracks with $2.0 < \eta < 4.8$ & $p_{\mathrm{T}} >= 200$ MeV & $|p| >= 2000$ MeV & $\mathrm{DOCA_{beamline}} < 2$ mm & $\Delta z/\sigma_z < 3$ where $\mathrm{DOCA_{beamline}}$ is the minimum distance between the track and the beamline, Δz is the distance in z between the nominal interaction region and the track's closest position to the beamline and σ_z corresponds to the width of the nominal interaction region. The lower plot shows the ratio between measured data and MC generated data.

5.5.2 Efficiency Corrected Distributions

The efficiency correction corrects for prompt particles that are not detected by the detector. It is calculated by first modelling the detector response from Monte Carlo data using the truth information to associate tracks to generator level particles. The detector response is independent of the generator model used to create the simulated event so as to not introduce biases. As with the background rate, the efficiency is calculated in bins of pseudorapidity, transverse momentum, VELO track (section 3.15) multiplicity and t-station hit multiplicity. The efficiency in a given bin is given by,

$$\epsilon(\eta, p_{\mathrm{T}}, n_{\mathrm{VELO}}, n_{\mathrm{t}}) = \frac{n_{\mathrm{mat}}(\eta, p_{\mathrm{T}}, n_{\mathrm{VELO}}, n_t)}{n_{\mathrm{true}}(\eta, p_{\mathrm{T}}, n_{\mathrm{VELO}}, n_{\mathrm{t}})} \tag{5.2}$$

averaged over all events. Here n_{mat} is the number of tracks matched to prompt particles in the same η and p_{T} bin as before with the purity and n_{true} is the number of prompt particles in the η and p_{T} bin. The efficiency as a function of pseudorapidity and transverse momentum is shown in figure 5.10 averaged over all bins in n_{VELO} and n_{t}.

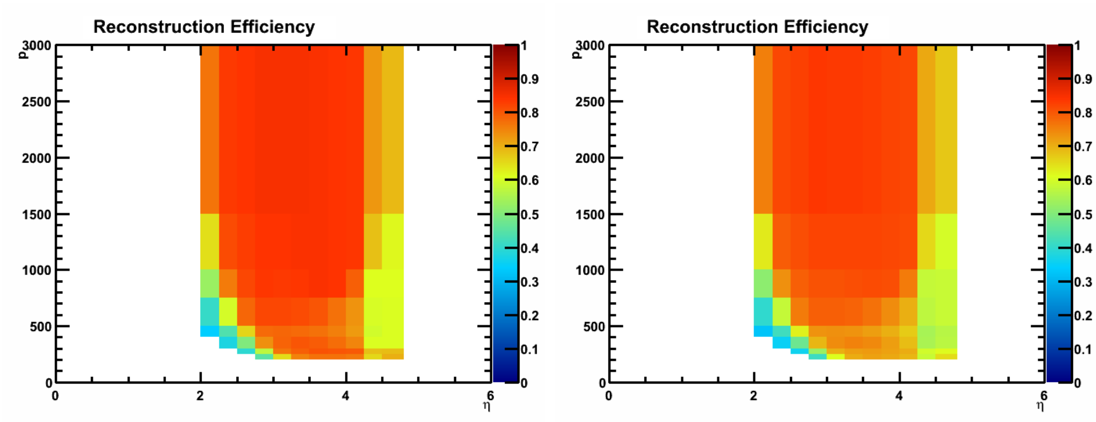

(A) probability of reconstructing a prompt particle as a track anywhere in η and p_{T}

(B) probability of reconstructing a prompt particle as a track in the same η and p_{T} bin

FIGURE 5.10: Prompt particle reconstruction efficiency for particles with $2.0 < \eta < 4.8$ & $p_{\mathrm{T}} >= 200$ MeV & $|p| >= 2000$ MeV calculated from MC generated data.

By combining the efficiency together with the purity the average ratio of the number of reconstructed tracks to the number of true prompt particles can be calculated, see equation 5.3. This correction factor is then applied on an event by event basis to give the corrected particle density contributions, figure 5.11. A comparison between the corrected charged particle densities of measured and MC data can be seen in figure 5.12 and a cross-check of the method using MC data is shown in figure 5.13.

$$\frac{n_{\mathrm{reco}}}{n_{\mathrm{true}}}(\eta, p_T, n_{VELO}, n_t) = p \cdot \epsilon^{-1} \tag{5.3}$$

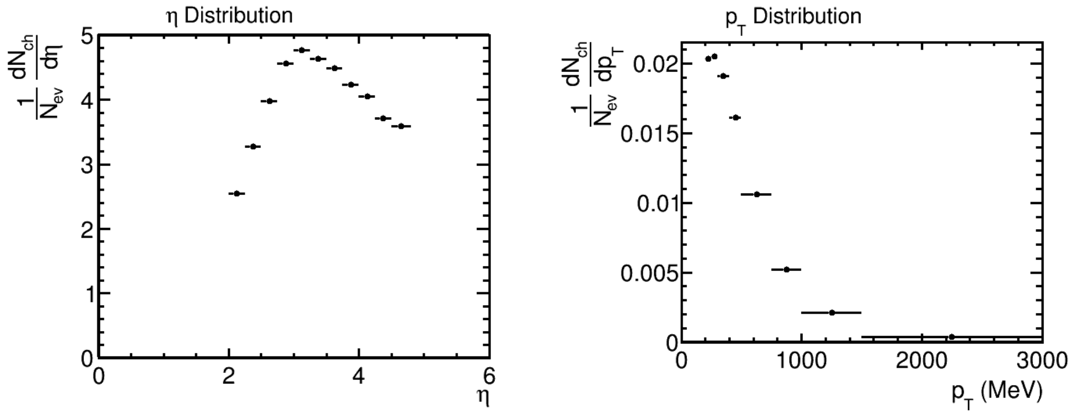

(A) η (B) p_T

FIGURE 5.11: Unfolded track distributions for tracks with $2.0 < \eta < 4.8$ & $p_{\mathrm{T}} >= 200$ MeV & $|p| >= 2000$ MeV & $\mathrm{DOCA}_{\mathrm{beamline}} < 2$ mm & $\Delta z/\sigma_z < 3$ where $\mathrm{DOCA}_{\mathrm{beamline}}$ is the minimum distance between the track and the beamline, Δz is the distance in z between the nominal interaction region and the track's closest position to the beamline and σ_z corresponds to the width of the nominal interaction region.

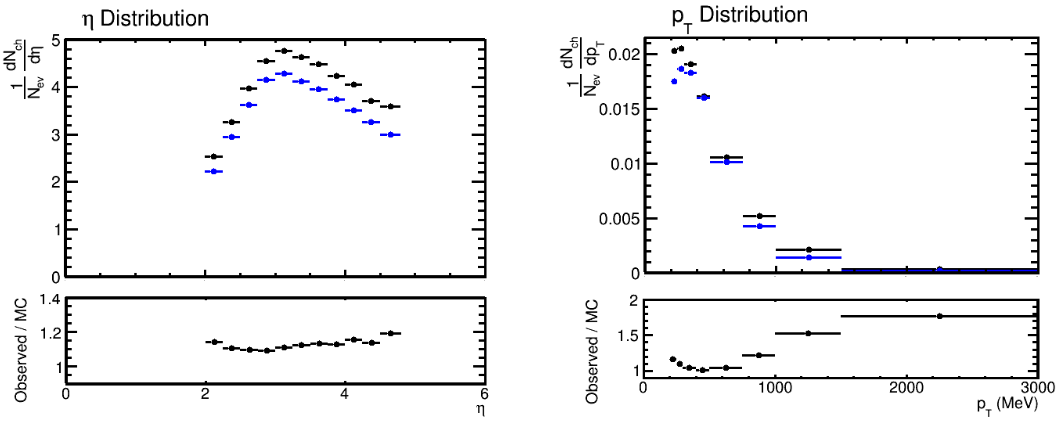

(A) η (B) p_T

FIGURE 5.12: Comparison between measured data (black) and MC generated data (blue) of the unfolded track distributions for tracks with $2.0 < \eta < 4.8$ & $p_{\mathrm{T}} >= 200$ MeV & $|p| >= 2000$ MeV & $\mathrm{DOCA}_{\mathrm{beamline}} < 2$ mm & $\Delta z/\sigma_z < 3$ where $\mathrm{DOCA}_{\mathrm{beamline}}$ is the minimum distance between the track and the beamline, Δz is the distance in z between the nominal interaction region and the track's closest position to the beamline and σ_z corresponds to the width of the nominal interaction region. The lower plot shows the ratio between measured data and MC generated data.

5.5.3 Pile-up correction

The Pile-Up is the number of proton interactions corresponding to a bunch crossing instance. A bunch crossing consisting of multiple proton interactions will associate all interactions to the same event. In order to calculate the charged particle density associated to a single proton-proton interaction a correction is applied to remove the

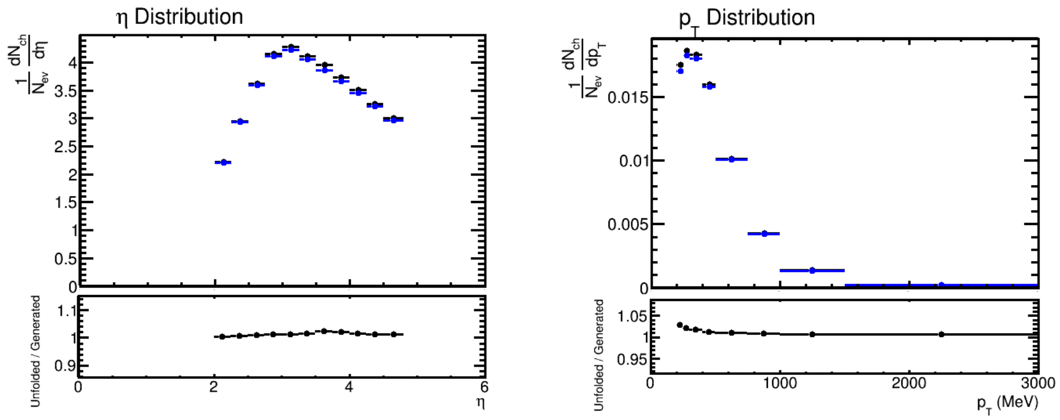

(A) η (B) p_T

FIGURE 5.13: Comparison of the unfolded track distributions to the MC particle distributions for particles with $2.0 < \eta < 4.8$ & $p_{\mathrm{T}} >= 200$ MeV & $|p| >= 2000$ MeV. The correction is applied using tracks with $2.0 < \eta < 4.8$ & $p_{\mathrm{T}} >= 200$ MeV & $|p| >= 2000$ MeV & $\mathrm{DOCA_{beamline}} < 2$ mm & $\Delta z/\sigma_z < 3$ where $\mathrm{DOCA_{beamline}}$ is the minimum distance between the track and the beamline, Δz is the distance in z between the nominal interaction region and the track's closest position to the beamline and σ_z corresponds to the width of the nominal interaction region. The ratio of the corrected distribution and MC particle distribution are shown in the bottom of the figure. The same MC generated data set is used for both the unfolded track distribution and MC particle distribution.

effects of pile-up. The amount of pile expected in a data sample is related to the number visible proton-proton interactions (n) per bunch crossing, this follows a Poisson distribution given by equation 5.4.

$$P(n;\mu) = \frac{\mu^n e^{-\mu}}{n!} \tag{5.4}$$

where μ is the expected number of visible proton-proton interactions per bunch crossing. The value of μ for a dataset can be calculated by plotting the distribution of the time passed between consecutive events ($g(\Delta t)$) and fitting it to equation 5.5,

$$g(\Delta t) = e^{-\mu \cdot k \cdot f \cdot \Delta t} \tag{5.5}$$

where k is the number of colliding bunches (1 for magnet down data and 2 for magnet up data) and f is the LHC revolution frequency (11.246 kHz for data collected in 2010). Fitting the distribution (see figure 5.14) gives a μ is of 0.0261 for magnet down data and 0.0066 for magnet up data in 2010.

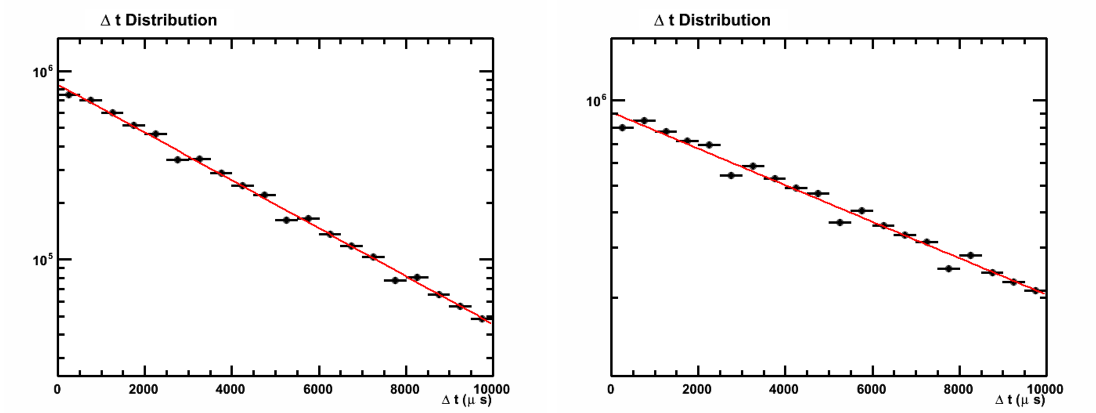

(A) Magnet Down (B) Magnet Up

FIGURE 5.14: Distribution of the time between events with at least one track reconstructed

Introducing a trigger condition that accepts only events with visible interactions gives a probability distribution of observing n interactions ($1 \leq n \leq \infty$) with an expected number of interactions μ_1 described by a renormalised zero suppressed Poisson distribution.

$$P_1(n;\mu_1) = \frac{P(n;\mu)}{1 - P(0;\mu)} \qquad \text{for } 1 \leq n \leq \infty \tag{5.6}$$

The expectation value μ_1 that describes the expected number of visible interactions in triggered events, i.e. pile-up is given by,

$$\mu_1 = \frac{\sum_{n=1}^{\infty} n \cdot P(n;\mu)}{1 - P(0;\mu)} = \frac{\sum_{k=0}^{\infty} n \cdot P(n;\mu)}{1 - e^{-\mu}} = \frac{\mu}{1 - e^{-\mu}} \tag{5.7}$$

For small values of μ the pile-up can be expressed as the following expansion,

$$\mu_1 \approx \frac{\mu}{1 - (1 - \mu + \mu^2/2)} \approx 1 + \frac{\mu}{2} \tag{5.8}$$

To correct the particle density distributions the number of events are renormalised to include events including two proton-proton interactions, this is given by,

$$N_{ev}^{\text{total}} = \mu_1 \cdot N_{\text{ev}} = N_{\text{ev}}(1 + \frac{\mu}{2}) \tag{5.9}$$

This corresponds to a decrease in the charged particle density of 1.3% for magnet down data and 0.33% for magnet up data.

5.5.4 Uncertainties and Results

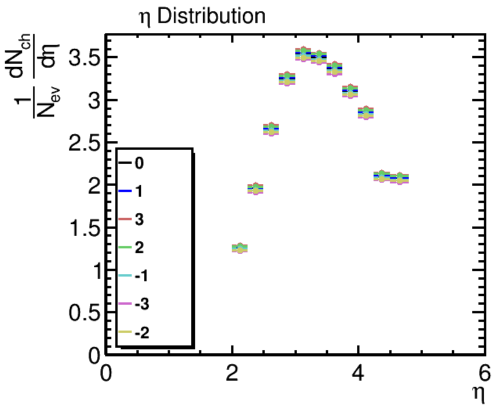

(A) Background corrected charged particle density, η

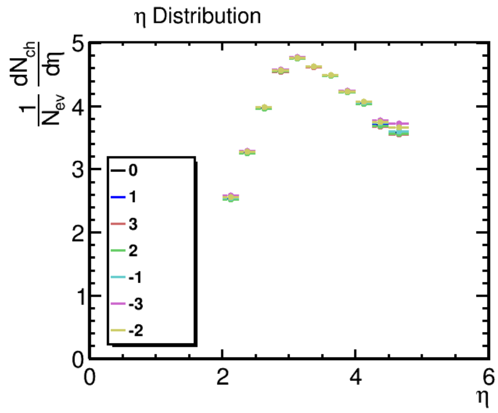

(B) Unfolded charged particle density, η

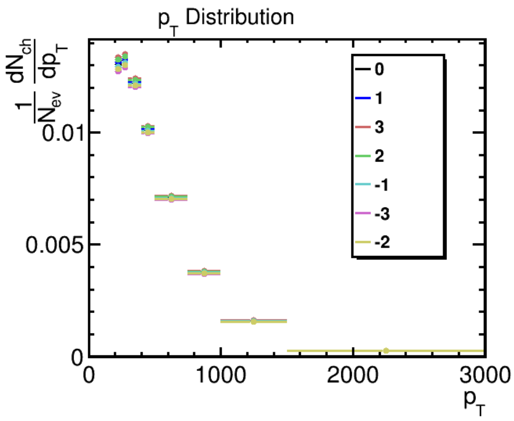

(C) Background charged particle density, p_T

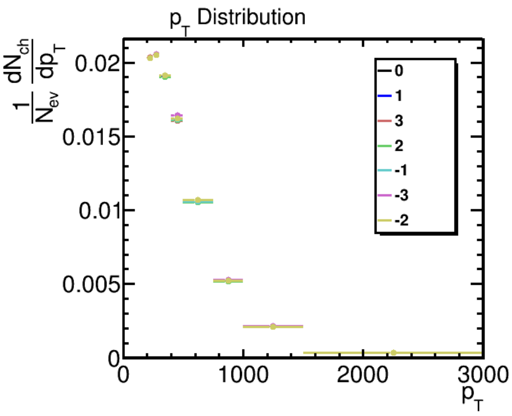

(D) Unfolded charged particle density, p_T

FIGURE 5.15: Uncertainty of the corrected charged particle density in measured data due to statistical errors in the purity and efficiency for tracks with $2.0 < \eta < 4.8$ & p_T >= 200 MeV & $|p|$ >= 2000 MeV & $\mathrm{DOCA}_{\mathrm{beamline}} < 2$ mm & $\Delta z/\sigma_z < 3$ where $\mathrm{DOCA}_{\mathrm{beamline}}$ is the minimum distance between the track and the beamline, Δz is the distance in z between the nominal interaction region and the track's closest position to the beamline and σ_z corresponds to the width of the nominal interaction region.

Since the purity and efficiency distributions are calculated from MC generated data, there is an associated uncertainty due to the statistical error in their distributions. This uncertainty is estimated by applying the correction procedure with the values of the purity and efficiency varied by their standard deviation. The resulting corrected distributions are shown in figure 5.15 for measured data and figure 5.16 for MC data.

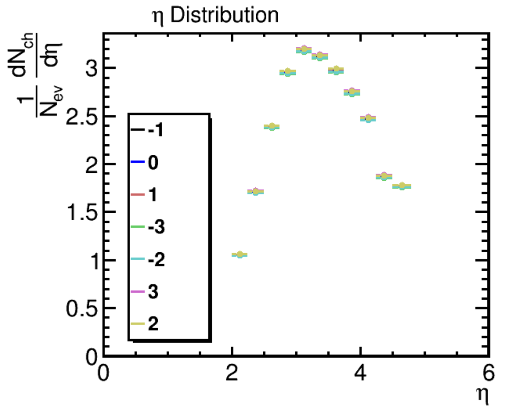

(A) Background corrected charged particle density, η

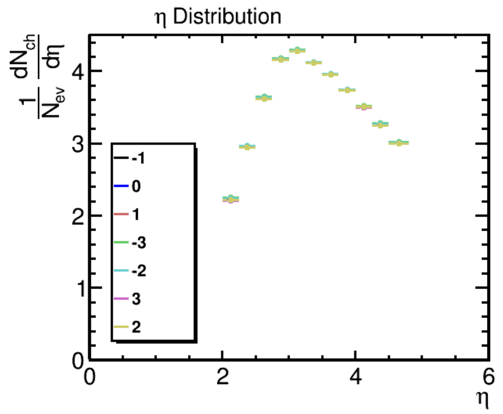

(B) Unfolded charged particle density, η

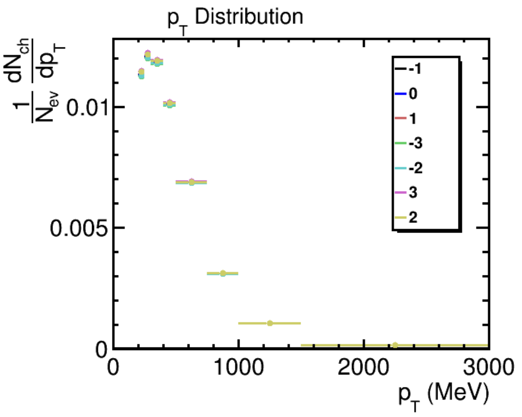

(C) Background charged particle density, p_{T}

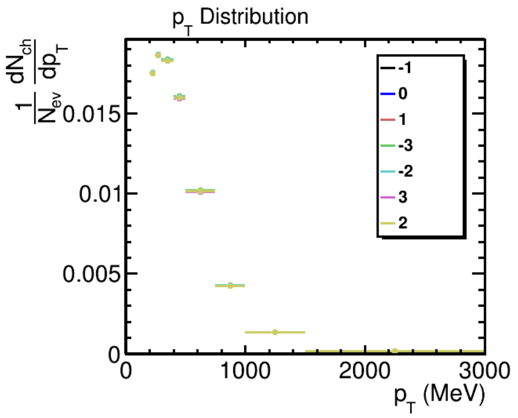

(D) Unfolded charged particle density, p_{T}

FIGURE 5.16: Uncertainty of the corrected charged particle density in MC data due to statistical errors in the purity and efficiency for tracks with $2.0 < \eta < 4.8$ & $p_{\mathrm{T}} >= 200$ MeV & $|p| >= 2000$ MeV & $\mathrm{DOCA_{beamline}} < 2$ mm & $\Delta z/\sigma_z < 3$ where $\mathrm{DOCA_{beamline}}$ is the minimum distance between the track and the beamline, Δz is the distance in z between the nominal interaction region and the track's closest position to the beamline and σ_z corresponds to the width of the nominal interaction region.

The uncertainty in the background correction of the charged particle density is dominated by the ghost correction, this can been seen in figure 5.7. The systematic error on the ghost estimation is estimated by comparing the ghost rates calculated in section 5.5.1 to a data driven method of ghost estimation.

From MC data it can be seen that the dominant source of ghost tracks is from mismatching VELO track segments (see section 3.6.3) to hits or track segments in the T-stations - these hits may be due to other particles or detector noise. The data driven method of estimates these effects using the VELO flip method; this involves taking a reconstructed VELO track segment and flipping its direction in x and y. The flipped

VELO track segment is then used as a seed in the forward track matching reconstruction algorithm that attempts to match the segment to hits or other track segments in the T-stations. Forward tracks reconstructed using the flipped VELO segment as its seed are then classified as ghost tracks.

In order for the track to be reconstructed it must meet several criteria such as a quality of fit (χ^2) cut. In addition to this the track must be a better candidate than other combinations of the VELO track segment seed and T-station hits or track segments. In order to make an accurate estimation of the ghost rate the track candidates from the flipped VELO track segment are compared to the candidates from the original VELO track segment, if the best track candidate is from the flipped VELO track segment then it is kept.

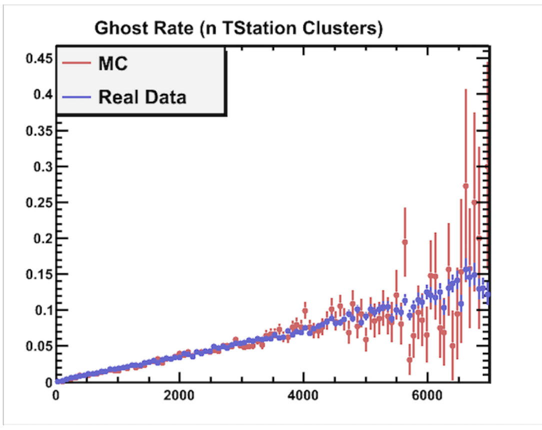

FIGURE 5.17: Ghost rates as a function of T-station hit multiplicity calculated using the data driven VELO flip method. The data points in red correspond to the ghost rate in MC data and the blue data points correspond to measured data. A good agreement is present between MC and measured data.

Due to the nature of the matching algorithm, events with higher activity (expressed by the number of hits in the T-stations) in the detector are expected to have higher ghost rates. The ghost rate is plotted as a function of the T-station multiplicity (figure 5.17). The ghost rate is determined by the ratio of ghost classified tracks to the number of VELO track segments in an event, to translate this to the context of long tracks used in this analysis the ghost rate in long tracks is related to the ghost rate in VELO tracks scaled by the ratio of VELO tracks to long tracks.

$$R_{\text{long}} = R_{\text{VELO}} \cdot \frac{n_{\text{VELO}}}{n_{\text{long}}} \tag{5.10}$$

where R_{long} is the ghost rate in long tracks, R_{VELO} is the ghost rate in VELO tracks, n_{VELO} is the number of velo tracks and n_{long} is the number of long tracks in the event. The overall ghost rate is then calculated from the average of the ghost rate in all events. The comparison between ghost rate estimation using the VELO flip method is shown in figure 5.17; there is good agreement between measured and MC data. A conservative estimate of 2% for the systematic error was made for this analysis, as is the case for similar analyses such as [55].

The final results for the charged particle density are shown in figure 5.18 with the systematics errors shown by the blue shaded boxes. A comparison between the unfolded distribution and charged particle distributions in MC generated events are shown for several event generators in figure 5.19. The results show that the charge density in both η and p_{T} is significantly lower in the PYTHIA 6 and PYTHIA 8 data than seen in the measured data over the entire η and p_{T} range. This is consistent with the measurements made by the other detectors at the LHC discussed earlier in section 5.1. On the other hand the charged particle density seen in data generated using the EPOS data is systematically higher over the η and p_{T} range. These values are closer to the values seen in the measured data (particularly for the charged particle density as a function of p_{T}) but are still not consistent with the measured data. Overall the charged particle density shown in the measured data is not adequately modelled by any the Monte Carlo generators used in this study, but these results will hopefully help to constrain these models and inspire future models describing proton-proton interactions at the energies present at the LHC.

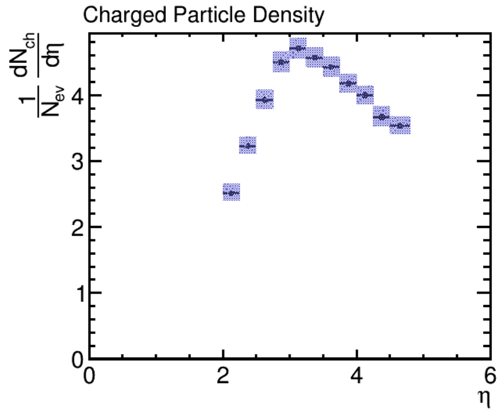

(A) η

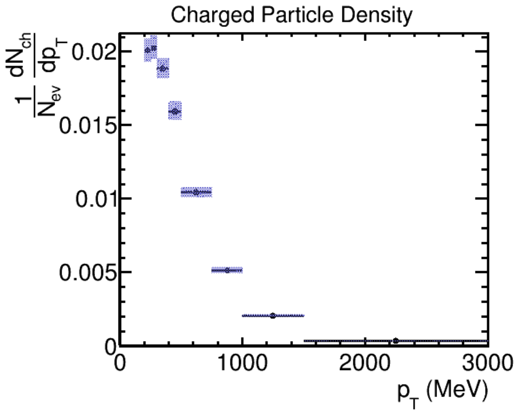

(B) p_{T}

FIGURE 5.18: Corrected charged particle densities, systematic errors are shown by the shaded blue areas for particles with $2.0 < \eta < 4.8$ & $p_{\mathrm{T}} >= 200$ MeV & $|p| >= 2000$ MeV corrected using tracks with $2.0 < \eta < 4.8$ & $p_{\mathrm{T}} >= 200$ MeV & $|p| >= 2000$ MeV & $\mathrm{DOCA_{beamline}} < 2$ mm & $\Delta z/\sigma_z < 3$ where $\mathrm{DOCA_{beamline}}$ is the minimum distance between the track and the beamline, Δz is the distance in z between the nominal interaction region and the track's closest position to the beamline and σ_z corresponds to the width of the nominal interaction region.

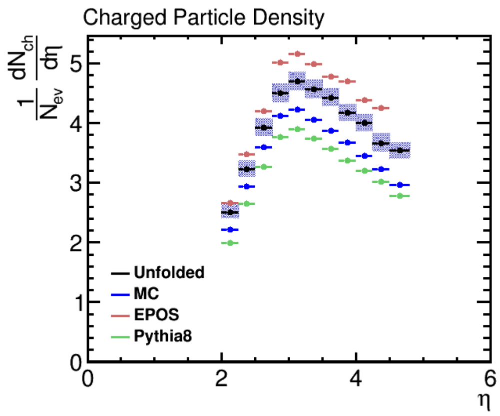

(A) η

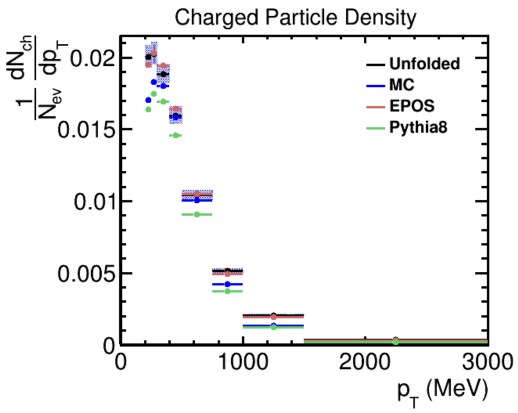

(B) p_{T}

FIGURE 5.19: Comparison of corrected charged particle densities between measured data and several MC generators for particles with $2.0 < \eta < 4.8$ & $p_{\mathrm{T}} >= 200$ MeV & $|p| >= 2000$ MeV. The corrected distribution was corrected using tracks with $2.0 < \eta < 4.8$ & $p_{\mathrm{T}} >= 200$ MeV & $|p| >= 2000$ MeV & $\mathrm{DOCA_{beamline}} < 2$ mm & $\Delta z/\sigma_z < 3$ where $\mathrm{DOCA_{beamline}}$ is the minimum distance between the track and the beamline, Δz is the distance in z between the nominal interaction region and the track's closest position to the beamline and σ_z corresponds to the width of the nominal interaction region.

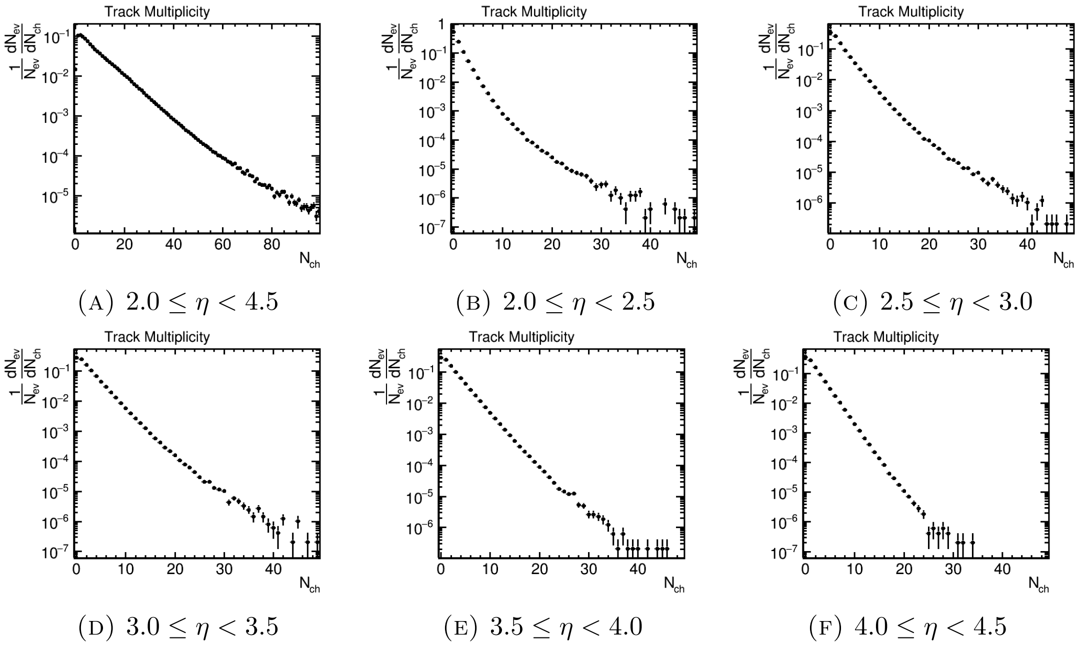

(A) $2.0 \leq \eta < 4.5$ (B) $2.0 \leq \eta < 2.5$ (C) $2.5 \leq \eta < 3.0$

(D) $3.0 \leq \eta < 3.5$ (E) $3.5 \leq \eta < 4.0$ (F) $4.0 \leq \eta < 4.5$

FIGURE 5.20: Reconstructed track multiplicity of measured data for tracks with $2.0 \leq \eta < 4.8$ & $p_{\mathrm{T}} \geq 200$ MeV & $|p| \geq 2000$ MeV & $\mathrm{DOCA}_{\mathrm{beamline}} < 2$ mm & $\Delta z/\sigma_z < 3$ where $\mathrm{DOCA}_{\mathrm{beamline}}$ is the minimum distance between the track and the beamline, Δz is the distance in z between the nominal interaction region and the track's closest position to the beamline and σ_z corresponds to the width of the nominal interaction region. Only events with at least one of track matching this criteria were accepted.

5.6 Charged Particle Event Multiplicity

The event multiplicity distribution describes the number of tracks or charged particles produced per proton-proton interaction. The process of particle production in high energy collisions is very sensitive to phenomenological models used by MC event generators. As with the case of the charged particle densities, a series of corrections are applied to the measured track distributions to correct for detector effects such as background contributions, reconstruction efficiencies and pile-up. The charged particle densities the distributions were plotted as a function of the continuous quantities, pseudorapidity and transverse momentum. The event multiplicity distribution is plotted as a function of the discrete quantity, N_{ch}, the number of charged particles or tracks in the event. In order to correct the distribution, different methods of applying the corrections are employed, these are discussed in the following sections.

The uncorrected track multiplicities are shown in figure 5.20. A comparison between measured and MC data is shown in figure 5.21; these data shows a systematic increase

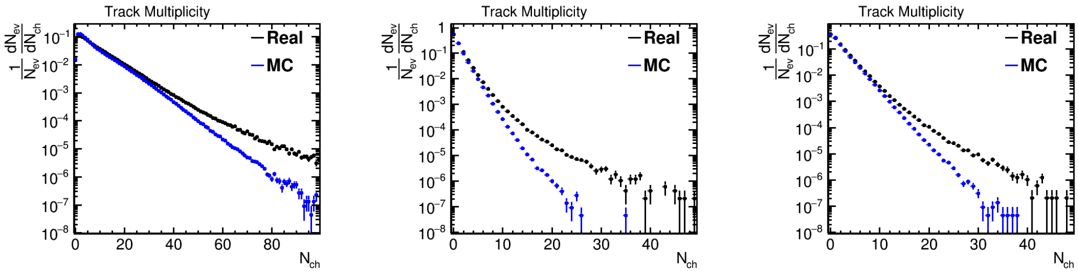

(A) $2.0 \leq \eta < 4.5$ (B) $2.0 \leq \eta < 2.5$ (C) $2.5 \leq \eta < 3.0$

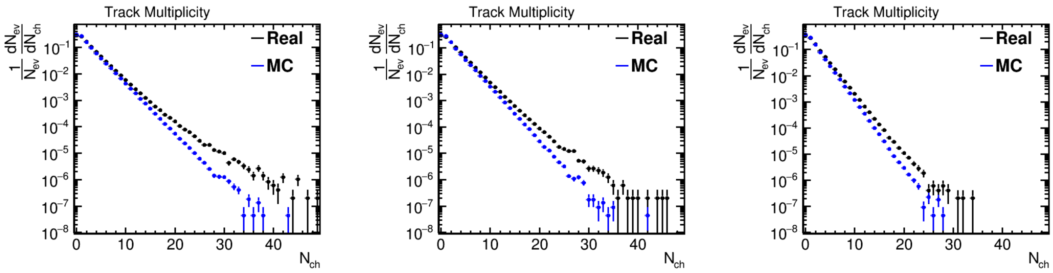

(D) $3.0 \leq \eta < 3.5$ (E) $3.5 \leq \eta < 4.0$ (F) $4.0 \leq \eta < 4.5$

FIGURE 5.21: Comparison of reconstructed track multiplicities in measured (black) and MC simulated (blue) data for tracks with $p_T \geq 200$ MeV & $|p| \geq 2000$ MeV & $\mathrm{DOCA_{beamline}} < 2$ mm & $\Delta z/\sigma_z < 3$ where $\mathrm{DOCA_{beamline}}$ is the minimum distance between the track and the beamline, Δz is the distance in z between the nominal interaction region and the track's closest position to the beamline and σ_z corresponds to the width of the nominal interaction region. Only events with at least one of track matching this criteria were accepted.

in the track multiplicity in measured data, this is partly due to pile-up (which is not included in the MC simulated data) and the physics of the MC generator. Lastly a comparison between the uncorrected track multiplicity and the true particle multiplicity in MC data is shown in figure 5.22; this shows that the detector response varies significantly over the pseudorapidity range of the experiment with efficiency effects being more predominant at the boundaries, $2.0 \leq \eta \leq 2.5$ and $4.0 \leq \eta \leq 4.5$, and background effects being more predominant in the middle region $3.0 \leq \eta \leq 4.0$.

5.6.1 Background Correction

For the charged particle multiplicity distributions the background is modelled by a Poisson distribution,

$$f(k;\lambda) = \frac{\lambda^k e^{-\lambda}}{k!}$$

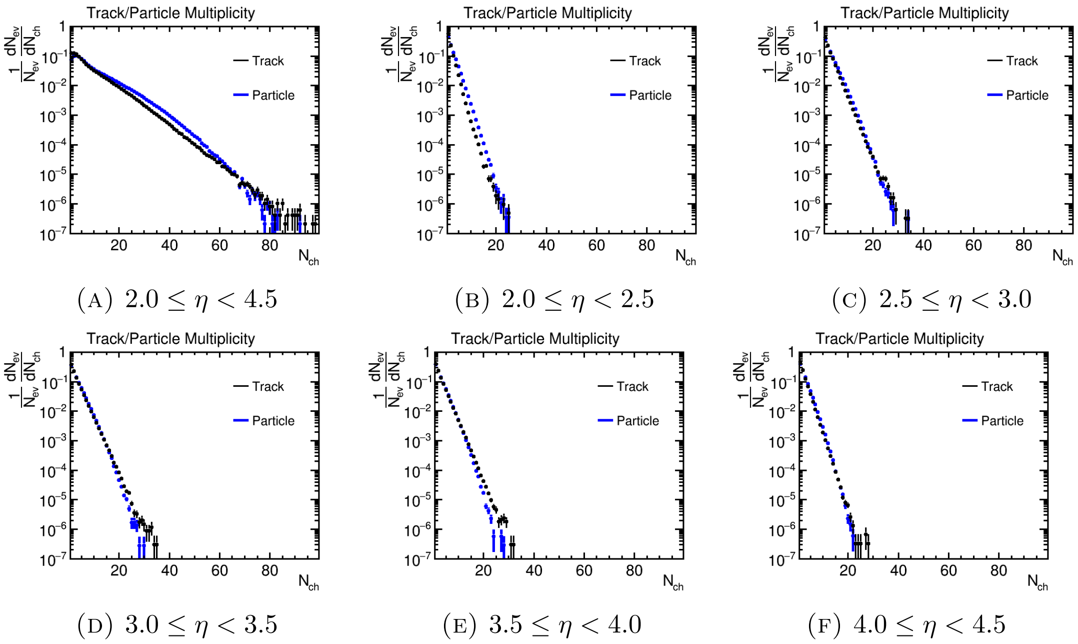

FIGURE 5.22: Comparison between reconstructed track multiplicities and generator charged particle multiplicities in MC simulated data for tracks with $p_{\mathrm{T}} \geq 200$ MeV & $|p| \geq 2000$ MeV & $\mathrm{DOCA}_{\mathrm{beamline}} < 2$ mm & $\Delta z/\sigma_z < 3$ where $\mathrm{DOCA}_{\mathrm{beamline}}$ is the minimum distance between the track and the beamline, Δz is the distance in z between the nominal interaction region and the track's closest position to the beamline and σ_z corresponds to the width of the nominal interaction region. Only events with at least one of track matching this criteria were accepted. The generator particle selection selects charged stable particles in the same kinematic region as for the track selection and with a prompt lifetime cut on its ancestors. Only events with at least one of track matching this criteria were accepted.

where k corresponds to the number of background tracks in an event and λ corresponds to the expected number of background tracks. The expected number of background tracks is calculated by summing the background rates for all tracks in the event. These background rates for the tracks are calculated from the purity calculated in section 5.5.1 and shown in figure 5.6.

$$\lambda = \sum_{i=0}^{N} 1 - p_i(\eta, p_{\mathrm{T}}, n_{VELO}, n_{\mathrm{t}}) \tag{5.11}$$

where N is the total number of selected tracks in the event and p is the purity corresponding to the η, p_{T}, n_{VELO} and n_{t} bin associated to the track. To apply the correction to the event multiplicity all allowed values for the number of background tracks (k) are considered and weighted by the corresponding probability. An event with N tracks may then be considered as the sum of events with $k \in \{0, 1, ..., N\}$ background tracks weighted by the corresponding probability. Since the Poisson distribution is limited by the allowed values of k ($0 \leq k \leq N$), the Poisson distribution requires and additional normalisation factor I^{-1} where I is given by,

$$I = \sum_{k=0}^{N} f(k; \lambda) \tag{5.12}$$

The results of the background correction applied to measured data are shown in figure 5.23 and comparisons to the background correction applied to MC data is shown in figure 5.24.

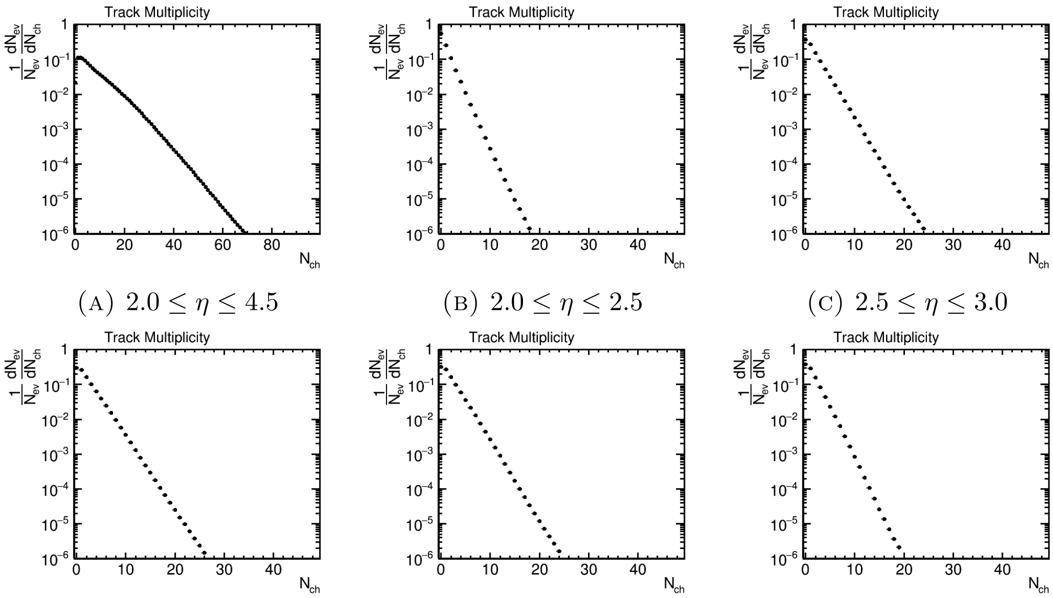

(A) $2.0 \leq \eta \leq 4.5$ (B) $2.0 \leq \eta \leq 2.5$ (C) $2.5 \leq \eta \leq 3.0$

(D) $3.0 \leq \eta \leq 3.5$ (E) $3.5 \leq \eta \leq 4.0$ (F) $4.0 \leq \eta \leq 4.5$

FIGURE 5.23: Background corrected track multiplicities in measured data for tracks with $2.0 \leq \eta < 4.8$ & $p_{\mathrm{T}} \geq 200$ MeV & $|p| \geq 2000$ MeV & $\mathrm{DOCA}_{\mathrm{beamline}} < 2$ mm & $\Delta z/\sigma_z < 3$ where $\mathrm{DOCA}_{\mathrm{beamline}}$ is the minimum distance between the track and the beamline, Δz is the distance in z between the nominal interaction region and the track's closest position to the beamline and σ_z corresponds to the width of the nominal interaction region. Only events with at least one of track matching this criteria were accepted.

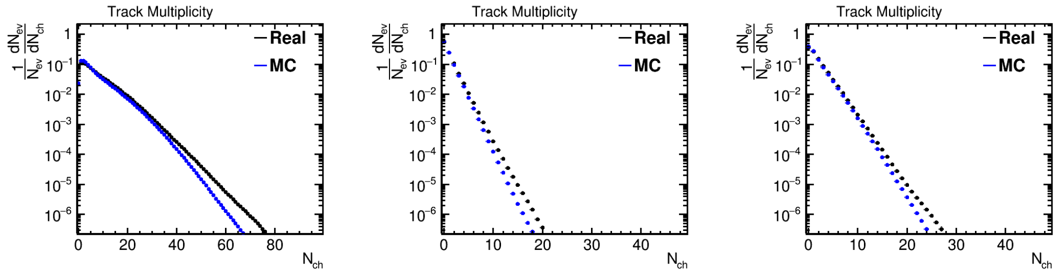

(A) $2.0 \leq \eta \leq 4.5$ (B) $2.0 \leq \eta \leq 2.5$ (C) $2.5 \leq \eta \leq 3.0$

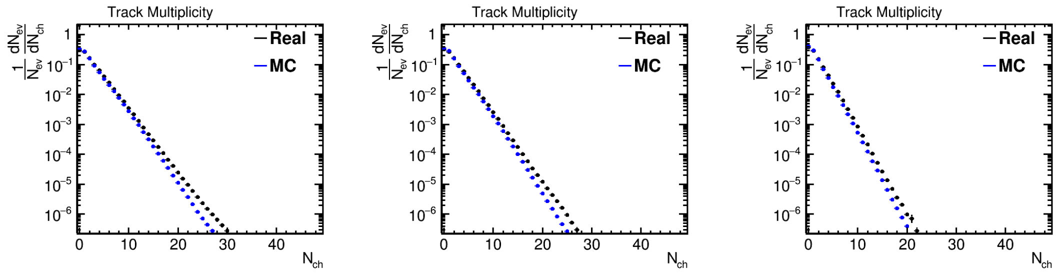

(D) $3.0 \leq \eta \leq 3.5$ (E) $3.5 \leq \eta \leq 4.0$ (F) $4.0 \leq \eta \leq 4.5$

FIGURE 5.24: Comparison of background corrected track multiplicities from measured (black) and MC (blue) data for tracks with $2.0 \leq \eta < 4.8$ & $p_{\mathrm{T}} \geq 200$ MeV & $|p| \geq 2000$ MeV & $\mathrm{DOCA_{beamline}} < 2$ mm & $\Delta z/\sigma_z < 3$ where $\mathrm{DOCA_{beamline}}$ is the minimum distance between the track and the beamline, Δz is the distance in z between the nominal interaction region and the track's closest position to the beamline and σ_z corresponds to the width of the nominal interaction region. Only events with at least one of track matching this criteria were accepted.

5.6.2 Efficiency Correction

5.6.2.1 The Response Matrix

The efficiency correction for the multiplicity distribution is modelled by the response matrix R. This characterises the effect of the detector response on the charged particle multiplicity distribution, it is a two dimensional matrix with dimensions of n by m where each element R_{ij}, corresponds to the probability to reconstruct i tracks given that j prompt particles are present in the event (constraining the values along the columns so that their sum is normalised to one). The relationship between the track multiplicity a, true multiplicity b and response matrix R can be then expressed as a matrix equation,

$$a = R \cdot b \tag{5.13}$$

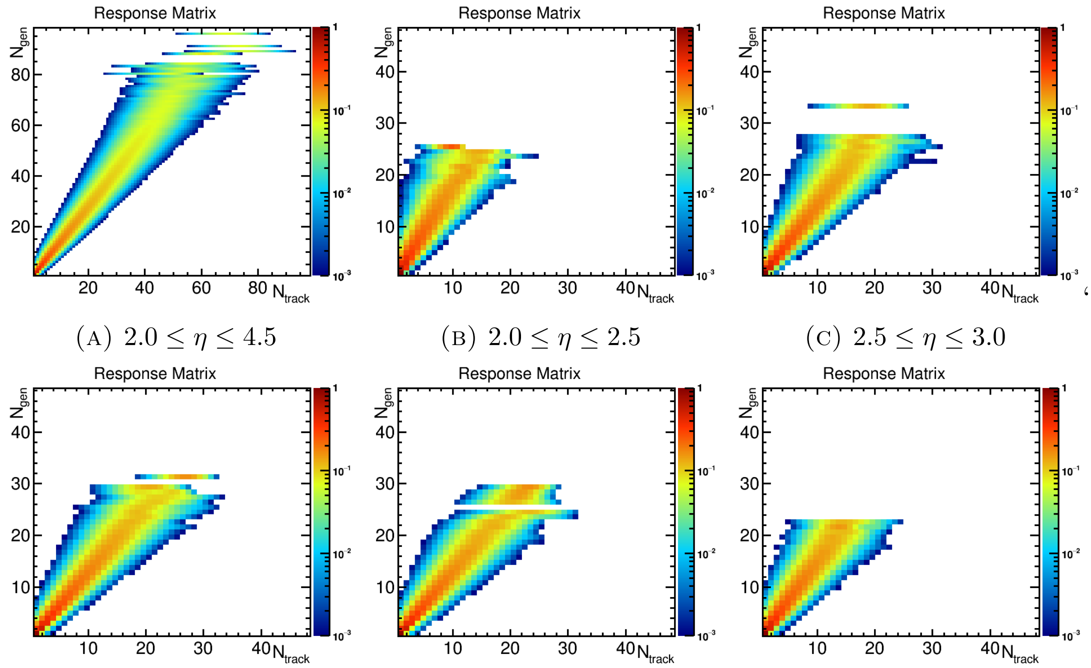

(A) $2.0 \leq \eta \leq 4.5$ (B) $2.0 \leq \eta \leq 2.5$ (C) $2.5 \leq \eta \leq 3.0$

(D) $3.0 \leq \eta \leq 3.5$ (E) $3.5 \leq \eta \leq 4.0$ (F) $4.0 \leq \eta \leq 4.5$

FIGURE 5.25: Response matrices for tracks with $2.0 \leq \eta < 4.8$ & $p_{\mathrm{T}} \geq 200$ MeV & $|p| \geq 2000$ MeV & $\mathrm{DOCA}_{\mathrm{beamline}} < 2$ mm & $\Delta z/\sigma_z < 3$ where $\mathrm{DOCA}_{\mathrm{beamline}}$ is the minimum distance between the track and the beamline, Δz is the distance in z between the nominal interaction region and the track's closest position to the beamline and σ_z corresponds to the width of the nominal interaction region. Only events with at least one of track matching this criteria were accepted.The generator particle selection selects charged stable particles in the same kinematic region as for the track selection and with a prompt lifetime cut on its ancestors.

where a and b are column matrices describing the track and particle multiplicities such that a_i is the number of events with i reconstructed tracks and b_j is the number of events with j corresponding true particles. This can be interpreted as a set of linear equations,

$$a_i = \sum_{j=0}^{m} R_{ij} \cdot b_j \qquad i \in \{0, 1, ..., n\} \tag{5.14}$$

The response matrix is determined using truth information from Monte Carlo simulated events. Each event is first subject to the background correction procedure discussed in section 5.6.1 so that the response matrix corresponds only to efficiency effects. As in section 5.6.1 the number of background tracks is varied between its allowed range ($0 \leq k \leq N$) and the number of signal tracks, $n_{\mathrm{signal}} = N - k$, is then plotted against the number of prompt particles present in the event, then weighted by the corresponding probability of observing n_{signal}. Due to insufficient statistics at the high multiplicity

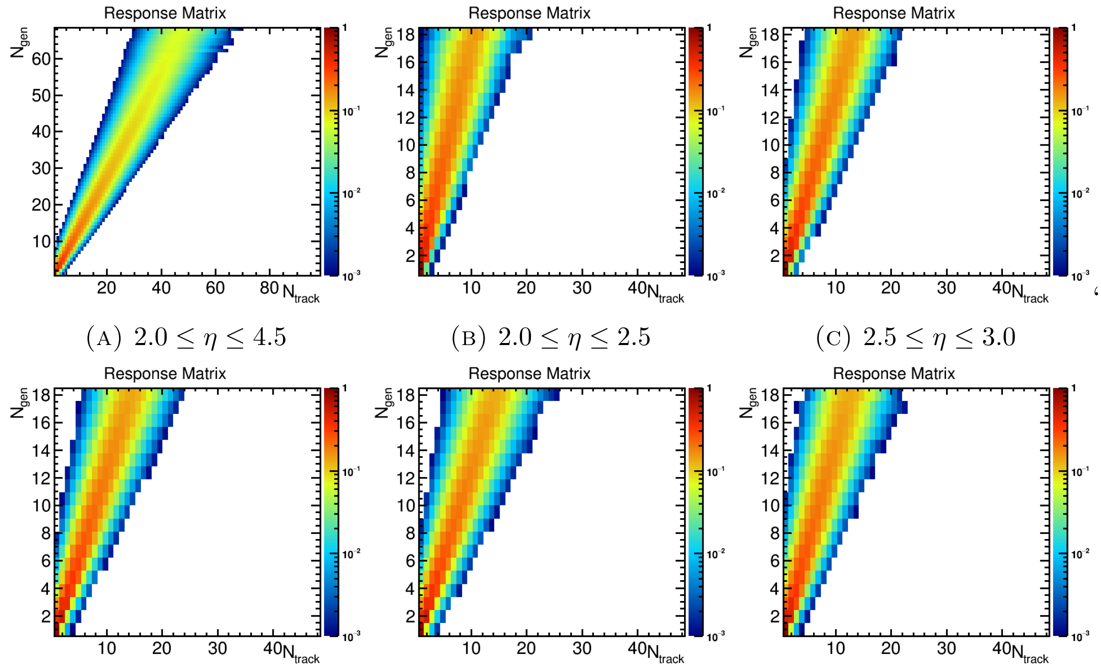

(A) $2.0 \leq \eta \leq 4.5$ (B) $2.0 \leq \eta \leq 2.5$ (C) $2.5 \leq \eta \leq 3.0$

(D) $3.0 \leq \eta \leq 3.5$ (E) $3.5 \leq \eta \leq 4.0$ (F) $4.0 \leq \eta \leq 4.5$

FIGURE 5.26: Truncated response matrices s with $2.0 \leq \eta < 4.8$ & $p_{\mathrm{T}} \geq 200$ MeV & $|p| \geq 2000$ MeV & $\mathrm{DOCA}_{\mathrm{beamline}} < 2$ mm & $\Delta z/\sigma_z < 3$ where $\mathrm{DOCA}_{\mathrm{beamline}}$ is the minimum distance between the track and the beamline, Δz is the distance in z between the nominal interaction region and the track's closest position to the beamline and σ_z corresponds to the width of the nominal interaction region. Only events with at least one of track matching this criteria were accepted. The generator particle selection selects charged stable particles in the same kinematic region as for the track selection and with a prompt lifetime cut on its ancestors. The response matrices are truncated to exclude particle multiplicity regions where there is low statistics.

regions in the MC data (see figure 5.25 the response matrices are truncated to remove elements with low statistical significance, the response matrices calculated for the efficiency correction are shown in figure 5.26.

5.6.2.2 True Multiplicity Parameterisation

Starting from equation 5.13 a heuristic approach to calculating the true particle multiplicity can be employed. By making a educated guess at the shape of the true distribution a corresponding expected multiplicity can be calculated by applying the response matrix. Comparing the observed multiplicity to the expected multiplicity gives a quantifiable measurement of the accuracy of the guess. To achieve this in a more systematic way, a parameterisation of the true distribution (b') can be made for which a corresponding response (or smearing) functions (a') exists. By fitting the response function to the observed multiplicity the associated parameters can be propagated back in terms of the parameterisation of the true multiplicity distribution to give a corrected multiplicity distribution. The response function and corresponding χ^2 minimisation function that were used are,

$$a'(p_0, p_1, ..., p_n) = R \cdot b'(p_0, p_1, ..., p_n) \tag{5.15}$$

$$\chi^2(p_0, p_1, ..., p_n) = \sum_{N_{\mathrm{ch}}}^{N_{\mathrm{max}}} \sqrt{a(N_{\mathrm{ch}})^2 - a'(N_{\mathrm{ch}})^2} \tag{5.16}$$

Where $p_0, p_1, ..., p_n$ corresponds to the parameters used to parameterise the response function and hence true multiplicity, N_{max} is the maximum number of reconstructed tracks (N_{ch}), $a(N_{\mathrm{ch}})$ is the number of events with N_{ch} tracks and $a'(N_{\mathrm{ch}})$ is the number of events with N_{ch} reconstructed tracks predicted by the response function.

The true multiplicity distribution is parameterised by several parameterisations (listed below) inspired from similar multiplicity analyses [55]. These parameterisations consist of several parameters such that the parameterisations are extremely flexible and robust. This enables the parameterisations to model a range of possible true distributions, minimising the bias associated to modelling an unknown distribution. The initial values of the parameters in each parameterisation are initialised by fitting MC generated data with each parameterisations, the fits are shown in figure 5.27 and the parameters are shown in table 5.2.

- $f_A(x) = 10^{-9} e^{p_0 + p_1 x} x^2 + 10^{-9} e^{p_2 + p_3 x} x^2 + p_4 e^{-\frac{1}{2}(\frac{x - p_5}{p_6})^2}$
- $f_B(x) = e^{p_0 + p_1 x}(x+1)^3 + e^{p_2 + p_3 x} x^2 + e^{p_4 + p_5 x} x^2$
- $f_C(x) = p_2 NB(x, p_0, p_1) + p_5 NB(x, p_3, p_4) + (1 - p_2 - p_5) NB(x, p_6, p_7)$
- $f_D(x) = e^{p_0 + p_1 x} x^{p_2} + e^{p_3 + p_4 x} x^{p_5} + e^{p_6 + p_7 x} x^{p_8}$

where NB is a negative binomial distribution given by,

$$NB(x, p_0, p_1) = \frac{(x + p_1 - 1)!}{x!(p_1 - 1)!} p_0^{p_1} (1 - p_0)^x \tag{5.17}$$

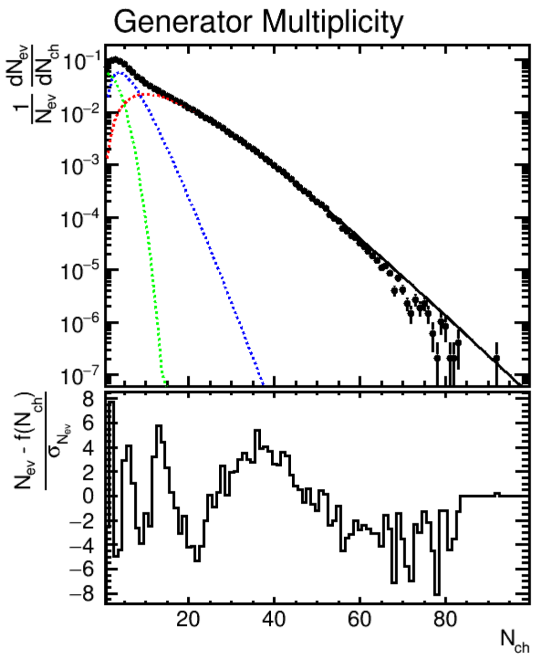

(A) Parameterisation A

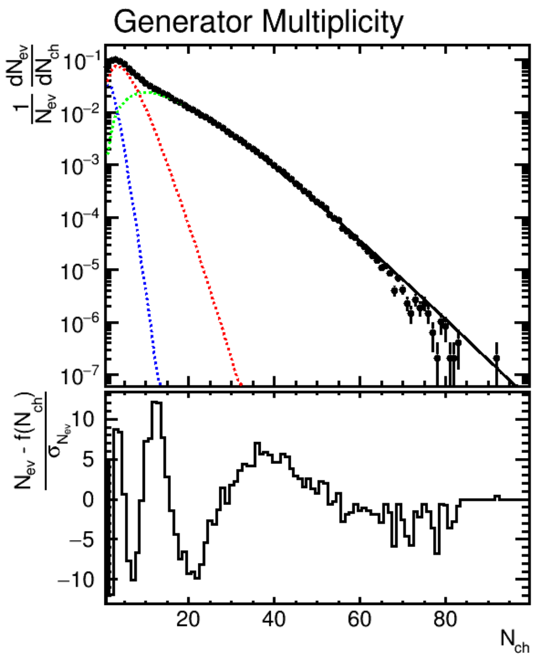

(B) Parameterisation B

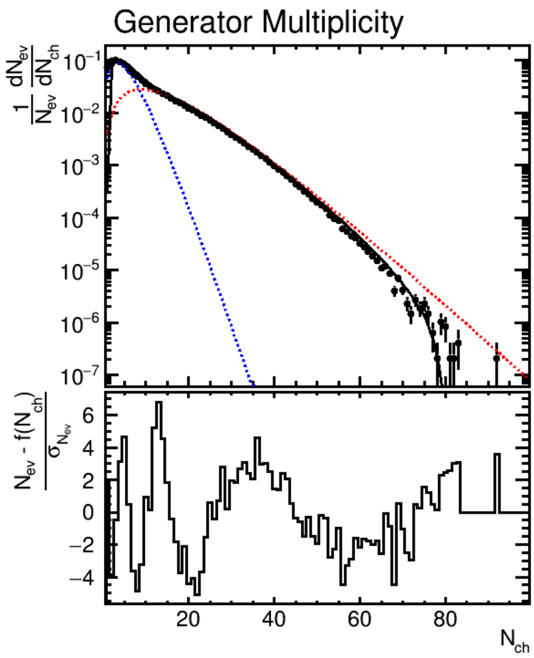

(C) Parameterisation C

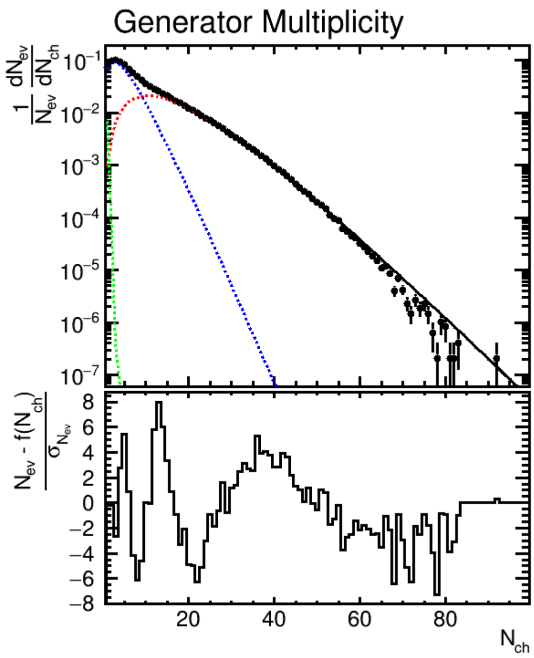

(D) Parameterisation D

FIGURE 5.27: Parameterisation fits to MC data for $2.0 \leq \eta \leq 4.5$. The solid black line corresponds to the total fit and the coloured dotted lines correspond to the components of the total fit

TABLE 5.2: True multiplicity parameterisations fit to generated prompt particle distributions

(A) Parameterisation A

p0	$14.2954 \pm 4.99 \times 10^{-3}$
p1	$-0.1984 \pm 1.78 \times 10^{-4}$
p2	$17.2719 \pm 2.86 \times 10^{-2}$
p3	$-0.5436 \pm 3.27 \times 10^{-3}$
p4	$0.055263 \pm 4.12 \times 10^{-4}$
p5	$0.766571 \pm 6.12 \times 10^{-2}$
p6	$2.54936 \pm 2.19 \times 10^{-2}$
χ^2/n_{dof}	11.87

(B) Parameterisation B

p0	$4.61827 \pm 8.50 \times 10^{-3}$
p1	$-0.7031 \pm 1.41 \times 10^{-3}$
p2	$-1.87528 \pm 7.51 \times 10^{-3}$
p3	$-1.52653 \pm 1.03 \times 10^{-2}$
p4	$-6.32881 \pm 3.73 \times 10^{-3}$
p5	$-0.20164 \pm 1.57 \times 10^{-4}$
χ^2/n_{dof}	26.66

(C) Parameterisation C

p0	$0.168866 \pm 8.17355 \times 10^{-4}$
p1	$2.74981 \pm 2.73212 \times 10^{-2}$
p2	$0.525603 \pm 4.50851 \times 10^{-3}$
p3	$0.452843 \pm 4.71820 \times 10^{-3}$
p4	$3.24562 \pm 5.88466 \times 10^{-2}$
p5	$0.589735 \pm 8.50050 \times 10^{-3}$
p6	$0.0729007 \pm 2.36719 \times 10^{-3}$
p7	$0.329029 \pm 2.47769 \times 10^{-2}$
χ^2/n_{dof}	7.62

(D) Parameterisation D

p0	$-6.76070 \pm 6.34208 \times 10^{-2}$
p1	$-0.203303 \pm 8.89120 \times 10^{-4}$
p2	$2.14251 \pm 2.66230 \times 10^{-2}$
p3	$-224242 \pm 3.11861 \times 10^{-3}$
p4	$-0.463025 \pm 3.63005 \times 10^{-3}$
p5	$1.15883 \pm 1.02232 \times 10^{-2}$
p6	$-0.0251832 \pm 5.60194 \times 10^{-1}$
p7	$-4.98538 \pm 1.77480 \times 10^{-1}$
p8	$0.0119719 \pm 4.03135 \times 10^{-2}$
χ^2/n_{dof}	11.71

The response functions for the background corrected multiplicities in figure 5.23 and parameterisations in figure 5.27 are shown in figure 5.28 for measured data. The corresponding unfolded multiplicities are shown figure 5.29.

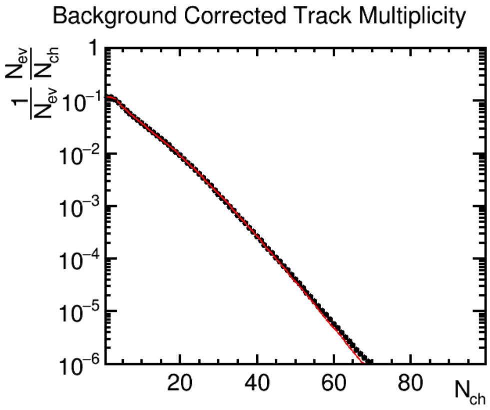

(A) Parameterisation A

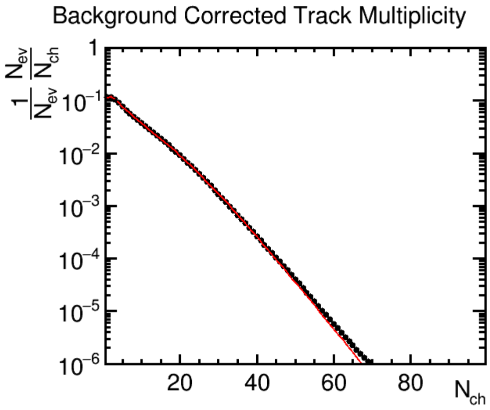

(B) Parameterisation B

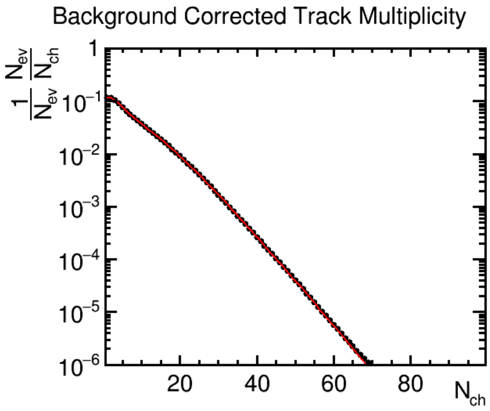

(C) Parameterisation C

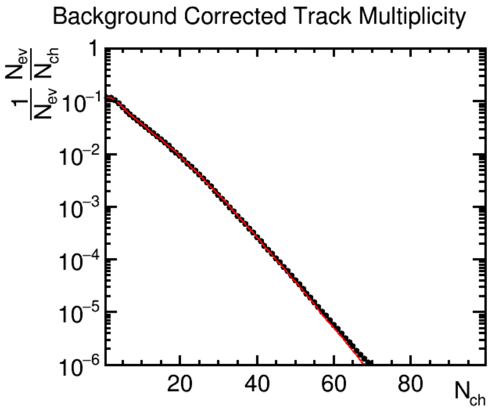

(D) Parameterisation D

FIGURE 5.28: The response function fitted for the background corrected track multiplicity in $2.0 \leq \eta \leq 4.5$ seen in Measured data.

TABLE 5.3: Response function parameters

(A) Parameterisation A

p0	$14.1220 \pm 4.50606 \times 10^{-3}$
p1	$-0.184706e \pm 1.17128 \times 10^{-4}$
p2	$16.2471 \pm 2.78928 \times 10^{-2}$
p3	$-0.411813 \pm 2.69004 \times 10^{-3}$
p4	$0.0537215 \pm 3.62658 \times 10^{-4}$
p5	$1.81841 \pm 2.35143 \times 10^{-2}$
p6	$2.59423 \pm 2.61233 \times 10^{-2}$
χ^2/n_{dof}	12.12

(B) Parameterisation B

p0	$-5.89170 \pm 1.52004 \times 10^{-2}$
p1	$-0.530718 \pm 1.67559 \times 10^{-3}$
p2	$-2.17499 \pm 5.20221 \times 10^{-3}$
p3	$-1.04831 \pm 4.87827 \times 10^{-3}$
p4	$-6.52691 \pm 2.78654 \times 10^{-3}$
p5	$-0.186539 \pm 8.26762 \times 10^{-5}$
χ^2/n_{dof}	26.18

(C) Parameterisation C

p0	$0.151154 \pm 6.18266 \times 10^{-4}$
p1	$2.06655 \pm 4.68535 \times 10^{-2}$
p2	$0.954913 \pm 5.60568 \times 10^{-2}$
p3	$0.330164 \pm 1.38889 \times 10^{-3}$
p4	$1.93727 \pm 9.86289 \times 10^{-3}$
p5	$1.00000 \pm 6.96524 \times 10^{-3}$
p6	$0.184204 \pm 4.62492 \times 10^{-3}$
p7	$1.15272 \pm 1.16887 \times 10^{-2}$
χ^2/n_{dof}	3.72

(D) Parameterisation D

p0	$-6.76495 \pm 8.60131 \times 10^{-3}$
p1	$-0.203354 \pm 2.04042 \times 10^{-4}$
p2	$2.14422 \pm 3.62350 \times 10^{-3}$
p3	$-2.24152 \pm 2.38312 \times 10^{-3}$
p4	$-0.462582 \pm 1.17706 \times 10^{-3}$
p5	$1.15708 \pm 4.45158 \times 10^{-3}$
p6	$0.848250 \pm 2.15620 \times 10^{-1}$
p7	$-5.87161 \pm 2.15620 \times 10^{-1}$
p8	$-15.0291 \pm 1.75136 \times 10^{3}$
χ^2/n_{dof}	51.39

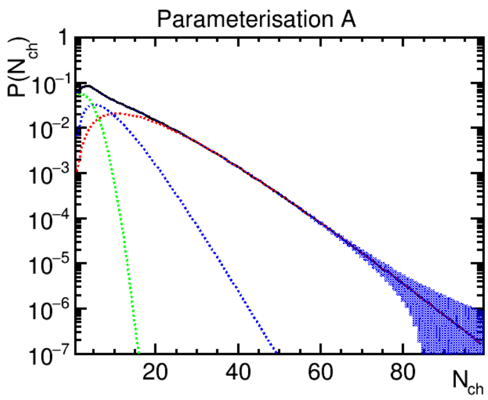

(A) Parameterisation A

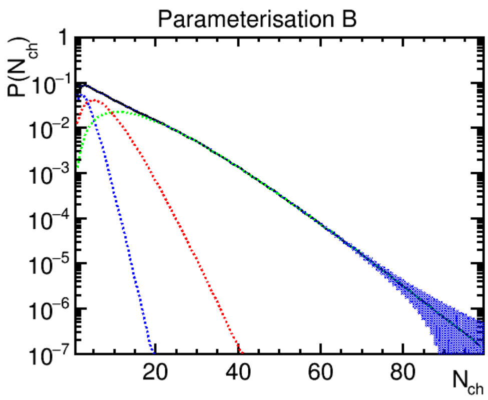

(B) Parameterisation B

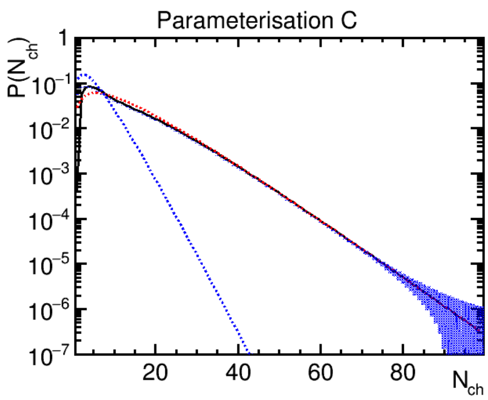

(C) Parameterisation C

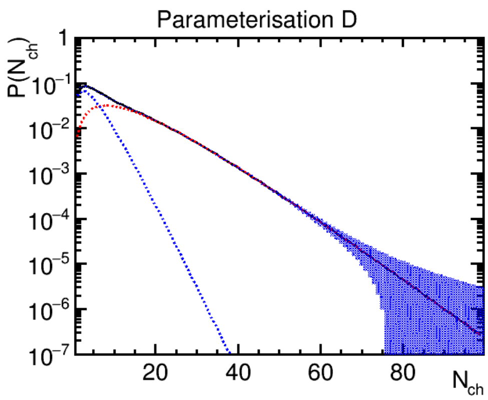

(D) Parameterisation D

FIGURE 5.29: Unfolded Multiplicity for $2.0 \leq \eta \leq 4.5$ for measured data. The errors due to fit are represented by the blue shaded areas and the components of the parameterisation are shown by the dotted lines.

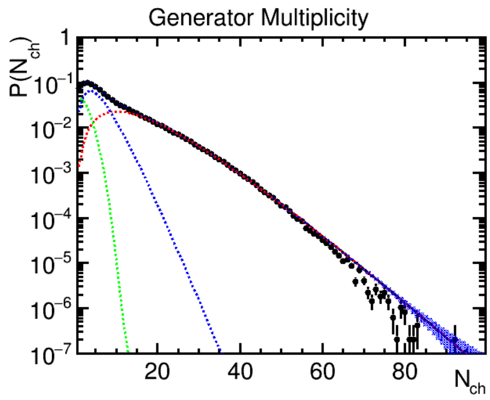

(A) Parameterisation A

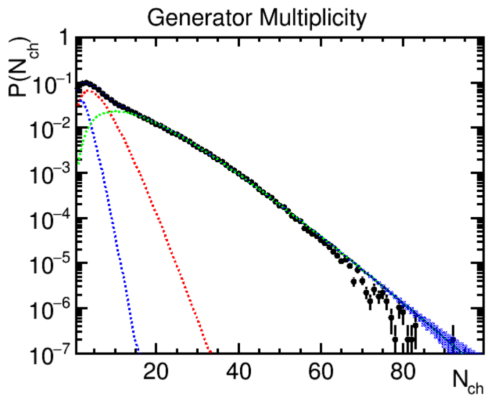

(B) Parameterisation B

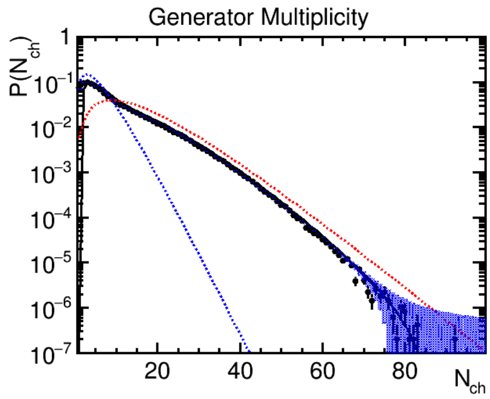

(C) Parameterisation C

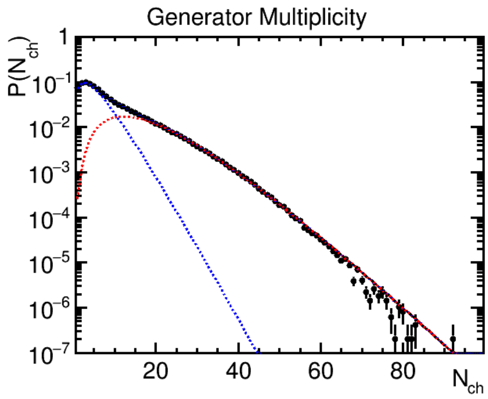

(D) Parameterisation D

FIGURE 5.30: Unfolded multiplicity for $2.0 \leq \eta \leq 4.5$ of tracks reconstructed in MC data. The charged particle distribution in the MC generated data are shown in the black data points. The unfolded multiplicity is consistent with the parameterised generator multiplicities shown in figure 5.27. The distributions are unfolded using several parameterisations shown above.

The unfolding procedure has been applied to reconstructed MC data as a cross check to test the validity of the method. The unfolded multiplicities are shown in figure 5.30, the unfolded multiplicities are consistent with the generated multiplicities shown in figure 5.27.

5.6.3 Pile-Up

Pile up describes interactions in which more there is more than one proton-proton interaction for a given beam crossing. Since the MC generated data does not include detector effects such as pile up, in order to compare the compare the data from MC models to observed data the underlying multiplicity due to single proton-proton collisions is extracted using the method described here. In section 5.5.3 a method to correct the effect on pile-up on the number of proton-proton interactions was demonstrated. In the case of the multiplicity distribution the effect the pile-up has on the shape of the multiplicity distribution must also be calculated. Since the average number of proton-proton interactions (μ) is small as shown in section 5.5.3 the pile-up contribution to the charged particle event multiplicity may be approximated as consisting of the distribution from events with a single proton-proton collision and the convolution of two single proton-proton collisions (equation 5.18),

$$N_{\text{observed}}(n) \approx \frac{N_{\text{single}}(n) + \frac{\mu}{2} N_{\text{single}}(n) * N_{\text{single}}(n)}{A} \tag{5.18}$$

with,

$$N_{\text{single}}(n) * N_{\text{single}}(n) = \sum_{k=0}^{n} N_{\text{single}}(k) \cdot N_{\text{single}}(n-k) \tag{5.19}$$

A is a normalisation constant given by,

$$A = \sum_{n=0}^{n_{\text{max}}} N_{\text{single}}(n) + \frac{\mu}{2} N_{\text{single}}(n) * N_{\text{single}}(n) \tag{5.20}$$

$N_{\text{observed}}(k)$ is the number of events with n charged particles consisting of contributions of events with one or two proton-proton interactions; $N_{\text{single}}(k)$ is the number of events with n charged particles from single proton-proton interactions, k is the number of charged particles from a secondary proton-proton interaction in an event with n charged particles and $N_{\text{single}}(k) * N_{\text{single}}(n-k)$ is the convolution of two single proton-proton interactions producing n charged particles. The normalisation constant A may also be expressed as (see equation 5.8),

$$A = 1 + \frac{\mu}{2} \tag{5.21}$$

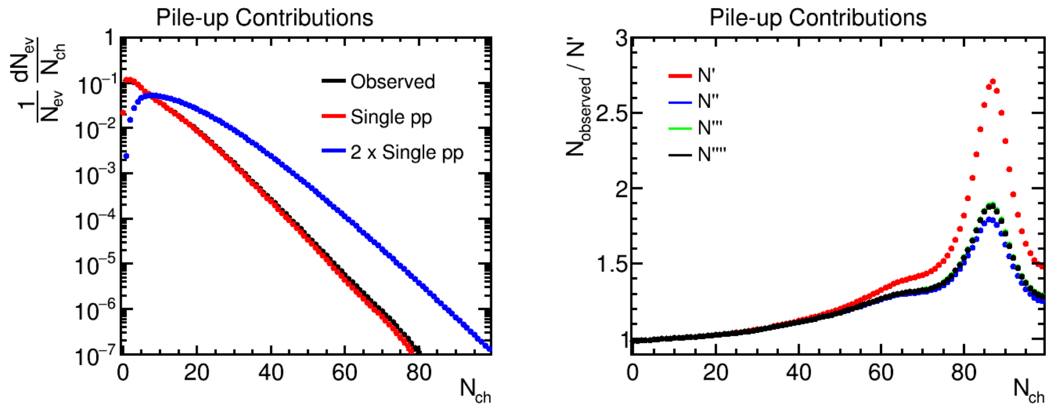

(A) A comparison of the observed multiplicity (black), single proton-proton interaction (red) and the convolution of two single proton-proton interactions (blue).

(B) The ratio of the observed multiplicity distribution to the underlying single proton interaction distribution calculated using the iterative method described.

FIGURE 5.31: Pile-up contributions to the charged particle event multiplicity for $2.0 \leq \eta \leq 4.5$. Figure A) shows the components making up the observed distribution (black), the single proton-proton interaction (red) and the combination of two single proton-proton interactions (blue). It can be seen that the observed distribution is predominantly due to single proton-proton interactions. Figure B) shows the ratios of the observed multiplicity to the multiplicity due to single proton-proton collisions, the data points shown in different colours correspond to the different stages in the iterative process with convergence being shown in the latter iterations. The effect due to the contributions from pile up are most prominent in the high multiplicity region.

since $N_{\text{single}}(n)$ and $N_{\text{single}}(n) * N_{\text{single}}(n)$ are normalised functions of n. Solving equation 5.18 for N_{single} gives,

$$N_{\text{single}}(n) = (1 + \frac{\mu}{2})N_{\text{observed}}(n) - \frac{\mu}{2}N_{\text{single}}(n) * N_{\text{single}}(n) \tag{5.22}$$

The form of this equation suggests an iterative procedure may be used in order to approximate N_{single}, using this approach gives,

$$N''_{\text{single}}(n) = (1 + \frac{\mu}{2})N_{\text{observed}}(n) - \frac{\mu}{2}N_{\text{single}}(n)' * N_{\text{single}}(n)' \tag{5.23}$$

where $N'_{\text{single}}(n)$ is an approximation of $N_{\text{single}}(n)$ and $N''_{\text{single}}(n)$ is the next iteration of the approximation of $N_{\text{single}}(n)$. Starting with $N_{\text{observed}}(n)$ as the initial seed for the process gives the results shown in figure 5.31b.

5.6.4 Uncertainties and Results

Systematic Uncertainties

The systematic uncertainties affecting the unfolded particle event multiplicities are discussed in this section. The uncertainty associated to the uncertainty of the statistical error in the response matrix due to the limited MC simulated events is estimated by producing several additional response matrices with values randomised around the central value. For each element a random number is generated using a Gaussian distribution that has a mean of the central value of the original response matrix calculated in section 5.6.2.1 and a width equal to the statistical uncertainty of the element (an additional renormalisation is required in order to preserve the normalisation of the response matrix). The unfolding procedure is carried out using the randomised response matrices and an average difference between the central value and the value from the randomised response matrix is calculated. Figure 5.32a shows an example of the randomisation procedure and figure 5.32b shows the systematic error as a function of the number of charged particles in the event.

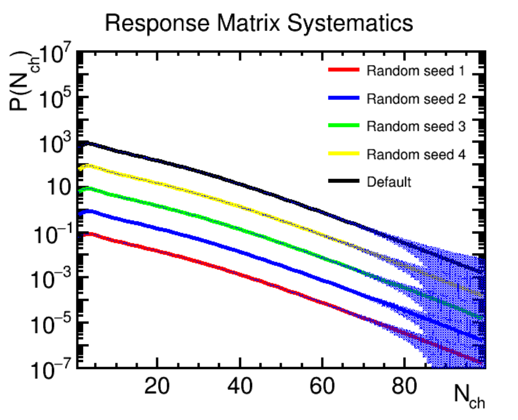

(A) Comparison of unfolded multiplicities.

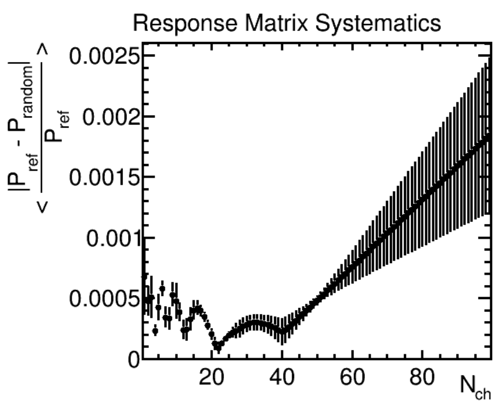

(B) Response matrix systematic error as a percentage

FIGURE 5.32: Response matrix systematic errors. Figure A) shows the difference between the unfolded multiplicities using the default response matrix and response matrices which have had their elements randomly varied within their statistical errors. The results for the different response matrices have been scaled so that they do not overlay one another. Figure B) shows the mean fractional difference between the results from the default response matrix and the response matrices that have been varied within their statistical errors, the overall difference is very small ($< 1\%$); the statistical error on the response matrix has no significant effect on the unfolded multiplicity.

In addition to this a systematic uncertainty is due to the parameterisation model used is also present. To estimate this one of the parameterisation models is nominated as the reference parameterisation and the difference between it and the unfolded distributions from the other parameterisations is used to assign an error, figure 5.33a shows the comparison between the unfolded distributions due to the different parameterisations and figure 5.33b shows the systematic error as a function of the number of charged particles.

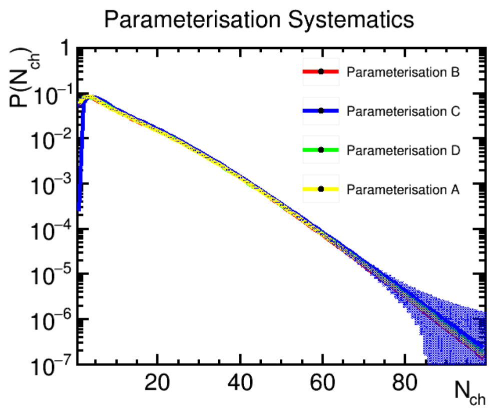

(A) Comparison of unfolded multiplicities.

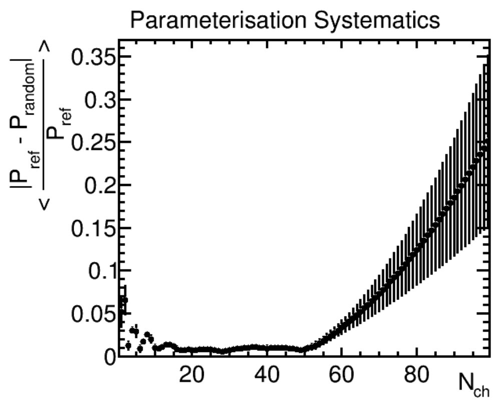

(B) Parameterisation model systematic error as a percentage

FIGURE 5.33: Parameterisation systematic errors. Figure A) shows the difference between the unfolded multiplicities for each parameterisation model. Figure B) shows the mean fractional difference between the parameterisation A and parameterisations B - C, the overall difference is significant in the low and high multiplicity regions.

The uncertainty in the background correction discussed in section 5.5.4 is also present in the measurement of the charged particle event multiplicity, similarly a systematic error of 2% is applied to the final results.

MC Generator Comparison

The unfolded multiplicity distribution together with systematic errors is compared with the multiplicity distributions from the Pythia 6, Pythia8 and EPOS event generators in figure 5.34, the average multiplicity for the respective distributions are shown in table 5.4. The Pythia and EPOS generators show a systematic decrease and increase in higher multiplicity events respectively (in agreement with the charged particle densities).

TABLE 5.4: Comparison of the mean charged particle multiplicity between the unfolded multiplicity and MC simulated data

MC Generator	Mean Multiplicity (N_{ch})
Unfolded	10.272
Pythia6	8.8364
Pythia8	8.1147
EPOS	11.034

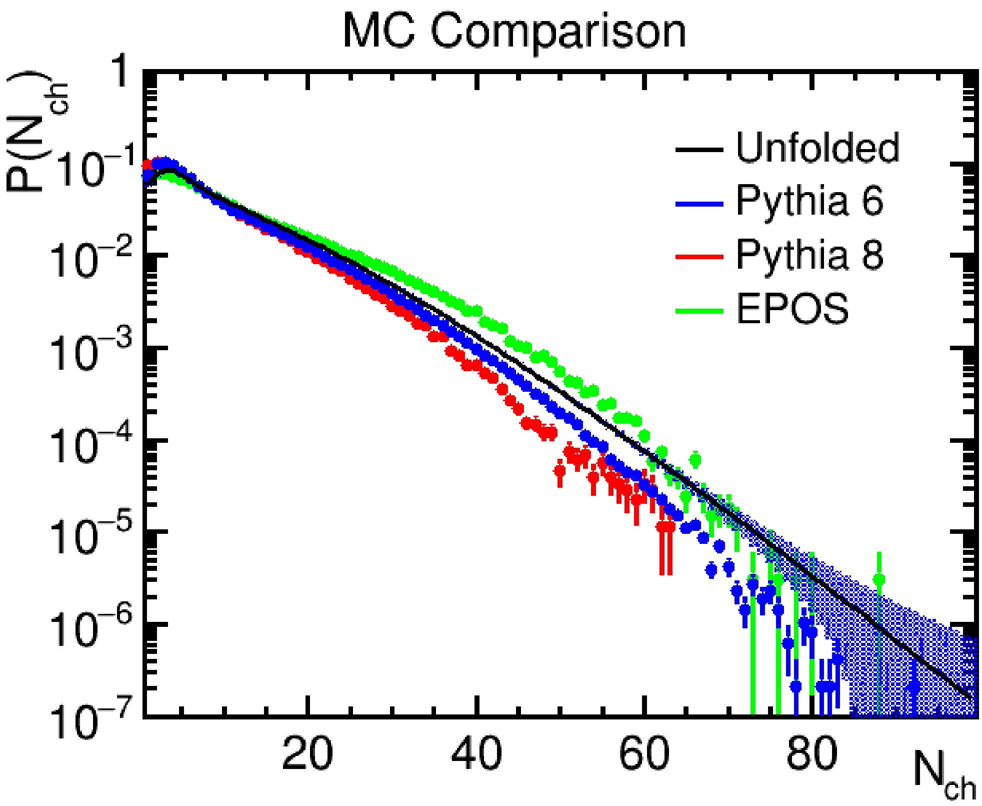

FIGURE 5.34: The unfolded event multiplicity distribution compared with the Pythia6, Pythia8 and EPOS event generators for particles with $2.0 \leq \eta < 4.5$ & $p_{\mathrm{T}} \geq 200$ MeV & $|p| \geq 2000$ MeV. The unfolded distribution is shown in black with the systematics shown in the red shaded boxes.

5.7 Matrix Inversion Unfolding Method

A matrix inversion unfolding method was explored as an alternative to the parameterisation unfolding method. This involved inverting the response matrix to give an unfolding matrix.

$$U = R^-1 \tag{5.24}$$

where U is the unfolding matrix and R is the response matrix. The multiplicity matrix equation is given by,

$$a = R \cdot b \tag{5.25}$$

where a is the column matrix corresponding the the reconstructed track multiplicity such that element n of the matrix corresponds to the number of events where n tracks are observed, R is the response matrix, a two dimensional matrix where element nm corresponds to the probability to reconstruct n tracks given m particles in the event and b is the column matrix where element m corresponds to the number of events with m particles present. In terms of their elements the multiplicity matrix equation can be written as,

$$a_n = \sum_{m=0}^{M} R_{nm} b_m = \sum_{m=0}^{M} P(n|m)\ b_m \tag{5.26}$$

where $P(n|m)$ is the probability to reconstruct n tracks given m particles in the event. Using the unfolding matrix an expression for the unfolded particle multiplicity distribution, b, can be expressed as,

$$U \cdot a = b \tag{5.27}$$

Due to the size of the matrix ($\sim 100 \times 100$) and since the response matrix is not constrained to square matrices the method of singular value decomposition (SVD) was used to calculate the inverse of the response matrix. This method decomposes an $n \times m$ matrix into three component matrices,

$$R = u \cdot W \cdot v^T \tag{5.28}$$

where u and v are orthogonal matrices and W is a diagonal matrix with non-zero elements on the diagonal.

$$u \cdot u^T = \mathbb{I} \qquad v \cdot v^T = \mathbb{I}$$

$$W_{nm} \neq 0 \quad n = m, \qquad W_{nm} = 0 \quad n \neq m$$

The inverse matrix of R is then given by,

$$R^{-1} = (u \cdot W \cdot v^T)^{-1} = v \cdot W^{-1} \cdot u^T \tag{5.29}$$

and therefore the matrix multiplicity equation can be expressed as,

$$v \cdot W^{-1} \cdot u^T \cdot a = b \tag{5.30}$$

Inverting the response matrix using the method described above results in an unfolding matrix with large errors across the range of multiplicities, this is due effects from the statistical uncertainty, especially at the higher multiplicities where the errors relative to the value are large,

$$\frac{\Delta x}{x} \sim 1$$

by inverting the matrix, the errors at the higher multiplicities are propagated to the entire multiplicity range of the unfolding matrix. This has two noticeable effects when unfolding the reconstructed track multiplicity. Firstly the errors across the multiplicity range are very large due the amplification of statistical insignificant measurements (noise) and secondly, oscillatory behaviour in the multiplicity is introduced.

This oscillatory behaviour can be attributed to the orthogonal matrices u and v since the unfolding method becomes in effect the summation of the orthogonal rows and columns in these matrices weighted by the diagonal elements of the diagonal matrix W^{-1}. In order to reduce these effects it is necessary to reduce the contributions from the noise.

This was attempted by using a regularisation scheme which introduces a cut off that restricts the higher order contributions from the diagonal W^{-1} matrix. This method shows some promise and is currently in development.

Chapter 6

Conclusion

Outlined in this thesis are the key physics underlying particle production phenomena as well as prospective areas of interest in this field of physics. The LHCb detector is highly suited to this are of research due especially to its exceptional tracking as well as its overall performance in all areas.

A method in which the effective position of Hybrid Photo-Detectors (HPDs) in Cherenkov imaging detectors may be aligned by software was presented. This has shown to have a significant increase in the ability of the detector to distinguish particle species, aiding in many of the key measurements made at the LHCb detector. The particle identification power of the LHCb detector also gives a unique opportunity of studying the charged particle production of individual particle species further constraining current event generator models.

Comparisons between the unfolded charged particle distributions and Monte Carlo event generated distributions show significant differences between measured data and MC simulators (as well as between the different event generators). The measurements in this thesis will hopefully go on to help constrain these generators, increasing their predictive powers well as providing insight into the phenomena of particle production in the soft QCD regime. Understanding these phenomena is particularly important for physics at the LHC since multiplicity sensitive phenomena such additional hard or semi-hard scatters are predicted to be more prevalent at the collision energies present at the LHC [56].

With the increasing collision energies at luminosity at the LHC, the future at the LHC promises to be an exciting and challenging environment in which great advances will be made.

Appendix A

MC Generator Parameters

A.1 PYTHIA Event Generator Parameters

Table A.1: The non default parameters used in the generation of MC events using versions 6.418 and 8.135 of the PYTHIA program.

Parameter	Value
ckin(41)	3.0
mstp(2)	2
mstp(33)	3
mstp(128)	2
mstp(81)	21
mstp(82)	3
mstp(52)	2
mstp(51)	10042 (i.e. CTEQ6 Leading order fit, with α_S PDF from LHAPDF)
mstp(142)	2
parp(67)	1.0
parp(82)	4.28
parp(89)	14000
parp(90)	0.238
parp(85)	0.33
parp(86)	0.66
parp(91)	1.0
parp(149)	0.02
parp(150)	0.085
parj(11)	0.5
parj(12)	0.4
parj(13)	0.79
parj(14)	0.0
parj(15)	0.018
parj(16)	0.054
parj(17)	0.131
mstj(26)	0
parj(33)	0.4

Bibliography

[1] David Griffiths. *Introduction to elementary particles.* Wiley VCH; 2nd, Revised Edition edition, 2008.

[2] B. Odom, D. Hanneke, B. D'Urso, and G. Gabrielse. New measurement of the electron magnetic moment using a one-electron quantum cyclotron. *Phys. Rev. Lett.*, 97:030801, Jul 2006. doi: 10.1103/PhysRevLett.97.030801. URL http://link.aps.org/doi/10.1103/PhysRevLett.97.030801.

[3] Dave Fehling. The standard model of particle physics: A lunchbox's guide, 2008. URL http://www.pha.jhu.edu/~dfehling/.

[4] Guido Altarelli and G. Parisi. Asymptotic Freedom in Parton Language. *Nucl.Phys.*, B126:298, 1977. doi: 10.1016/0550-3213(77)90384-4.

[5] Rick D. Field. The Underlying event in hard scattering processes. *eConf*, C010630: P501, 2001.

[6] T. Akesson et al. Double Parton Scattering in pp Collisions at $\sqrt{s} = 63$-GeV. *Z.Phys.*, C34:163, 1987. doi: 10.1007/BF01566757.

[7] F. Abe et al. Measurement of double parton scattering in $\bar{p}p$ collisions at $\sqrt{s} = 1.8$ TeV. *Phys.Rev.Lett.*, 79:584–589, 1997. doi: 10.1103/PhysRevLett.79.584.

[8] F. Abe et al. Double parton scattering in $\bar{p}p$ collisions at $\sqrt{s} = 1.8$TeV. *Phys.Rev.*, D56:3811–3832, 1997. doi: 10.1103/PhysRevD.56.3811.

[9] V.M. Abazov et al. Double parton interactions in photon+3 jet events in pp^{-} bar collisions $\sqrt{s} = 1.96$ TeV. *Phys.Rev.*, D81:052012, 2010. doi: 10.1103/PhysRevD.81.052012.

[10] D. Acosta et al. The underlying event in hard interactions at the Tevatron $\bar{p}p$ collider. *Phys.Rev.*, D70:072002, 2004. doi: 10.1103/PhysRevD.70.072002.

[11] T. Aaltonen et al. Studying the Underlying Event in Drell-Yan and High Transverse Momentum Jet Production at the Tevatron. *Phys.Rev.*, D82:034001, 2010. doi: 10.1103/PhysRevD.82.034001.

[12] Vardan Khachatryan et al. First Measurement of the Underlying Event Activity at the LHC with $\sqrt{s} = 0.9$ TeV. *Eur.Phys.J.*, C70:555–572, 2010. doi: 10.1140/epjc/s10052-010-1453-9.

[13] Torbjörn Sjöstrand and Maria van Zijl. A multiple-interaction model for the event structure in hadron collisions. *Phys. Rev. D*, 36:2019–2041, Oct 1987. doi: 10.1103/PhysRevD.36.2019. URL http://link.aps.org/doi/10.1103/PhysRevD.36.2019.

[14] T. Sjostrand and Peter Z. Skands. Multiple interactions and the structure of beam remnants. *JHEP*, 0403:053, 2004. doi: 10.1088/1126-6708/2004/03/053.

[15] T. Sjostrand and Peter Z. Skands. Transverse-momentum-ordered showers and interleaved multiple interactions. *Eur.Phys.J.*, C39:129–154, 2005. doi: 10.1140/epjc/s2004-02084-y.

[16] J.M. Butterworth, Jeffrey R. Forshaw, and M.H. Seymour. Multiparton interactions in photoproduction at HERA. *Z.Phys.*, C72:637–646, 1996. doi: 10.1007/s002880050286.

[17] Manuel Bahr, Stefan Gieseke, and Michael H. Seymour. Simulation of multiple partonic interactions in Herwig++. *JHEP*, 0807:076, 2008. doi: 10.1088/1126-6708/2008/07/076.

[18] PYTHIA 8. Pythia 8, 2014. URL http://home.thep.lu.se/~torbjorn/pythia81php/Welcome.php.

[19] R et al Antunes-Nobrega. *LHCb computing: Technical Design Report*. Technical Design Report LHCb. CERN, Geneva, 2005. Submitted on 11 May 2005.

[20] EvtGen. The evtgen project, 2014. URL http://lhcb-release-area.web.cern.ch/LHCb-release-area/DOC/gauss/generator/evtgen.php.

[21] Geant 4. Geant 4, 2014. URL http://geant4.cern.ch/.

[22] Klaus Werner. The hadronic interaction model {EPOS}. *Nuclear Physics B - Proceedings Supplements*, 175176(0):81 – 87, 2008. ISSN 0920-5632. doi: http://dx.doi.org/10.1016/j.nuclphysbps.2007.10.012. URL http://www.sciencedirect.com/science/article/pii/S0920563207007736. Proceedings of the {XIV} International Symposium on Very High Energy Cosmic Ray Interactions.

[23] T. Pierog, Iu. Karpenko, J.M. Katzy, E. Yatsenko, and K. Werner. EPOS LHC : test of collective hadronization with LHC data. 2013.

[24] K. Werner, Iu. Karpenko, T. Pierog, M. Bleicher, and K. Mikhailov. Event-by-Event Simulation of the Three-Dimensional Hydrodynamic Evolution from Flux Tube Initial Conditions in Ultrarelativistic Heavy Ion Collisions. *Phys.Rev.*, C82:044904, 2010. doi: 10.1103/PhysRevC.82.044904.

[25] J Kwiecinski. Introduction to the Pomeron. Technical Report hep-ph/9611306. INP-1743-PH, Polish Acad. Sci. Inst. Nucl. Res., Cracow, Nov 1996.

[26] K et al Aamodt. The ALICE experiment at the CERN LHC. A Large Ion Collider Experiment. *J. Instrum.*, 3:S08002. 259 p, 2008. Also published by CERN Geneva in 2010.

[27] G et al Aad. The ATLAS Experiment at the CERN Large Hadron Collider. *J. Instrum.*, 3:S08003. 437 p, 2008. Also published by CERN Geneva in 2010.

[28] S et al Chatrchyan. The CMS experiment at the CERN LHC. The Compact Muon Solenoid experiment. *J. Instrum.*, 3:S08004. 361 p, 2008. Also published by CERN Geneva in 2010.

[29] A Augusto et al Alves. The LHCb Detector at the LHC. *J. Instrum.*, 3(LHCb-DP-2008-001. CERN-LHCb-DP-2008-001):S08005, 2008. Also published by CERN Geneva in 2010.

[30] G Anelli and et al. The TOTEM Experiment at the CERN Large Hadron Collider. *J. Instrum.*, 3:S08007, 2008.

[31] O et al Adriani. The LHCf detector at the CERN Large Hadron Collider. *J. Instrum.*, 3:S08006, 2008.

[32] T Latham. Performance of the LHCb Vertex Locator. Nov 2012.

[33] R. et al Aaij. Measurement of b-hadron branching fractions for two-body decays into charmless charged hadrons. *Journal of High Energy Physics*, 2012(10): 1–21, 2012. doi: 10.1007/JHEP10(2012)037. URL http://dx.doi.org/10.1007/JHEP10%282012%29037.

[34] R. et al Aaij. First observation of the decay $B_c^+ \to j/\psi\pi^+\pi^-\pi^+$. *Phys. Rev. Lett.*, 108:251802, Jun 2012. doi: 10.1103/PhysRevLett.108.251802. URL http://link.aps.org/doi/10.1103/PhysRevLett.108.251802.

[35] R. Aaij eta al. Observation of {CP} violation in decays. *Physics Letters B*, 712(3):203 – 212, 2012. ISSN 0370-2693. doi: http://dx.doi.org/10.1016/j.physletb.2012.04.060. URL http://www.sciencedirect.com/science/article/pii/S0370269312004893.

[36] R. et al Aaij. Measurement of the ratio of branching fractions $\mathcal{B}(B^0 \to K^{*0}\gamma)/\mathcal{B}(B_s^0 \to \phi\gamma)$. *Phys. Rev. D*, 85:112013, Jun 2012. doi: 10.1103/PhysRevD.85.112013. URL http://link.aps.org/doi/10.1103/PhysRevD.85.112013.

[37] R.et al Aaij. First evidence of direct *cp* violation in charmless two-body decays of B_s^0 mesons. *Phys. Rev. Lett.*, 108:201601, May 2012. doi: 10.1103/PhysRevLett.108.201601. URL http://link.aps.org/doi/10.1103/PhysRevLett.108.201601.

[38] S et al Amato. *LHCb RICH: Technical Design Report*. Technical Design Report LHCb. CERN, Geneva, 2000.

[39] S et al Amato. *LHCb magnet: Technical Design Report*. Technical Design Report LHCb. CERN, Geneva, 2000.

[40] Tracking strategies used in LHCb, 2014. URL https://twiki.cern.ch/twiki/bin/view/LHCb/LHCbTrackingStrategies.

[41] S et al Amato. *LHCb calorimeters: Technical Design Report*. Technical Design Report LHCb. CERN, Geneva, 2000.

[42] Irina Machikhiliyan and the LHCb calorimeter group. Current status and performance of the lhcb electromagnetic and hadron calorimeters. *Journal of Physics: Conference Series*, 293(1):012052, 2011. URL http://stacks.iop.org/1742-6596/293/i=1/a=012052.

[43] A A Alves Jr et al. Performance of the lhcb muon system. *Journal of Instrumentation*, 8(02):P02022, 2013. URL http://stacks.iop.org/1748-0221/8/i=02/a=P02022.

[44] *LHCb muon system: second addendum to the Technical Design Report*. Technical Design Report LHCb. CERN, Geneva, 2005. Submitted on 9 Apr 2005.

[45] Barbosa-Marinho. *LHCb muon system: Technical Design Report*. Technical Design Report LHCb. CERN, Geneva, 2001.

[46] Jr Alves, A.A., L. Anderlini, M. Anelli, R. Antunes Nobrega, G. Auriemma, et al. Performance of the LHCb muon system. *JINST*, 8:P02022, 2013. doi: 10.1088/1748-0221/8/02/P02022.

[47] F. Archilli, W. Baldini, G. Bencivenni, N. Bondar, W. Bonivento, et al. Performance of the Muon Identification at LHCb. 2013.

[48] R Aaij and J et al Albrecht. The LHCb Trigger and its Performance in 2011. *J. Instrum.*, 8(arXiv:1211.3055. CERN-LHCb-DP-2012-004. LHCb-DP-2012-004): P04022. 31 p, Nov 2012.

[49] R et al Antunes-Nobrega. *LHCb trigger system: Technical Design Report*. Technical Design Report LHCb. CERN, Geneva, 2003. revised version number 1 submitted on 2003-09-24 12:12:22.

[50] Mariusz Witek. The software architecture of the lhcb high level trigger. *Journal of Physics: Conference Series*, 396(1):012053, 2012. URL http://stacks.iop.org/1742-6596/396/i=1/a=012053.

[51] A Mollen and T Gys. Hpd image shift in lab - rich operations meeting 11/04/2009, 2009. URL https://indico.cern.ch/event/75126.

[52] G. Aad et al. Charged-particle multiplicities in pp interactions measured with the ATLAS detector at the LHC. *New J.Phys.*, 13:053033, 2011. doi: 10.1088/1367-2630/13/5/053033.

[53] Vardan Khachatryan et al. Charged particle multiplicities in *pp* interactions at $\sqrt{s} = 0.9$, 2.36, and 7 TeV. *JHEP*, 1101:079, 2011. doi: 10.1007/JHEP01(2011)079.

[54] K. Aamodt et al. Charged-particle multiplicity measurement in proton-proton collisions at $\sqrt{s} = 7$ TeV with ALICE at LHC. *Eur.Phys.J.*, C68:345–354, 2010. doi: 10.1140/epjc/s10052-010-1350-2.

[55] Roel Aaij et al. Measurement of charged particle multiplicities and densities in *pp* collisions at $\sqrt{s} = 7$ TeV in the forward region. *Eur.Phys.J.*, C74:2888, 2014. doi: 10.1140/epjc/s10052-014-2888-1.

[56] P. Bartalini et al. Multi-Parton Interactions at the LHC.